Reaction Nanoscopy:
From near-field dependent ion yields toward surface chemistry

Philipp Maximilian Rosenberger

München 2023

Reaction Nanoscopy:
From near-field dependent ion yields toward surface chemistry

Philipp Maximilian Rosenberger

Dissertation
an der Fakultät für Physik
der Ludwig–Maximilians–Universität
München

vorgelegt von
Philipp Maximilian Rosenberger
aus Hutthurm

München, den 19. Dezember 2022

Erstgutachter: Prof. Dr. Matthias F. Kling
Zweitgutachter: Prof. Dr. Matthias Ihme
Tag der mündlichen Prüfung: 10. Februar 2023

Contents

Zusammenfassung **ix**

Abstract **xi**

1 Introduction **1**

List of publications by the author **5**

2 Theoretical model **9**
2.1 General description 9
2.2 Electric field calculations 10
2.3 ADK rate and ionization probability 11
2.4 Generation of static surface charges 14
2.4.1 Rejection sampling 14
2.4.2 Candidate generation 14
2.4.3 Candidate acceptance 15
2.4.4 Total charge 16
2.5 Ion generation and propagation 18

3 Experimental Methods **21**
3.1 Aerosol generation 21
3.1.1 Aerosolization of silica nanoparticles 21
3.1.2 Droplet aerosol generation 24
3.1.3 Aerodynamic Lens 25
3.2 Laser systems 25
3.3 Reaction nanoscope 27
3.3.1 Detection of nanoparticle or droplet events 27
3.3.2 Typical nanoparticle density in the laser focus 31
3.3.3 Ion momentum measurement 33

4 Reaction nanoscopy with nanoparticle clusters **39**
4.1 Introduction 39
4.2 Experimental Techniques 41
4.3 Proton Emission from single nanoparticles and nanoparticle clusters 41

4.4 Dependence on intensity and wavelength . . . 44
4.5 Theoretical Results . . . 45
4.6 Coincident ion emission . . . 49
4.7 Discussion . . . 51
4.8 Conclusions . . . 54

5 Elliptical polarization and surface groups 57
5.1 Introduction . . . 57
5.2 Experimental Methods . . . 58
5.2.1 Laser system . . . 59
5.2.2 Reaction nanoscope . . . 59
5.2.3 Nanoparticle Delivery . . . 60
5.2.4 Nanoparticle synthesis . . . 60
5.3 Theoretical model . . . 61
5.4 Results . . . 61
5.5 Discussion . . . 69
5.6 Conclusions . . . 71

6 Reaction nanoscopy with droplets 73
6.1 Introduction . . . 73
6.2 Experimental . . . 75
6.2.1 Laser system . . . 76
6.2.2 Reaction nanoscopy with droplets . . . 76
6.3 Theoretical description of the droplet surface . . . 76
6.4 Results . . . 77
6.4.1 Near-field driven ion emission . . . 77
6.5 Intensity dependence of the ion emission angle . . . 79
6.6 Droplet size characterization . . . 81
6.7 Droplet charge and stability . . . 83
6.8 Ion emission: gas-phase vs. droplet . . . 84
6.9 Isomer comparison . . . 86
6.10 Conclusion . . . 88

A Expression for elliptical input fields for the FDTD simulations 91

B Energy of a charged spherical surface 93

Acknowledgments 109

List of Figures

1.1 Field Enhancement 2

2.1 Ionization rate and probability 13
2.2 Discrete and continuous sampling 15
2.3 Electric field, ionization probability and charge distribution 16
2.4 Potential due to the polarization of a dielectric 19

3.1 Aerosol Generation 22
3.2 Particle Characterization by SEM 23
3.3 Proton rate vs. nozzle diameter of the aerodynamic lens 26
3.4 FROG characterization of the 2 micron pulses 27
3.5 Reaction nanoscope and coincident electron detection 28
3.6 Reduction of false coincidences in droplet experiments 30
3.7 Multihit probability vs. channeltron hit rate 32
3.8 Asymmetric proton spectra 36
3.9 Single-shot detector response with nanoparticles at high laser intensity . . 37

4.1 Field enhancement for single nanoparticles and clusters 41
4.2 Proton momentum distribution vs. nanoparticle concentration 42
4.3 Dependence of cluster contribution on laser intensity 43
4.4 Cluster signature at longer wavelengths 45
4.5 Experiment vs. Simulation for nanoparticle dimers 46
4.6 Experiment vs. Simulation for nanoparticle dimers - 1D projections 48
4.7 Cumulative proton yield as a function of dimer angle 49
4.8 PiPiCo for gas phase vs. nanoparticle ions 50
4.9 Physical interpretation of nanoparticle-related PiPiCo histograms 52

5.1 Reaction Nanoscopy setup for ellipticity investigations 59
5.2 Field enhancement vs. ion emission for different ellipticities 62
5.3 Experiment vs. theory for ion emission with different ellipticities 63
5.4 Alkoxy group formation on silica surfaces 63
5.5 Solvent comparison 65
5.6 Ion energies for different ellipticities 68
5.7 Coincidence and covariance histograms for H^+ and CH_3^+ 69

6.1 Schematic of droplet experiment 74
6.2 Detailed depiction of experimental setup for droplet experiments 75
6.3 Simulation geometry for 1,2-PDO and 1,3-PDO 77
6.4 Ion emission from droplets 78
6.5 Intensity dependence of droplet proton emission 80
6.6 Droplet size and charge characterization 82
6.7 Discrimination between droplet data and gas-phase data 85
6.8 Proving PDO protonation by symmetry 87
6.9 Isomer comparison for droplet and gas-phase ions 88
6.10 Energy of 1,2-propanediol vs. C2-C3 rotation angle 89

Zusammenfassung

Die Wechselwirkung zwischen Licht und Nanoteilchen führt zu einer lokalen Verstärkung des elektromagnetischen Feldes auf der Teilchenoberfläche. Im Regime der Starkfeld-Physik verursacht diese Feldlokalisierung eine räumlich begrenzte Emission von Ionen von der Oberfläche von sphärischen Nanopartikeln, die mit der kürzlich eingeführten Reaktionsnanoskopietechnik abgebildet werden kann. Die Technik erlaubt die massenaufgelöste Messung der Energie- und Winkelverteilungen von Ionen, die durch die Starkfeld-Ionisation einzelner Nanopartikel im Vakuum erzeugt werden.

In der vorliegenden Arbeit wurden Reaktionsnanoskpie-Experimente für einen breiten Bereich experimenteller Parameter durchgeführt und die Ergebnisse weitgehend durch ein Monte-Carlo-Modell reproduziert, das auf der Nahfeld-getriebenen Erzeugung von Ladungen und ihrer klassischen Propagation beruht.

Im ersten Teil der Arbeit werden Experimente an SiO_2-Nanoteilchen mit hohen Probenkonzentrationen und niedrigen Laserintensitäten behandelt. Mit Hilfe des Monte-Carlo-Modells wurden charakteristische Signaturen in den Daten auf die Ionenemission von Nanopartikel-Clustern zurückgeführt. Auf der Grundlage dieser Ergebnisse wurden verschiedene Methoden vorgeschlagen, die eine Trennung der Messdaten in die Beiträge einzelner Nanopartikel und Clusterbeiträge ermöglichen. Diese Signaltrennung und der Nachweis von Nanopartikel-Clustern im Allgemeinen war in früheren Studien zur Starkfeld-*Elektronen*-Emission von Nanopartikeloberflächen nicht möglich. Die dort beobachteten Abweichungen zwischen Theorie und Experiment könnten daher durch einen nicht berücksichtigten Beitrag von Elektronen aus Nanopartikel-Clustern erklärt werden.

Der zweite Teil der Arbeit enthält eine Parameterstudie an einzelnen SiO_2-Nanopartikeln bei verschiedenen Laserpolarisationen und -intensitäten. Außerdem werden Isotopenaustauschexperimente vorgestellt, die die molekulare Oberflächenzusammensetzung von SiO_2-Nanoteilchen in typischen Reaktionsnanoskopie-Experimenten klären. Die Analyse der entsprechenden Ergebnisse wurde genutzt, um die Gültigkeit des Monte-Carlo-Modells zu prüfen und die Grenzen seiner Anwendbarkeit zu ermitteln. Die hier gewonnenen Erkenntnisse bilden die Grundlage für die zukünftige Entwicklung einer theoretischen Beschreibung von Reaktionsnanoskopie-Experimenten, die auf der molekularen Beschaffenheit der Nanopartikeloberfläche basiert.

Der letzte Teil der Arbeit befasst sich mit der ersten Studie zur Reaktionsnanoskopie an starkfeld-ionisierten Nanotröpfchen. Anhand von Propandiol-Tröpfchen wurde gezeigt, dass der an festen Nanoteilchen beobachtete enge Zusammenhang zwischen der Nahfeld-

verteilung und der Winkelverteilung der Ionenausbeute auch für Nanotröpfchen beobachtet wird. Diese Übereinstimmung wurde für eine in-situ-Charakterisierung der häufigsten Tröpfchengröße in der Verteilung und für die Bewertung der Tröpfchenstabilität genutzt. Schließlich wird ein Vergleich der Ionenspektren von Tröpfchen aus zwei verschiedenen Propandiol-Isomeren durchgeführt. Ergebnisse aus Dichtefunktionaltheorie-Rechnungen deuten darauf hin, dass ein Teil der beobachteten Unterschiede in den Spektren auf die isomerspezifische Molekülstruktur auf der Tröpfchenoberfläche zurückzuführen ist.

Die Ergebnisse dieser Arbeit belegen das enorme Potenzial der Anwendung der Reaktionsnanoskopie auf Problemstellungen der Oberflächenchemie. Die Technik legt den Grundstein für die Verfolgung der Entstehung von Reaktionsprodukten auf den Größenordnungen von Femtosekunden und Nanometern.

Abstract

The interaction between light and nanoparticles leads to a local enhancement of the electromagnetic field on the particle surface. In the regime of strong-field physics, this field localization causes a spatially confined emission of ions from the surface of spherical nanoparticles, which can be imaged using the recently introduced reaction nanoscopy technique. The technique facilitates the mass-resolved measurement of energy and angular distributions of ions produced by the strong-field ionization of individual nanoparticles in a vacuum.

In this work, reaction nanoscopy experiments were performed for a wide range of experimental parameters. The results were largely reproduced by a Monte Carlo model based on the near-field driven generation of charges and their classical propagation.

The first part of this work describes experiments employing silica nanoparticles with high sample concentrations and low laser intensities. Using the Monte-Carlo model, characteristic signatures in the data are attributed to ion emission from nanoparticle clusters. Based on these results, several methods are proposed to separate reaction nanoscopy data into single nanoparticle and cluster contributions. This signal separation and the detection of nanoparticle clusters has not been possible in previous studies on strong-field *electron* emission from nanoparticles. The deviations between theory and experiment observed there are consistent with an unaccounted contribution of nanoparticle clusters.

The second part contains a parametric study of different laser polarizations and intensities incident on single silica nanoparticles. Isotope exchange experiments are presented, which are used to investigate the molecular surface composition of silica particles in typical reaction nanoscopy experiments. The results are used to evaluate the applicability of the Monte-Carlo model and explore its limitations. The insights gained here form the foundation for future developments toward a theoretical description of reaction nanoscopy experiments based on the molecular details of the nanoparticle surface.

The final part of this thesis covers the first reaction nanoscopy study on strong-field ionized nanodroplets. Using propanediol droplets, it is demonstrated that a close correspondence between the near-field distribution and the angular distribution of the ion yield is observed for droplets similar to that of solid particles. This correspondence is used for an in situ characterization of the mean droplet size and for evaluating droplet stability. Finally, a comparison of the ion spectra for droplets from two different propanediol isomers is carried out. Density functional theory results suggest that parts of the observed differences can be attributed to the isomer-specific molecular structure on the droplet surface.

The findings of this thesis demonstrate the great potential of the application of reac-

tion nanoscopy to surface chemistry. The technique paves the way toward spatiotemporal tracing of reaction products on the femtosecond and nanometer scales.

Chapter 1

Introduction

Nanoparticles and nanodroplets are highly relevant in many fields of science. In chemistry, nanoparticles are widely used for separation[1–3], enrichment [4–6] and catalysis [7–9]. Catalytic nanoparticles enable, for example, the efficient production of synthetic and carbon-neutral fuels and may accelerate the transition to renewable and sustainable energy sources [10, 11]. Nanodroplets can serve as highly efficient reaction environments as well [12–16]. They hold great potential for the chemical and pharmaceutical industry [17, 18] and are considered a key element in prebiotic chemistry [19–22]. Atmospheric aerosols contain both, droplets and particles. They have a substantial impact on human health [23] as well as the weather and the global climate due to their role as condensation nuclei and their influence on the earth's radiative balance [24–26]. In biology and medicine, nanoparticles hold great promise for molecular sensing applications [27], and as drug delivery vessels [28]. Among other things, they allow a traversal of the blood-brain-barrier [29–31], which is a crucial step toward an effective treatment of cerebral diseases [32]. With the ongoing COVID-19 pandemic and the corresponding immunochromatographic rapid tests, nanoparticles have even become ubiquitous in everyday life. These tests use the accumulation of functionalized metallic nanoparticles (gold or silver) to indicate a positive or negative result [33]. The red appearance of the chromatographic indicator lines is the consequence of the interaction of light with the metallic nanoparticles.

This effect of structural color [34] is one of many intriguing optical properties of nanoparticles or nanodroplets. For metallic nanoparticles, the free electrons give rise to collective oscillations at the particle surface, which can be driven resonantly for a certain wavelength. Around this so-called localized surface plasmon resonance [35], the absorption of light is greatly enhanced, causing the colorful appearance of metallic nanoparticles. While, for dielectric materials, equivalent resonance effects can only be observed outside the optical domain [36], dielectric and metallic nanospheres share many of their other optical properties. The most relevant ones for this thesis are the localized enhancement of the electric field around a nanosphere and the effect of nanofocusing [37], which are beneficial for techniques like surface-enhanced Raman spectroscopy [38] and other nonlinear spectroscopies [39]. These techniques make use of the enhancement of the electric field enhancement at the interface between the particle and the environment, as shown for an

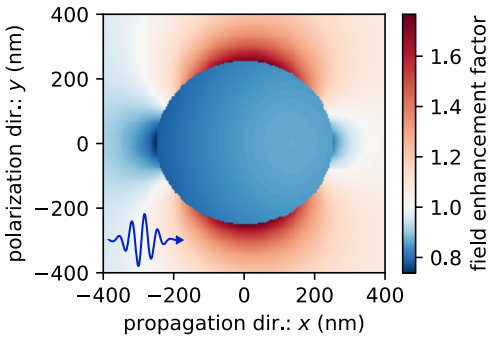

Figure 1.1: Field enhancement in the plane $z = 0$ for light with a wavelength of $\lambda = 2\,\mu$m and a sphere at the origin (diameter $d = 500\,$nm and refractive index $n = 1.5$). The field enhancement factor is defined as the ratio between the local amplitude of the electric field and the amplitude of an incoming plane wave. It was calculated from the Mie solution of Maxwell's equations [40].

exemplary case in Fig. 1.1. The localization of the field at the surface of the nanosphere implies that field-sensitive experimental techniques can, in principle, also be sensitive to the particle or droplet surface and its local chemical composition. Such a surface sensitivity is highly desirable for almost all of the above-mentioned applications of nanoparticles and droplets.

For nanoparticles and droplets in a vacuum, a very direct way of achieving this sensitivity is by the detection of ions, which are generated by strong-field ionization of the surface. The process of strong-field ionization is highly sensitive to near-field variations[41–46], and the ions can serve as a fingerprint of local, ionization-induced chemical processes on the nanosurface. The recent introduction of the reaction nanoscopy technique [47] has enabled the recording of such fingerprints. The technique facilitates the mass-resolved measurement of energy and angular distributions of ions produced upon strong-field ionization of isolated nanoparticles in a vacuum. Its surface sensitivity relies on the choice of sufficiently low intensities such that bulk ionization and plasma formation, as reported in earlier studies [48], can be avoided. With this condition met, however, it has been shown that the angular distribution of the protons emitted from silica nanoparticles is a direct map of the angular distribution of the proton yield on the particle surface [47]. This spatial mapping of strong-field-induced reaction yields makes reaction nanoscopy a unique and promising technique for the direct observation and control of laser-induced chemistry on nanoscale surfaces.

In this thesis, the experimental and theoretical advances in the reaction nanoscopy technique since its introduction are presented. In the experiments, silica nanoparticles, clusters of silica nanoparticles, as well as propanediol nanodroplets were investigated using a wide range of different laser parameters. The generated ion data were used to assess the target size and morphology, the validity of the theory, and to investigate the surface chemistry of the targets.

The structure of the thesis is described in the following. In the next chapter (Chapter 2), a model for the strong-field ionization of nanoparticles, as well as the near-field driven generation and emission of ions is presented. The charge generation is based on quantum-mechanical rates using the optical near-field as an input, and the ions are propagated classically. The ion emission model was used for the description of all results involving silica nanoparticles and has been employed for modeling further reaction nanoscopy experiments

outside the realm of this thesis [49].

In Chapter 3, the reaction nanoscopy technique is introduced. This includes the description of the experimental procedure for generating aerosols of droplets and nanoparticles as well as the manufacturing process of the silica nanoparticles. Moreover, the parameters of the different laser systems used for the reaction nanoscopy experiments are presented and the reaction nanoscope itself is described in much detail.

The chapters thereafter contain the results of three reaction nanoscopy projects carried out by the author in chronological order. In Chapter 4, we discuss the effect of nanoparticle clusters (in particular nanoparticle dimers) on the reaction nanoscopy data. It is shown that the strongly nonlinear nature of the ion emission causes a suppression of the ion yield from unaligned dimers with respect to the laser polarization and a dominant contribution of the aligned ones. Additionally, the signature of clusters in the ion-ion coincidence spectra and the differences between coincidences from nanoparticle ion emission to conventional ion-ion coincidence spectroscopy are discussed. It is furthermore demonstrated that the cluster-related ion signal dominates at low laser intensities, even for a small relative amount of cluster compared to single nanoparticles. This observation is a possible explanation for discrepancies between the theory and experiments in earlier studies on strong-field electron emission from nanoparticles, where a possible contribution of nanoparticle clusters at low intensities was not considered.

In Chapter 5, we present the first reaction nanoscopy data taken at a wavelength of 2 μm for a set of laser polarizations of different ellipticity and a range of intensities. The data serve to explore the limits of the theoretical model introduced in Chapter 2 and successfully applied in Chapter 4. While the model reproduces the angular distribution of the emitted ions, their energy is not predicted correctly across the entire parameter space. We discuss possible reasons for the observed discrepancies and provide experimental justification for a part of the underlying assumptions of the model. Equally relevant to the model, the surface composition of the silica nanoparticles was investigated in a solvent exchange experiment. We find that the solvent does not play a significant role in reaction nanoscopy experiments. It is rather the covalently bound functional groups on the nanoparticle surface and the nanoparticle material itself, which determine the ion spectra. This insight is of great value for the future development of the theoretical model as well as for the design of reaction nanoscopy experiments targeted at the observation of chemical reactions.

Driven by the findings about the ion origin, systems with a more controllable molecular surface structure, namely droplets, are investigated in Chapter 6. Droplets comprise the same molecules on the surface as in the bulk, allowing chemically well-controlled experiments. We used the reaction nanoscope to study polydisperse droplets of propanediol and characterize their average size based on the angle of maximum field enhancement measured from the angular ion distribution. The energy measurement in the reaction nanoscope moreover allows an estimate of the droplet charge and an assessment of the droplet stability after ionization. We interpret the reaction nanoscopy ion data from both isomers of propanediol to extract droplet-specific as well as isomer-specific effects in the ion emission process. In combination with density functional theory calculations for the molecular structure on the droplet surface, the results suggest that the ion yields from

droplets are influenced by the molecular alignment on the surface.

List of publications by the author

Publications with direct relevance to this thesis:

1. P. Rosenberger, R. Dagar, W. Zhang, A. Majumdar, M. Neuhaus, M. Ihme, B. Bergues, and M. F. Kling. "Reaction Nanoscopy of Ion Emission from Sub-wavelength Propanediol Droplets", *arXiv:2212.05587 [physics.chem-ph]*

2. P. Rosenberger, R. Dagar, W. Zhang, A. Sousa-Castillo, M. Neuhaus, E. Cortes, S. A. Maier, C. Costa-Vera, M. F. Kling, and B. Bergues. "Imaging elliptically polarized infrared near-fields on nanoparticles by strong-field dissociation of functional surface groups", *European Physical Journal D* 76, 109 (2022)

3. W. Zhang, R. Dagar, P. Rosenberger, A. Sousa-Castillo, M. Neuhaus, W. Li, S.A. Khan, A. S. Alnaser, E.Cortes, S. A. Maier, C. Costa-Vera, M. F. Kling, and B. Bergues. "All-optical nanoscopic spatial control of molecular reaction yields on nanoparticles", *Optica* 9, 551-560 (2022)

4. M. S. Alghabra, R. Ali, V. Kim, M. Iqbal, P. Rosenberger, S. Mitra, R. Dagar, P. Rupp, B. Bergues, D. Mathur, M. F. Kling, and A. S. Alnaser, "Anomalous formation of trihydrogen cations from water on nanoparticles", *Nature Communications* 12, 3839 (2021)

5. P. Rosenberger, P. Rupp, R. Ali, M. S. Alghabra, S. Sun, S. Mitra, S. Khan, R. Dagar, V. Kim, M. Iqbal, J. Schötz, Q. Liu, S. Sundaram, J. Kredel, M. Gallei, C. Costa-Vera, B. Bergues, A. S. Alnaser, and M. F. Kling, "Near-Field Induced Reaction Yields from Nanoparticle Clusters", *ACS Photonics* 7, 7, 1885–1892 (2020)

6. P. Rupp, C. Burger, N. G. Kling, M. Kübel, S. Mitra, P. Rosenberger, T. Weatherby, N. Saito, J. Itatani, T. Otsuka, A. S. Alnaser, M. B. Raschke, E. Rühl, A. Schlander, M. Gallei, L. Seiffert, T. Fennel, B. Bergues, and M. F. Kling, "Few-cycle laser driven reaction nanoscopy on aerosolized silica nanoparticles", *Nature Communications* 10, 4655 (2019)

Other publications:

1. A. C. LaForge, J. D. Asmussen, B. Bastian, M. Bonanomi, C. Callegari, S. De, M. Di Fraia, L. Gorman, S. Hartweg, S. R. Krishnan, M. Kling, D. Mishra, S. Mondal, A. Ngai, N. Pal, O. Plekan, K. C. Prince, P. Rosenberger, E. Serrata, F. Stienkemeier, N. Berrah, and M. Mudrich. "Relaxation dynamics in excited helium nanodroplets probed with high resolution, time-resolved photoelectron spectroscopy", *Physical Chemistry Chemical Physics* 24, 28844-28852 (2022)

2. J. Blöchl, J. Schötz, A. Maliakkal, N. Šreibere, Z. Wang, P. Rosenberger, P. Hommelhoff, A. Staudte, P. B. Corkum, B. Bergues, and M. F. Kling, "Spatiotemporal sampling of near-petahertz vortex fields", *Optica* 9, 755-761 (2022)

3. J. Schötz, A. Maliakkal, J. Blöchl, D. Zimin, Z. Wang, P. Rosenberger, M. Alharbi, A. M. Azzeer, M. Weidman, V. S. Yakovlev, B. Bergues, and M. F. Kling, "The emergence of macroscopic currents in photoconductive sampling of optical fields", *Nature Communications* 13, 962 (2022)

4. S. Li, T. Driver, P. Rosenberger, E. G. Champenois, J. Duris, A. Al-Haddad, V. Averbukh, J. C. T. Barnard, N. Berrah, C. Bostedt, P. H. Bucksbaum, R. N. Coffee, L. F. DiMauro, L. Fang, D. Garratt, A. Gatton, Z. Guo, G. Hartmann, D. Haxton, W. Helml, Z. Huang, A. C. LaForge, A. Kamalov, J. Knurr, M. Lin, A. A. Lutman, J. P. MacArthur, J. P. Marangos, M. Nantel, A. Natan, R. Obaid, J. T. O'Neal, N. H. Shivaram, A. Schori, P. Walter, A. L. Wang, T. J. A. Wolf, Z. Zhang, M. F. Kling, A. Marinelli, and J. P. Cryan, "Attosecond coherent electron motion in Auger-Meitner decay", *Science* 375, 6578, 285-290 (2022)

5. J. Schötz, L. Seiffert, A. Maliakkal, J. Blöchl, D. Zimin, P. Rosenberger, B. Bergues, P. Hommelhoff, F. Krausz, T. Fennel, and M. F. Kling, "Onset of charge interaction in strong-field photoemission from nanometric needle tips", *Nanophotonics* 10, 14, 3769-3775 (2021)

6. T. Mizuno, N. Ishii, T. Kanai, P. Rosenberger, D. Zietlow, M. F. Kling, O. Tolstikhin, T. Morishita, and J. Itatani, "Observation of the quantum shift of a backward rescattering caustic by carrier-envelope phase mapping", *Physical Review A* 103, 043121 (2021)

7. A. Korobenko, P. Rosenberger, J. Schötz, A. Yu. Naumov, D. M. Villeneuve, M. F. Kling, A. Staudte, P. B. Corkum, and B. Bergues, "Single-shot dispersion sampling for optical pulse reconstruction", *Optics Express* 29, 11845 (2021)

8. M. Kubullek, Z. Wang, K. von der Brelje, D. Zimin, P. Rosenberger, J. Schötz, M. Neuhaus, S. Sederberg, A. Staudte, N. Karpowicz, M. F. Kling, and B. Bergues, "Single-shot carrier–envelope-phase measurement in ambient air", *Optica* 7, 35 (2020)

9. T. Driver, S. Li, E. G. Champenois, J. Duris, D. Ratner, T. J. Lane, P. Rosenberger, A. Al-Haddad, V. Averbukh, T. Barnard, N. Berrah, C. Bostedt, P. H. Bucksbaum, R. Coffee, L. F. DiMauro, L. Fang, D. Garratt, A. Gatton, Z. Guo, G. Hartmann, D. Haxton, W. Helml, Z. Huang, A. LaForge, A. Kamalov, M. F. Kling, J. Knurr, M. Lin, A. A. Lutman, J. P. MacArthur, J. P. Marangos, M. Nantel, A. Natan, R. Obaid, J. T. O'Neal, N. H. Shivaram, A. Schori, P. Walter, A. L. Wang, T. J. A. Wolf, A. Marinelli, and J. P. Cryan, "Attosecond transient absorption spooktroscopy: a ghost imaging approach to ultrafast absorption spectroscopy", *Physical Chemistry Chemical Physics* 22, 2704-2712 (2020)

10. S. A. Bozpolat, P. Rosenberger, M. F. Ciappina, M. F. Kling, and I. Yavuz, "Carrier-envelope-phase–controlled molecular dissociation by ultrashort chirped laser pulses", *Physical Review A* 100, 063409 (2019)

11. J. Duris, S. Li, T. Driver, E. G. Champenois, J. P. MacArthur, A. A. Lutman, Z. Zhang, P. Rosenberger, J. W. Aldrich, R. Coffee, G. Coslovich, F. Decker, J. M. Glownia, G. Hartmann, W. Helml, A. Kamalov, J. Knurr, J. Krzywinski, M. Lin, J. P. Marangos, M. Nantel, A. Natan, J. O'Neal, N. Shivaram, P. Walter, A. Wang, J. J. Welch, T. J. A. Wolf, J. Z. Xu, M. F. Kling, P. H. Bucksbaum, A. Zholents, Z. Huang, J. P. Cryan, and A. Marinelli, "Tunable isolated attosecond X-ray pulses with gigawatt peak power from a free-electron laser", *Nature Photonics* 14, 30 (2019)

12. I. Yavuz, J. Schötz, M. F. Ciappina, P. Rosenberger, Z. Altun, M. Lewenstein, and M. F. Kling, "Control of molecular dissociation by spatially inhomogeneous near fields", *Physical Review A* 98, 043413 (2018)

13. C. Burger, A. Atia-Tul-Noor, T. Schnappinger, H. Xu, P. Rosenberger, N. Haram, S. Beaulieu, F. Légaré, A. S. Alnaser, R. Moshammer, R. T. Sang, B. Bergues, M. S. Schuurman, R. de Vivie-Riedle, I. V. Litvinyuk and M. F. Kling, "Time-resolved nuclear dynamics in bound and dissociating acetylene", *Structural Dynamics* 5, 044302 (2018)

Chapter 2

Theoretical model

As part of this thesis, a model for describing the strong-field ion emission from clusters of nanoparticles was developed. The model was later adapted for single nanoparticles and more complicated laser polarization states [50], as well as multi-color light fields [49]. It is inspired by the M^{3}C model [51], which was used for the description of the initial reaction nanoscopy results by Rupp et al. [47]. M^{3}C is short for Mie-field, mean-field, Monte-Carlo. The M^{3}C model was originally developed for modeling the photoemission of electrons from nanoparticles and has successfully been applied to a variety of different experimental conditions [46]. However, the M^{3}C code only describes the light-matter interaction for single nanoparticles and is thus not suited for the description of nanoparticle clusters, which was the initial motivation for the development of a different approach. The second reason for using a different model was the insight that the precise details of the electron dynamics are not crucial for the reproduction of the major features of the experimental results of strong-field ion emission from nanoparticles [49, 50, 52]. Omitting electron trajectory calculations leads to a faster run time and thus allows averaging over many different configurations, which was essential for the description of the experiments on randomly oriented nanoparticle clusters. The following paragraph contains a brief summary of the concepts of the M^{3}C model and describes how they were adapted for an optimized description of the ion momentum spectroscopy experiments.

2.1 General description

In the M^{3}C model, the strong-field electron ionization of the naoparticles is described by the quasi-static Ammosov-Delone-Krainov (ADK) ionization rate [53] using the ionization potential of the nanoparticle material. Ionization rates like ADK are typically used for atomic and molecular systems, where the electric field used as the input for ADK rate calculations is usually homogeneous in space. In the M^{3}C model, however, the response of the nanosystem is taken into account for the calculation of a spatially and temporally varying electric field. This electric field is composed of the optical response of the nanosphere, the so-called Mie field [40], and the Coulomb field due to the charges generated over time, i.e.,

the mean field. There are two types of charges, electrons and positively charged mother ions. The mother ions remain at their initial position throughout the simulation while the electrons are propagated classically in the total electric field (Mie field + mean field). For the first study using the reaction nanoscopy technique by Rupp et al. [47], the M^{3}C model was extended by placing protons at a small distance to the surface and including them in the time propagation starting from the most intense peak of the laser pulse. The generation probability of the protons was modeled by an intensity-dependent power law assuming that the proton generation is achieved via multi-photon ionization [54] of molecules adsorbed on the nanoparticle surface. In this adapted M^{3}C code, the protons themselves did not contribute to the mean field and consequently did not influence the electron trajectories and the trajectories of other protons.

The model developed here uses a similar semi-classical approach, and the ionization of the nano surface is also described by the ADK rate. However, the input for the ADK rate, the electric field, is assumed to be dominated by the optical near-field. The contribution of charge interactions to the ionization rate is thus neglected. The idea behind this assumption is similar to the strong-field approximation in atomic and molecular strong-field ionization [55] where the influence of the ion's Coulomb potential on the outgoing electron is neglected due to the presence of a strong electric field. The other difference to the M^{3}C approach is that the electrons are neglected in our model, as mentioned above. When a nanoparticle is ionized by a strong laser pulse, many electrons are generated with a broad distribution of energies [46]. However, only the most energetic electrons can escape from the vicinity of the nanoparticle, leaving a net positive charge on the nanoparticle surface. This positive charge traps low energy electrons close to the nanoparticle surface [43]. Our model neglects the microscopic details of the interaction between the trapped electrons and the emitted ions. Doing so is justified by the fact that individual electrons scattering from outgoing ions can not efficiently change the ion momentum due to the low electron mass compared to the mass of a proton. On the nanoparticle scale, however, the trapped electrons lower the nanoparticle's effective charge, reducing the repulsive force on the ions and, thus, the ions' final kinetic energy. In the model, the total charge of the particle is constant during the emission of the ions. This means that the shielding effect by trapped electrons is treated statically, which is a valid approximation due to the long time scale of the ion emission (ps to ns) compared to the time scale of electron generation (the pulse duration, i.e., fs). As in Ref. [47], the outgoing ions (protons in our case) are generated based on a power law, propagated independently of each other in the static field of the mother ions, and their final momentum is extracted. The following sections contain more detailed explanations of the different parts of the model mentioned here.

2.2 Electric field calculations

The basis for the generation of all charges in the model is the electric near-field around the nanoparticle or nanoparticle cluster in response to an incoming plane-wave laser pulse. This linear response can be efficiently calculated for a single spherical object using the

Mie solution of Maxwell's equations but requires more advanced techniques when more than one particle is present. Such techniques are the T-matrix approach [56–58] for solving Maxwell's equations by coupling the single particle solutions or the discretization of the equations on a spatio-temporal grid in the FDTD method (FDTD = finite-difference time-domain). In our case, the FDTD method was chosen due to readily available commercial solvers and the flexibility of the approach. We calculated the near-field on a regular cubic grid using the Lumerical FDTD software package. From the time- and space-dependent electric field on the grid, the local field enhancement factor α for every point $\mathbf{r}$ on the grid was calculated as:

$$\alpha(\mathbf{r}) = \frac{\max_t |\mathbf{E}_{\mathrm{FDTD}}(\mathbf{r}, t)|}{\max_t |\mathbf{E}_{\mathrm{in}}(t)|}. \tag{2.1}$$

Here $\mathbf{E}_{\mathrm{FDTD}}$ is the field obtained by the FDTD simulation and $\mathbf{E}_{\mathrm{in}}(t)$ is the incoming electric field of the laser pulse. The simulations used a Gaussian for the temporal envelope of the pulse:

$$\mathbf{E}_{\mathrm{in}}(t) = \sin(-\omega_0 t + \varphi) \exp(-t^2/2\delta_t^2)\mathbf{e}_{\mathrm{p}}, \tag{2.2}$$

where ω_0 is the central frequency, φ is the carrier-envelope phase, δ_t is the pulse duration, and $\mathbf{e}_{\mathrm{p}}$ is a unit vector pointing along the direction of the linear polarization. The expressions for spherical and general elliptical polarization are derived in the appendix. The minus sign in the sine function is a convention of the FDTD software. The quantity δ_t relates to the full width at half-maximum (FWHM) of the intensity envelope T_{FWHM} in the following way:

$$\delta_t = \frac{T_{\mathrm{FWHM}}}{2\sqrt{\ln 2}} \tag{2.3}$$

In the following, any pulse duration given refers to the FWHM duration T_{FWHM}.

A typical grid spacing of 3 nm, 200 grid points along every spatial dimension, and a similar number of time steps in a single FDTD run leads to large amounts of data. Reading the simulation data back into the code for ionization and ion propagation can therefore be the bottleneck of the overall performance. This is especially undesirable when large parameter scans are necessary, as in the case of averaging over different dimer orientations. For this reason, the FDTD solution was approximated by rescaling the incident electric field with the field enhancement factor at the corresponding grid point:

$$\mathbf{E}_{\mathrm{FDTD}}(\mathbf{r}, t) \approx \alpha(\mathbf{r})\mathbf{E}_{\mathrm{in}}(t) \equiv \mathbf{E}(\mathbf{r}, t). \tag{2.4}$$

This approximation was selectively compared with the full FDTD solution. For the systems studied in this thesis, no significant impact on the ion emission results was found.

2.3 ADK rate and ionization probability

The ionization of the surface of the nanoparticle or cluster was described by a simple two-state model where the states are coupled by the ADK ionization rate γ, as illustrated in Fig. 2.1a. An electron of an atom on the surface of the nanosystem is with probabilities P_b

and P_f either in a bound state or a free state, respectively. The interaction of the system with a strong laser pulse $E(t)$ leads to a non-zero, time-dependent ionization rate $\gamma(E(t))$ and to population transfer between the states, which is expressed by the following system of ordinary differential equations (analogous to the approach in Ref. [59]):

$$\frac{\mathrm{d}P_b}{\mathrm{d}t} = -\gamma(E(t))P_b, \tag{2.5}$$

$$\frac{\mathrm{d}P_f}{\mathrm{d}t} = -\frac{\mathrm{d}P_b}{\mathrm{d}t} = +\gamma(E(t))P_b. \tag{2.6}$$

Before the arrival of the laser pulse, at $t = -\infty$, the probability for the bound state is one $P_b(t = -\infty) = 1$, and the free state is unoccupied $P_f(t = -\infty) = 0$. With these initial conditions, the solution of this system for $P_f(t)$ is given by:

$$P_f(t) = 1 - \exp\left[-\int_{-\infty}^{t} \mathrm{d}t'\, \gamma(E(t'))\right]. \tag{2.7}$$

The ionization probability for an atom exposed to a laser pulse is then given by the value $P_f(\infty)$. At this point, it is important to stress the difference between the ionization rate, which describes population transfer, and the ionization probability, which describes the population itself. For practical purposes, the limit $t \to \infty$ is replaced by a final time t_f that is large enough such that $P_f(t_f)$ has converged within the desired accuracy. Due to the exponential dependence of the ADK rate γ on the electric field $E(t)$, only the strongest half-cycles of the field need to be included in the integral to reach convergence. This effect is illustrated in Fig. 2.1b, where the ADK rate for a laser pulse with a central wavelength of $2\,\mu$m is shown. The plot only contains those half-cycles of the electric field, which have a significant contribution to the ionization probability in Fig. 2.1c. For this example, the final population of the free state is already reached three half cycles after $t = 0$, i.e., $P_f(t = \infty) \approx P_f(t = t_f = 10\,\mathrm{fs})$.

For the nanosystem, the electric field and thus the ionization probability varies across the surface. Instead of calculating the ionization probability on the fly, the approximation made in Eq. (2.4) allows for a more efficient approach since the polarization and the temporal evolution of the field are approximated as constant across space and only the field amplitude changes. The ionization probability can thus be calculated for the laser pulse corresponding to the lowest field in the simulation volume, for the pulse at the highest field, and for a small number of points in between. With sufficiently many intermediate points, the ionization probabilities for all other field enhancement values can then be obtained by interpolation. This approach is illustrated in Fig. 2.1d.

The same sub-figure shows that the total ionization probability in this model behaves very differently for different regimes of field amplitude. For very high fields, the full depletion of the bound state leads to a saturation of the ionization probability, and a value constant for $P_f(t = \infty) \approx 1$. Mathematically, the depletion occurs when the exponential term in Eq. (2.7) approaches zero, i.e., when the time integral of the ADK rate becomes large:

$$\int_{-\infty}^{t} \mathrm{d}t'\, \gamma(E(t')) \gg 1 \quad \longrightarrow \quad P_f(t = \infty) \approx 1 \ \text{(saturation)}. \tag{2.8}$$

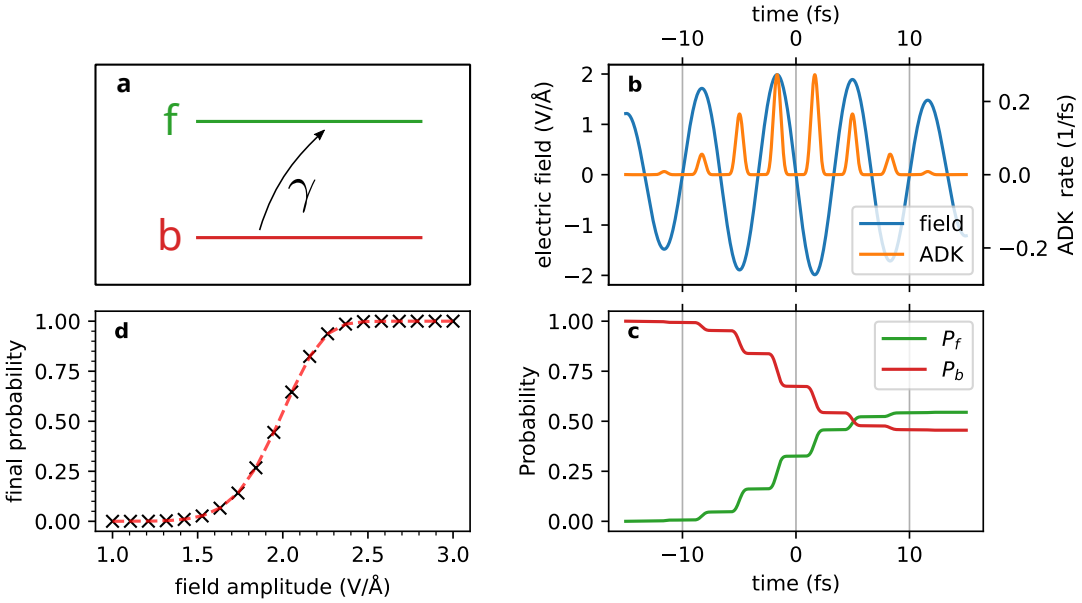

Figure 2.1: Ionization rate and ionization probability for a single atom. **a:** Schematic depicting the population transfer between the bound state b and the free state f due to the ionization rate γ. **b:** The electric field (blue line) of a laser pulse with a central wavelength of 2 μm and a full-width-at-half-maximum duration of the intensity envelope of 25 fs. The corresponding ADK ionization rate for the ionization potential of silica ($I_p = 10.2\,\text{eV}$, see [60]) is shown in orange. **c:** The probabilities P_b and P_f of the bound state and the excited state, respectively, as a function of time. **d:** The final probability $P_f(t = \infty)$ as a function of the field amplitude of the laser pulse. The crosses show the points where the probability was calculated using Eq. (2.7), and the dashed line shows a linear interpolation used for approximating the ionization probability in the simulations.

For intermediate field strengths, the ionization probability scales linear with field amplitude, and for low electric fields, it is proportional to the time integral of the ADK rate. This can be shown by Taylor-expanding the exponential of Eq. (2.7) to first order:

$$P_f(t) \approx 1 - \underbrace{\left[1 - \int_{-\infty}^{t} \mathrm{d}t'\, \gamma(E(t'))\right]}_{\exp(-x)\approx 1-x} = \int_{-\infty}^{t} \mathrm{d}t'\, \gamma(E(t')). \tag{2.9}$$

2.4 Generation of static surface charges

2.4.1 Rejection sampling

As mentioned above, the model uses static, positive point charges to describe the combined effect of the ionized atoms on the particle surface and the shielding due to the trapped electrons close to the surface. The surface charges in the simulation sampled from the spatial distribution of the ADK-based ionization probabilities using the rejection sampling technique [61]. In short, rejection sampling works by randomly generating candidate samples, which are accepted or rejected based on the target distribution and a uniform random number. If done correctly, the accepted samples follow the target distributions. Even though the rejection sampling method can be applied to discrete distributions as given by the FDTD grid, a continuous distribution of charges in space was more desirable for the simulations. In the discrete case, charges could only be generated exactly at the grid points, which would lead to artifacts in the simulation or require excessively fine FDTD grids. In order to avoid this, the electric field from the FDTD simulations (Eq. (2.4)) was linearly interpolated such that an ionization probability could be calculated for every point in space. This approach is visualized in Fig. 2.2 for a one-dimensional probability distribution. The necessary steps for rejection sampling in three-dimensional space, as applied in the model, are described in the following sections.

2.4.2 Candidate generation

The candidate samples for the placement of the static surface charges were obtained by generating uniformly and randomly distributed position vectors in a thin layer below the nanoparticle surface. First, three Gaussian random numbers $\mathbf{g} = (g_x, g_y, g_z)$ were drawn. These random coordinates were then normalized to obtain a set of random numbers that are uniformly distributed on the surface of a three-dimensional unit sphere around the coordinate origin[62, 63]:

$$\hat{\mathbf{g}} = \frac{\mathbf{g}}{\|\mathbf{g}\|} = \frac{\mathbf{g}}{\sqrt{g_x^2 + g_y^2 + g_z^2}} \tag{2.10}$$

Afterward, the random positions were rescaled with a factor of $R - \delta R$, where R is the nanosphere radius, and δR is a small, positive number drawn from a uniformly random distribution. This scheme results in a set of candidate positions that are distributed uniformly and randomly within a thin layer δR underneath the surface of a sphere with a

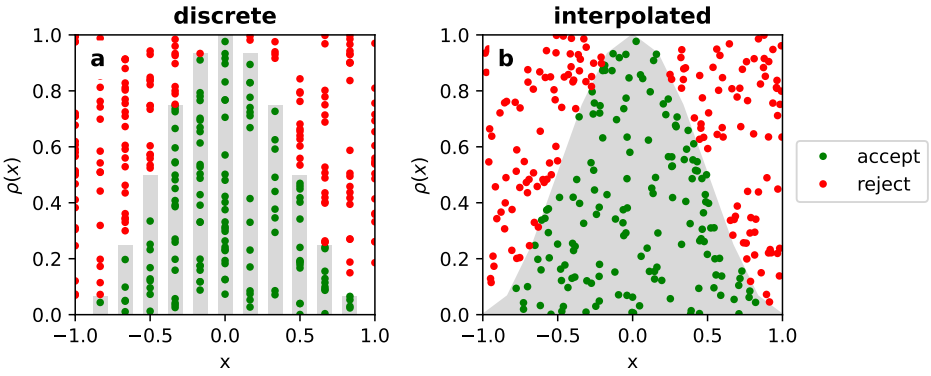

Figure 2.2: Example for sampling a distribution using the rejection method. The points (x_i, u_i) in red and green are pairs of candidate sample values x_i (uniformly distributed in $[-1, 1]$) and uniformly distributed random numbers $u_i \in [0, 1]$. Candidates x_i are accepted as samples if $u_i \leq \rho(x_i)$, where ρ is the probability density (gray shading). Accepted samples are displayed in green, and rejected samples in red. **a:** A discrete probability distribution. **b:** The interpolated, continuous version of the distribution in panel a.

radius R. The extension of the candidate generation to nanoparticle clusters is straightforward: For every particle of the cluster, an equal number of candidates are generated using the algorithm described above. For a two-particle cluster, for example, $2N$ candidates are generated, N of them are shifted to the center of the first particle $\mathbf{r}_1$, and the other N are shifted to the center of the second particle $\mathbf{r}_1$. In summary, a single candidate position $\mathbf{p}$ for a particle at position $\mathbf{r}_n$ is obtained as:

$$\mathbf{p} = (R - \delta R)\hat{\mathbf{g}} + \mathbf{r}_n. \tag{2.11}$$

2.4.3 Candidate acceptance

Candidates in rejection sampling are rejected or accepted based on the value of the probability ρ at the candidate position $\mathbf{p}$ and a random number u that is compared to $\rho(\mathbf{p})$. The probability distribution of u, denoted as $U(\mathbf{p})$ must be chosen such that

$$cU(\mathbf{p}) \geq \rho(\mathbf{p}) \tag{2.12}$$

for all points $\mathbf{p}$, where c is a constant [64]. In our case, the random number u was chosen to be distributed uniformly random between zero and the maximum ionization probability $\rho_{\max}$. The ionization probability is a monotonously increasing function of the electric field and, therefore, also of the field enhancement $\alpha(\mathbf{r})$. The maximum ionization probability $\rho_{\max}$ could thus be obtained by finding the maximum field enhancement on the FDTD grid and calculating the corresponding ionization probability.

With these parameters, a candidate position $\mathbf{p}$ is accepted for the placement of a static charge if:

$$\rho(\mathbf{p}) \leq u. \tag{2.13}$$

In Fig. 2.3c, the angular distribution of 1000 accepted candidates is shown. The example illustrates the case of a relatively low field amplitude where the field distribution is much wider than the charge distribution.

In principle, the shape of U can be chosen as non-uniform as long as Eq. (2.12) is satisfied for all $\mathbf{p}$. This can be used to increase the relative amount of accepted samples if the shape of U resembles the shape of ρ. However, in practice, it is extremely challenging to generate such non-uniform random numbers computationally efficient while ensuring that Eq. (2.12) is not violated, especially for a three-dimensional domain, as is the case here.

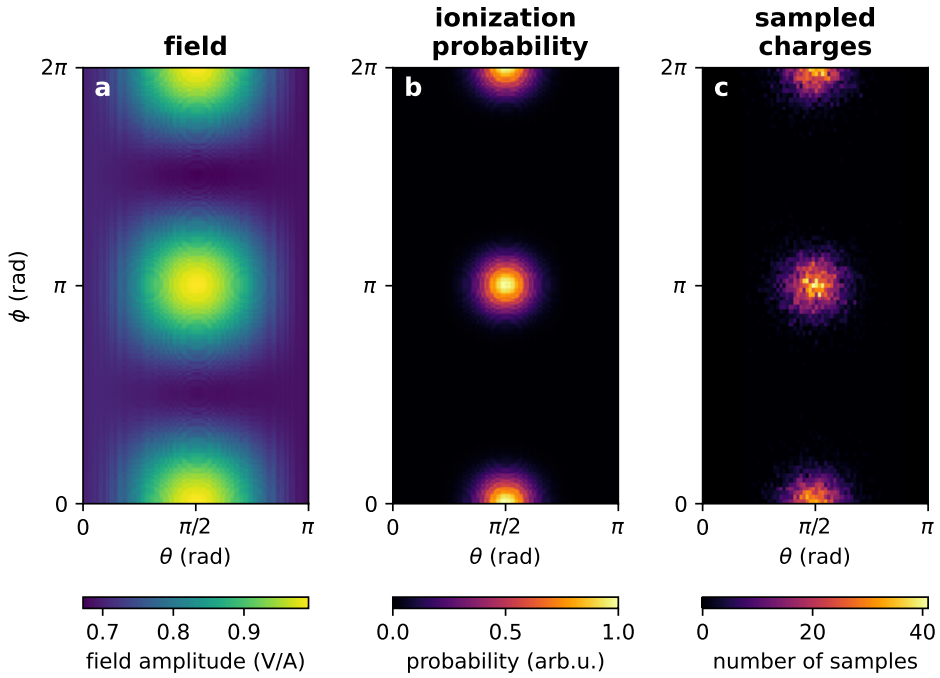

Figure 2.3: **a:** The electric field distribution on the surface of a silica nanoparticle with a diameter of 300 nm illuminated with a 25 fs, 2 μm linearly polarized laser pulse. The result was obtained from an FDTD simulation on a grid with 3 nm spacing in all directions. **b:** The ionization probability corresponding to the field displayed in panel a, calculated via Eq. (2.7). **c:** Histogram of a sample of 10k point charges obtained from the distribution of panel b.

2.4.4 Total charge

The rejection algorithm described above does obviously not fix the maximum number of samples to be drawn from a distribution. In physical terms, however, the number of accepted candidate positions is equivalent to the number of elementary charges placed on the surface of the nanosystem and will thus have an impact on the charge dynamics. It is, therefore, necessary to calculate the total ionization probability for obtaining the total

charge and, thereby, the number of required samples. The ionization probability per atom is given by $P_f(t = \infty)$, as introduced above. The density of generated charges per unit volume is obtained by multiplying $P_f(t = \infty)$ with the number density n of the nanoparticle material. Finally, the total charge Q on the surface is obtained by integrating the obtained charge density over space:

$$Q = \int_S \mathrm{d}V \, P_\infty(\mathbf{r}) n = \int_S \mathrm{d}V \, \rho(\mathbf{r}). \tag{2.14}$$

Here, S represents the thin surface layer of the nanoparticle or all the surface layers for all the particles of a nanoparticle cluster, respectively. The expression $P_\infty(\mathbf{r})$ is used as a shorthand for the ionization probability $P_f(t = \infty)$ at a point $\mathbf{r}$.

Carrying out this multidimensional integral can be elegantly achieved by reusing the candidate generation scheme described above for a Monte-Carlo integration (see, for instance, [61, 64]). The candidate positions are generated uniformly random within the surface layer of the system. This means that the candidate density is a constant $c = 1/V$, where V is the volume of the surface layer. The expectation value of the charge density $\rho(\mathbf{r})$ under the constant candidate density can formally be expressed as:

$$\langle \rho(\mathbf{r}) \rangle_c = \int_S \mathrm{d}V \, \rho(\mathbf{r}) c = \frac{1}{V} \int_S \mathrm{d}V \, \rho(\mathbf{r}) = \frac{Q}{V}, \tag{2.15}$$

where we have used Eq. (2.14) to replace the integral over space with the total charge of the system Q. Eq. (2.15) shows that the charge Q could be calculated if the expectation value $\langle \rho(\mathbf{r}) \rangle_c$ was known. It can be approximated using the sampled, uniformly distributed candidate positions. With N candidates generated with positions $\mathbf{r}_i$ in the surface layer, the value of $\langle \rho(\mathbf{r}) \rangle_c$ can be estimated by sample averaging:

$$\langle \rho(\mathbf{r}) \rangle_c \approx \frac{1}{N} \sum_{i=1}^{N} \rho(\mathbf{r}_i). \tag{2.16}$$

The total charge can thus be approximated by the Monte-Carlo integral:

$$Q = V \langle \rho(\mathbf{r}) \rangle_c \approx \frac{V}{N} \sum_{i=1}^{N} \rho(\mathbf{r}_i). \tag{2.17}$$

While Monte-Carlo integration is not the most efficient integration method, it was sufficiently fast for the charge calculations and came at the large advantage of being easily applicable to both single nanoparticles and nanoparticle clusters. Due to the rather slow convergence of Monte-Carlo integrals with $\mathcal{O}(1/\sqrt{N})$ [64], the number of candidate samples needs to be high enough for sufficient accuracy of the total charge. This has been checked in the code by repeating the integration multiple times and ensuring that the variance between the results is small enough.

2.5 Ion generation and propagation

Apart from the static charge on the nanosurface, the model also considers non-static, mobile ions. In the experiments, they are generated by the dissociative ionization of molecules and functional groups on the nanoparticle. They are accelerated by Coulomb repulsion from the surface and their final momentum is observed with the reaction nanoscope. For the case of the silica nanoparticles studied here, the exact surface composition depends on the solvent that the particles are stored in as well as, in the case of an aerosol injection, the evaporation conditions (see Chapter 5). The ion generation model used here was adapted from the approach introduced by Rupp et al. [47]. It assumes that the surface constituents are ionized in a multi-photon fashion. This means that the ion yield Y is proportional to the laser intensity I taken to the power of the number of photons n needed to overcome the ionization potential I_p:

$$Y \propto I^n = I^{I_p/\hbar\omega}, \tag{2.18}$$

where $\omega = 2\pi f$ is the angular frequency of the light field. The intensity $I = I(\mathbf{r})$ is the position-dependent peak intensity around the irradiated nanoparticle. To restrict the ion generation to an area close to the surface of the nanosystem, Y was further multiplied with a Gaussian along the radial coordinate:

$$Y(\mathbf{r}) \propto I^n(\mathbf{r}) \cdot \exp\left(-\frac{(r-R)^2}{2\sigma_r^2}\right) \tag{2.19}$$

The standard deviation of the Gaussian is given by σ_r, and the mean is set to the nanoparticle radius R. This expression holds for a single nanoparticle centered around the coordinate origin, with $r = \|\mathbf{r}\|$. For N nanoparticles at positions $\mathbf{R_i}$ and radii R_i, the formula is generalizes to:

$$Y(\mathbf{r}) \propto I^n(\mathbf{r}) \cdot \sum_{i=1}^{N} \exp\left(-\frac{(\|\mathbf{R_i} - \mathbf{r}\| - R_i)^2}{2\sigma_r^2}\right) \tag{2.20}$$

The ions in the simulation only interact with the static charges on the surfaces but not with each other. This means that the number of charges sampled from the distribution $Y(\mathbf{f})$ only affects the statistics of the simulation but has no influence on individual ion trajectories. For this reason, it is sufficient to define $Y(\mathbf{r})$ proportionally and only up to an arbitrary normalization constant.

The initial positions of the mobile ions are sampled by rejection sampling, as described above. They are then propagated in the static electric field of the surface charges. The electric field acting on a mobile ion at position $\mathbf{r}$ is approximated by summing over all the static point charges:

$$\mathbf{E} = \frac{e}{4\pi\varepsilon_0} \sum_{i=1}^{N_s} \frac{\mathbf{r} - \mathbf{r}_i}{\|\mathbf{r} - \mathbf{r}_i\|^3} \tag{2.21}$$

This approximation neglects the potential due to the material polarization induced by the point charges under the surface (and by the mobile ion). Expressions for the polarization

potential can be obtained by solving Maxwell's equations for a point charge inside or in the vicinity of a dielectric sphere. The solution for this system can either be represented by a multipole expansion around the coordinate origin [43], or by an image charge density [65, 66]. The solution via the latter approach can be further simplified by approximating the charge density by a set of point charges using Radau quadrature [67, 68]. As Fig. 2.4 shows, for small distances, the difference between the pure Coulomb potential and the full potential (including polarization) can be significant. The polarized dielectric material shields the charge and thus reduces the potential energy in the field. In the simulation, the effect of polarization was neglected for multiple reasons:

- Description of clusters: The polarization of a nanocluster cannot be represented as simply as for a single sphere
- Computational cost: The introduction of mirror charges or the expansion in multipoles increases the computational cost
- Other error sources: The error resulting from an inaccurate intensity and pulse characterization in the experiment and the error from neglecting electron-ion interaction are likely to have a larger influence than neglecting the polarization field. The model is an effective model in this sense: The shielding by dielectric polarization can be compensated by fitting the intensity (within the experimental bounds) and producing fewer surface charges.

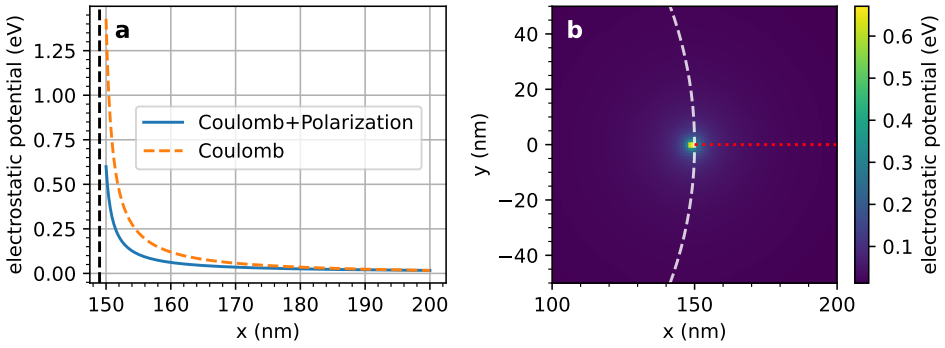

Figure 2.4: Potential due to a point charge inside a dielectric sphere with a radius of 150 nm. The sphere is centered around the coordinate origin, and the charge is placed at (149 nm,0,0). A set of 30 image charges [67] was used to approximate the polarization potential of the dielectric. A relative permittivity of $\varepsilon_r = 3.9$ was chosen. This simulates the extreme case of a DC material response for silica [69] (for high frequencies, ε_r is smaller). **a:** Potential energy of an elementary test charge along the x-axis (red dotted line in panel b). The blue line includes the effect of the dielectric polarization, the orange dashed line does not. The black dashed line indicates the position of the point charge generating the potential. **b:** The electrostatic potential energy (Coulomb + polarization) in the plane $z = 0$. The surface of the sphere is indicated by the white dashed line.

The propagation of the mobile ions was achieved by integrating Newton's equations of motion using an off-the-shelf solver for ordinary-differential-equations [70]. Ions were

propagated until their momentum did not change significantly anymore from one time step to the next. At this point, due to the infinite range of the Coulomb potential, the potential energy of the ion has not yet been fully converted into kinetic energy. The momentum vector of the ion is thus rescaled to match the total energy. This scheme assumes that the ion has propagated far enough away from the nanoparticle that only the length of its momentum vector might still change while the direction remains fixed.

For single nanoparticles, combining the individual final ion momenta into histograms for further analysis is a trivial task. For clusters, however, different alignments correspond to different near-field distributions and thus a different total ion yield. Ion histograms for different alignments thus need to be weighted by the total ion yield for obtaining the averaged result. The total ion yield is proportional to the integral of $Y(\mathbf{r})$ over the entire space. This integral was calculated for every alignment by Monte-Carlo integration in analogy to the determination of the total surface charge, with the modification that the random numbers were drawn uniformly inside the entire FDTD volume and not only from a surface layer. Importantly, while the proportionality constant for $Y(\mathbf{r})$ is arbitrary (see Eq. (2.18)), it needs to be chosen before and kept constant during the entire alignment averaging procedure in order to obtain correct results. The orientation-averaged ion momentum histograms can then be compared to the momenta measured via the reaction nanoscopy technique, introduced in the next chapter.

Chapter 3

Experimental Methods

All nanoparticle and droplet measurements described in this thesis were carried out with reaction nanoscopy setups. The data on nanoparticle clusters were collected at the American University of Sharjah (AUS), and the other datasets were collected at the Ludwig-Maximilians-Universität (LMU) in Munich. The reaction nanoscopy technique was first introduced by Rupp et al. [47] and is described in much detail in Ref. [71]. The reaction nanoscope is designed for momentum spectroscopy of ions generated from the strong-field ionization of aerosolized nanoparticles, droplets, and other nanosystems. This chapter is an introduction to the reaction nanoscopy technique. It will give an overview of all the involved parts, including the aerosol generation, the particle detection, and the momentum reconstruction.

3.1 Aerosol generation

The aerosol generation setups were similar for both, the silica nanoparticle studies and the droplet investigations. The setups are shown in Fig. 3.1. In the following, both setups will be described separately and independently for ease of reading.

3.1.1 Aerosolization of silica nanoparticles

Silica nanoparticles produced by the Stöber method [72] with a diameter of 300 nm were obtained from collaborations with different research groups. The group of Prof. Dr. Markus Gallei from Saarland University provided the samples for the investigation of nanoparticle clusters (see Ref. [52] and Chapter 4) and the group of Prof. Dr. Stefan A. Maier from the chair in Hybrid Nanosystems of Ludwig-Maximilians-Universität delivered the particles for the investigations in Ref. [50] and Chapter 5. The particles were produced, washed, and stored in anhydrous ethanol. The details of the nanoparticle synthesis are described in the corresponding chapters. The washing procedure consisted of three consecutive cycles of centrifugation (4000 rpm, 10 min), solvent removal, and redispersion in a fresh solvent. The solvent was removed with a pipette, and redispersion was achieved by bath sonication

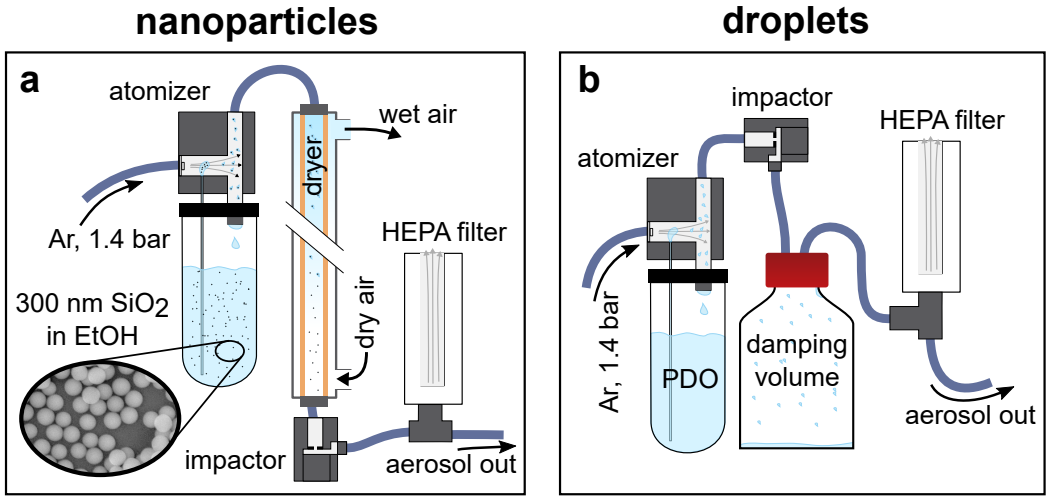

Figure 3.1: Aerosol generation setups for nanoparticles (panel a) and propanediol (PDO) droplets (panel b). **a:** The aerosol source for nanoparticles consisted of a reservoir containing the nanoparticle-alcohol dispersion connected to an atomizer (TSI inc., model 3076) operated with 1.4 bar of argon. The aerosol was dried in a counter-flow membrane dryer (PermaPure MD-700-48S) operated with dry, compressed air. The dried aerosol was passed through an impactor (TSI inc., part no. 1035900). A high-efficiency particulate air (HEPA) filter connected to ambient air ensured a pressure of 1 atm at the aerosol outlet as required by the aerodynamic lens of the reaction nanoscope. **b:** For generating droplet aerosols, the dryer was removed from the system, and a 1 l bottle was inserted between the impactor and the HEPA filter, which acted as a damping volume to stabilize the flow (see atomizer manual) and as a reservoir for excess liquid building up at the impactor over time.

for 5 min. The samples were delivered with concentrations between 20 g of nanoparticles per liter and 40 g/l and diluted to 1 g/l and below for the experiments. When a complete solvent exchange was required, as in Ref. [50], the washing procedure with redispersion in the new solvent was applied.

A note on redispersion by sonication: Sonication is a well-established method for reducing the likelihood of aggregated nanoparticles in the solution [73]. However, in some cases, the sample appeared visually well-dispersed, but still, a cluster contribution (as described in Chapter 4) was observed in the ion spectra, even at low nanoparticle concentrations. To reduce the cluster signal, longer sonication times than 5 min were tested, but no further improvement in the clustering behavior of the samples was observed. A possible explanation is that the bath sonicator was not powerful enough for an ideal de-agglomeration of all particles. For future investigations, the use of a probe sonicator is advisable. Probe sonication can be more effective than bath sonication in reducing the cluster content nanoparticle dispersions [74].

The size distributions of the silica nanoparticles used in our studies were characterized using different methods. The Gallei group provided a polydispersity value of 2.9% for their particles, which they obtained from dynamic light scattering [75] and transmission electron microscopy. The Maier group provided scanning electron microscopy images, from which we determined the size distribution by a combination of algorithms of the OpenCV Python library [76], as shown in Fig. 3.2. A polydispersity of 6% was obtained.

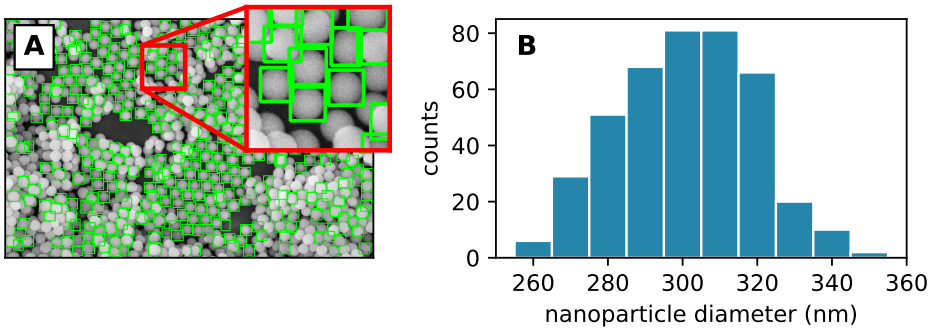

Figure 3.2: Panel A: SEM image of the silica nanoparticles used in Ref. [50]. The green rectangles indicate the position of the particles detected by a combination of algorithms of the OpenCV Python library [76]. Panel B: The histogram of the particle diameters from all marked particles of panel A with a standard deviation of 6% w.r.t the mean of the distribution.

For a typical measurement, between 50 ml and 100 ml of diluted nanoparticle solution was prepared in a flask and attached to the nanoparticle source. As shown in Fig. 3.1a, the nanoparticle solution was aerosolized using an atomizer (TSI inc., model 3076) operated with argon gas at a pressure of 1.4 bar at the inlet. According to the manual and the reference therein [77], the atomizer is designed to produce a fine mist of droplets with a wide size distribution at a constant rate. With nanoparticles present, the goal is that most of these droplets contain exactly one nanoparticle such that only individual particles and

no clusters are contained in the aerosol once the solvent is completely removed in a drying stage.

In the aerosol generation setup used here, the aerosol is dried with a counter-flow membrane dryer (PermaPure MD-700-48S). It consists of two concentric tubes connected by a Nafion membrane, which is permeable to water and alcohols but not to argon, air, or nanoparticles, in particular. The wet aerosol flows on the inside of the membrane, and dry compressed air on the outside in the opposite direction. This configuration causes a humidity gradient across the membrane leading to an outflow of moisture (or alcohol vapor) from the inner tube, and the aerosol gets dried.

After the drying stage, an impactor was used to remove any (large) clusters of nanoparticles that may have formed in the atomizer. The impactor forces the aerosol through a narrow aperture of 0.71 mm toward a stainless steel plate at a distance of 2.0 mm from the aperture. This narrow geometry guides the aerosol around a sharp 90° turn, which causes large particles or clusters with high inertia to hit the steel plate, while (ideally) only single particles are transmitted further.

The last element of the nanoparticle source is a high-efficiency particulate air (HEPA) filter mounted to the transmission line with a T-piece. One outlet of the T-piece connects to ambient air via the HEPA filter, and the other is connected to the inlet of the reaction nanoscope. The purpose of the HEPA filter is to reduce the pressure in the aerosol source to 1 atm, which is required by the aerodynamic lens [78] used for the injection of the nanoparticles into the vacuum.

3.1.2 Droplet aerosol generation

The generation of an aerosol of propanediol droplets was achieved with the setup shown in Fig. 3.1b. For the experiments, only fresh propanediol samples from closed bottles were used. Both propanediol isomers are highly hygroscopic, and prolonged exposure to ambient air would increase the liquid's water content, which might affect the droplet generation and the ion emission, making the experiments non-reproducible. The samples of 1,2-propanediol (Thermo Scientific, +99.5 %) and 1,3-propanediol (Thermo Scientific, 99 %) were purchased from Fisher Scientific. For a typical measurement, about 20 ml of propanediol was filled into the reservoir bottle attached to the atomizer. The 1,3-propanediol was aerosolized using 1.4 bar of argon at the inlet of the atomizer, while for the 1,2-propanediol, 2.0 bar of pressure was required. After leaving the atomizer, the aerosol was size filtered with the same impactor as used for the solid nanoparticles. A bottle with a volume of 1 l was inserted after the impactor. The atomizer manual recommends such a damping volume for a more stable aerosol flow. In addition to its function as a flow instability dampener, the bottle was used as a collection reservoir for propanediol which was building up at the impactor over time. Analogously to the nanoparticle delivery system, the droplet stream was split at the end of the source. One path was attached to the inlet of a HEPA filter connected to ambient air, while the other path led to the aerodynamic lens of the reaction nanoscope. The connection to the ambient air ensured a pressure of 1 atm at the inlet of the aerodynamic lens [78].

3.1.3 Aerodynamic Lens

For the injection of the nanoparticles and the droplets into the vacuum of the reaction nanoscope, an aerodynamic lens was used. The model used in this thesis was designed by H. Bresch at the Freie Universität Berlin [78]. It serves the purpose of generating a collimated stream of nanoparticles. This is achieved by a series of apertures of certain sizes at fixed distances. The pressure on the inlet side of the aerodynamic lens is fixed at 1 atm, and the outlet side is pumped to about 10^{-2} mbar by a roughing pump. Two additional differential pumping stages after the lens exit generate an ultra-high vacuum around the nanoparticle stream, which is required to operate the reaction nanoscope. The dimensions of the aerodynamic lens were crucial for the efficient injection of nanoparticles into the vacuum chamber. For the inlet of the aerodynamic lens, a glass nozzle with a diameter of 190 μm was found to be ideal for injecting 300 nm silica particles. This was tested by measuring the rate of protons generated from nanoparticles for different nozzle sizes. The test data are shown Fig. 3.3. The data demonstrate that optimizing the particle injection system can lead to a manifold increase in the particle or droplet hit rate and should thus not be neglected. This applies not only to the aerodynamic lens's inlet but also to the geometry of the aerodynamic lens itself. Before the lens version by Bresch [78] was installed in the reaction nanoscope at LMU, a different, undocumented aerodynamic lens was used. The change of lenses increased the nanoparticle hit rate by one order of magnitude.

Bresch [78] reports the highest efficiency for a nozzle diameter of 180 μm, which is in reasonable agreement with our results. Due to the dependence of the throughput on the particle size, the inlet and outlet pressure, as well as the length of the injection nozzle, a certain deviation from setup to setup is not surprising.

3.2 Laser systems

Two different femtosecond laser systems were used for the studies presented in this thesis. The laser system for the investigation of clusters of nanoparticles [52] at the AUS was a high-power fiber laser (AFS-UFFL-300-2000-1030-300, Active Fiber Systems GmbH). It produced pulses with a central wavelength of 1030 nm and three different options for the pulse duration (150 fs, 40 fs, and 8 fs). The pulse duration was measured with a second-order autocorrelator. Due to technical problems with the 8 fs output of the laser, the 40 fs option was used for the reaction nanoscopy experiments. The repetition rate of the system could be set to three different values: 50 kHz, 75 kHz, and 150 kHz. While the highest repetition rate of 150 kHz is the best choice for fast data collection and good measurement statistics, it can cause artifacts in the ion time-of-flight spectra since the flight time of heavy ions is typically longer than the period between two laser shots (6.67 μs for a repetition rate of 150 kHz). This means that the heavy ions arrive at the same time at the detector as the light ions from the next laser shot leading to a background signal in the light ion time-of-flight spectra. In the reaction nanoscope at AUS, a spherical mirror with a focal

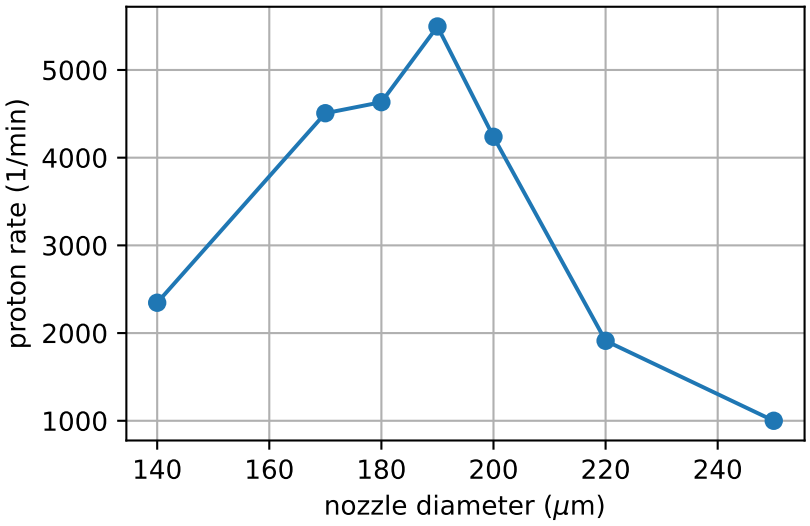

Figure 3.3: Proton detection rate as a function of nozzle diameter for a measurement with 300 nm silica particles ionized by 2 μm pulses. The proton rate was filtered on channeltron signals with a high number of electrons, i.e., nanoparticle hits. The proton rate plotted here is thus proportional to the rate of nanoparticle hits.

length of 100 mm was used to focus the pulses. Measurements were typically carried out at a peak intensity of 5×10^{13} W/cm^2. The intensity was calibrated from a time-of-flight measurement with argon as the target. The ratio between Ar^+ and Ar^{2+} ions was then used to determine the peak intensity [79]. Due to the high output power of the laser system of 150 W, significant attenuation of the laser beam to about 1% of the total power was required not to exceed these intensities. The attenuation was achieved by a half-wave plate in combination with a thin-film polarizer followed by absorptive neutral-density filters.

The laser system used at the LMU was a custom optical-parametric chirped pulse amplifier (OPCPA) [81] producing pulses with a central wavelength of 2 μm at a repetition rate of 100 kHz. Typically, a pulse duration of around 25 fs was achieved. The pulses were characterized by frequency-resolved optical gating (FROG) [82, 83] using the third harmonic as the nonlinear signal. A typical pulse measurement is shown in Fig. 3.4. For the reconstruction of the FROG traces, the COPRA pulse reconstruction algorithm [80] with a slightly modified version of its reference implementation [84] was used. The maximum output power of the laser system at LMU was 6 W. After attenuation, typically about a third of the power was focused by a spherical silver mirror with a focal length of 75 mm, reaching a peak intensity of about 5×10^{13} W/cm^2. To the best of our knowledge, for strong few-cycle pulses at 2 μm, there are no published methods yet, which allow an intensity calibration based on relative ion yields similar to the Ar^+/Ar^{2+} method used above. The laser intensity for the OPCPA system was therefore calibrated from the geometry of the laser focus and the measured pulse duration. Due to the uncertainties of both measurements, a relative intensity error of about 50% is expected.

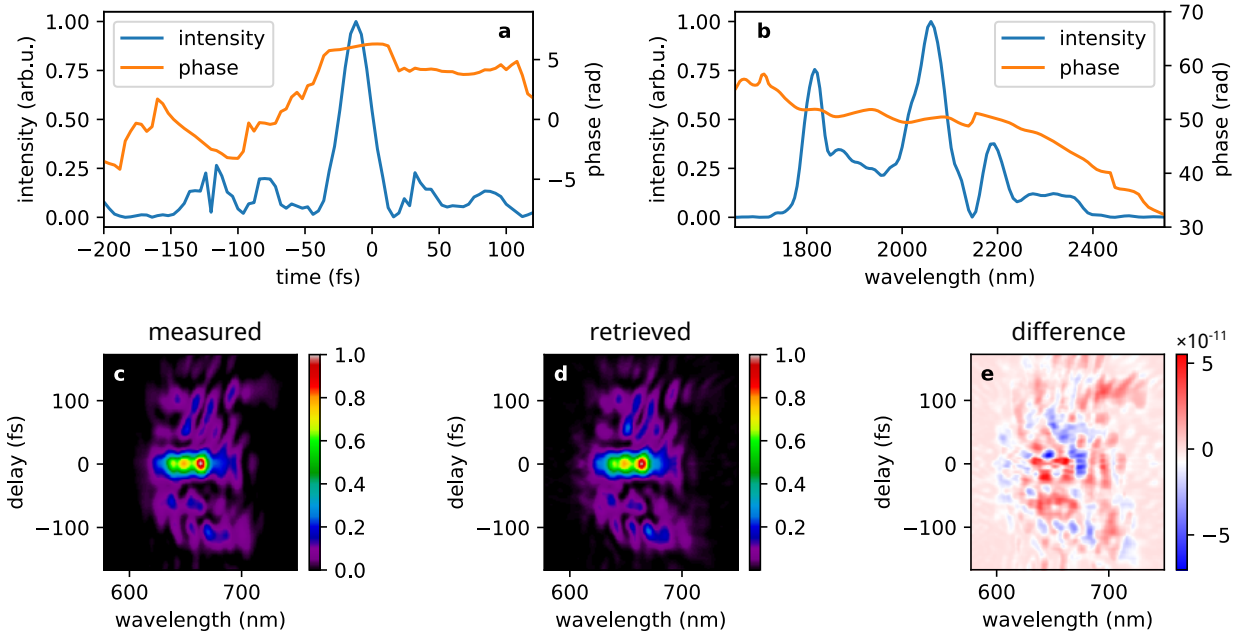

Figure 3.4: OPCPA pulse characterization using a third-harmonic FROG. **a:** Retrieved pulse in the temporal domain. The full width at half maximum of the main peak is 24 fs. **b:** Retrieved pulse in the spectral domain. **c:** Measured third-harmonic FROG spectrogram. **d:** Retrieved FROG spectrogram using the *common pulse retrieval algorithm* (COPRA) [80]. **e:** Difference between the measured and the retrieved spectrograms.

3.3 Reaction nanoscope

The reaction nanoscope is depicted in Fig. 3.5. It allows the measurement of the three-dimensional momenta of laser-generated ions from the surface of nanoparticles or droplets using the ion detection side of a reaction *microscope* [85] in combination with a channeltron electron multiplier for categorizing the events into gas-phase ionization events and nanoparticle/droplet ionization events.

3.3.1 Detection of nanoparticle or droplet events

Even though the exit of the aerodynamic lens is differentially pumped to reduce the amount of carrier gas in the interaction region, the contribution of ions generated from the ionization of single, gas-phase molecules to the reaction nanoscopy spectra can still be significant. In order to reduce the gas-phase contribution, the amount of detected electrons is to classify an ion's origin as a single molecule or nanoparticle/droplet. Since the strong-field ionization of a nanosystem generates many more electrons than the ionization of an atom or a small molecule [71], ions detected in coincidence with a small (or zero) electron signal are associated with the ionization of a single molecule and ions detected with a large electron signal correspond to nanoparticle/droplet hits. The threshold can be determined from gas-only experiments. An example of the separation into the gas-phase background and

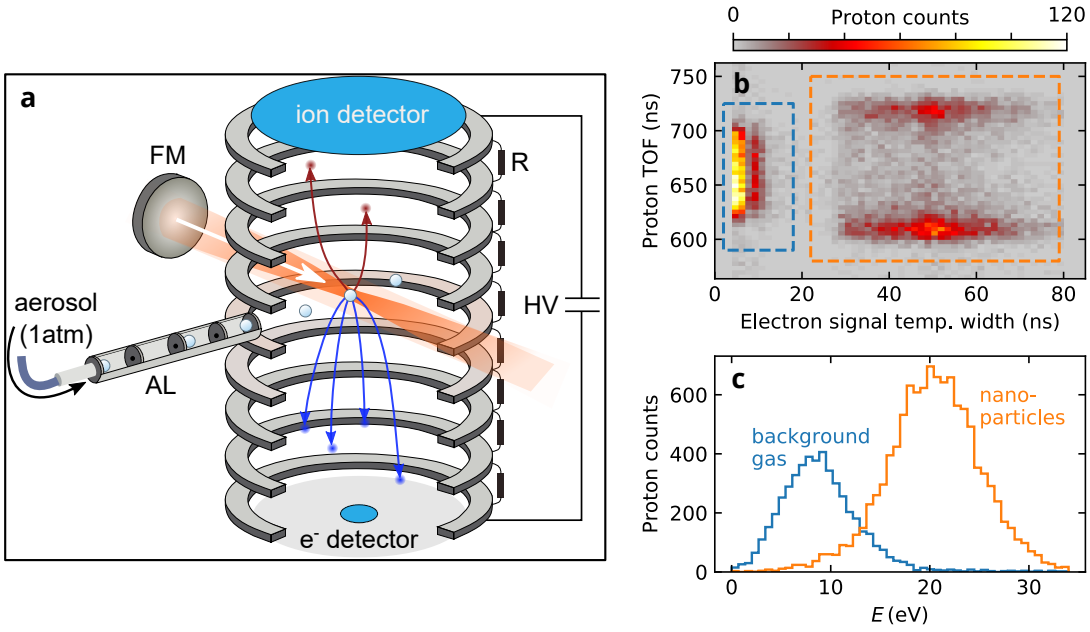

Figure 3.5: Reaction nanoscope and coincident electron detection. **a:** Setup of the nanoscope. The aerosol is injected through the aerodynamic lens (AL). The particles or droplets are ionized in the focus of the laser (FM: focusing mirror). An electric field generated by a high-voltage (HV) across the spectrometer forces the generated electrons and ions onto the corresponding detectors. The spectrometer rings are spaced equidistantly and separated by 100 kΩ resistors (R), ensuring a constant electric field [71]. The ion detector measures the time-of-flight and the position of the emitted ions. The signal of the electron detector is time-integrated and used as a measure for the number of generated electrons. **b:** Histogram of proton counts as a function of the electron signal and the time-of-flight. The time-of-flight axis is restricted to the proton arrival time. The detected ions can be grouped into ions emitted from background gas (blue dashed rectangle) and from nanoparticles (orange dashed rectangle). **c:** The energy of histograms of the protons from panel b. Due to the coincident electron detection, the ion origin in the energy overlap region (approx. 10 eV to 20 eV) can be determined.

the nanoparticle signal for the case of protons is shown in Fig. 3.5b. In Fig. 3.5c the most important advantage of the classification by electron signal is illustrated. As shown, the energy spectra of protons from the background and from nanoparticles have a significant overlap. Individual ions within the overlap region can only be assigned to either of the two categories due to the single-shot coincident detection of the electron signal. Of course, the same is true for potentially overlapping ion momentum spectra.

The data shown in Fig. 3.5b,c are representative of reaction nanoscopy experiments with nanoparticles. When droplets are injected into the vacuum chamber, however, molecules continuously evaporate from their surface. This leads to a higher density of single molecules around a droplet in the interaction region than for nanoparticles. This halo of molecules makes the ionization of a single molecule in coincidence with the ionization of a droplet more likely. As a consequence, large electron signals in droplet experiments often correspond to both the ionization of a droplet and, at the same time, a single molecule. Note that the inverse statement is not true. A small electron still corresponds to the ionization of *only* a single molecule. To mitigate this effect of "false coincidences," the droplet data can be further cleaned up by applying a filter based on the ion arrival position on the detector. This is illustrated in Fig. 3.6. Note that this filtering procedure can only be applied if the laser polarization is chosen perpendicularly to the time-of-flight axis. Only in this case, droplet ions are predominantly detected at large deflections from the center of the detector, making them separable from gas-phase ions at small deflections (see Fig. 3.6b).

As a technical note: The "electron signal" for the reaction nanoscope at the AUS was measured as the signal width of the decoupled channeltron voltage over a fixed threshold. For the data collected at the LMU, "electron signal" refers to the decoupled, digitally sampled, and time-integrated channeltron voltage signal.

Probability for multiple nanoparticle hits

A large magnitude of the electron signal in reaction nanoscopy experiments is, strictly speaking, an indication that *at least one* nanoparticle or droplet was ionized by the laser. This implies a non-zero probability of ionizing more than one nanoparticle per laser shot. In this section, we relate the average rate of large electron signals γ to the probability that exactly one nanoparticle was ionized, given that a large electron signal was detected. This can be written as the conditional probability $P(n = 1|n \geq 1)$, where n denotes the number of ionized particles or droplets. With a typical experimental rate of one large electron signal for every 100 laser shots, we obtain $\gamma = 0.01$. This rate is equal to the probability $P(n \geq 1)$ of ionizing at least one particle per laser shot: $P(n \geq 1) = \gamma = 0.01$.

Assuming independent particles (which is the case for low particle densities in the aerosol stream), and a constant flow rate of nanoparticles, the probability $P(n)$ for detecting exactly n particles follows a Poisson distribution:

$$P(n) = \frac{\lambda^n}{n!} e^{-\lambda}, \tag{3.1}$$

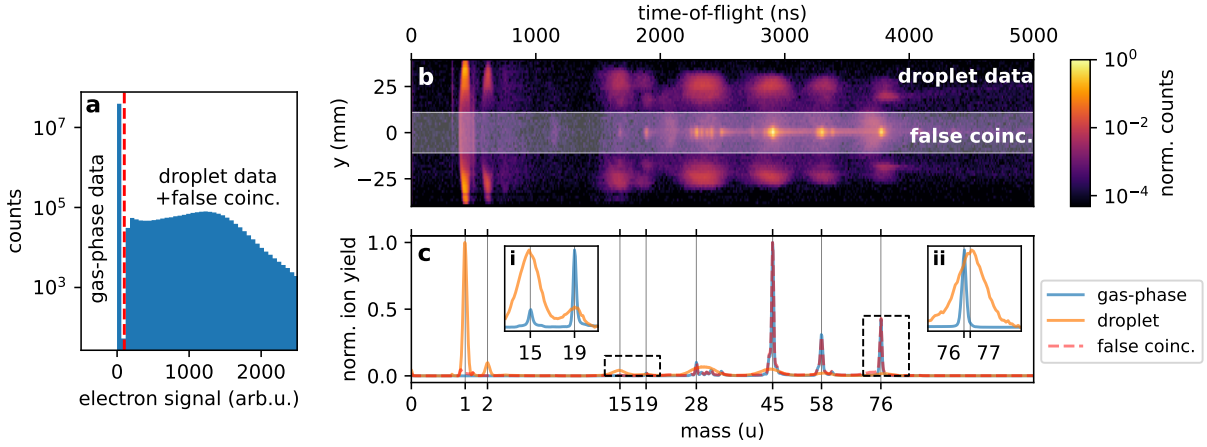

Figure 3.6: Reduction of false coincidences in droplet experiments. **a:** Histogram of electron signal values for a measurement with 1,2-propanediol droplets. The dashed red line indicates the threshold below which ions detected in coincidence originate from a single gas-phase molecule. Ions detected with electron signals above the threshold stem from either the surface of a droplet or a single molecule. The latter case defines a false coincidence (false coinc.). **b:** Time-of-flight histogram, position-resolved along the polarization direction of the laser (y) and filtered on events with a large electron signal ("droplet data + false coinc." of panel a). The white shaded area indicates detector positions with a low deflection from the center of the detector, corresponding to ions from gas-phase molecules and thus false coincidences. **c:** Comparison between the time-of-flight histogram obtained for small electron signals (gas-phase data of panel a) and the projection of the counts inside (false coinc.) and outside (droplet) the white-shaded area of panel b. The similarity between the histograms of gas-phase and false coincidences confirms that ions detected at low deflection correspond to gas-phase molecules. The insets i and ii show the data in the dashed boxes in more detail. The x-axes of panels b and c are identical (both are linear in time-of-flight). The mass values in panel c were obtained from a calibration as described in the text.

where λ is the mean of the distribution. Consequently, we obtain for $P(n \geq 1)$:

$$P(n \geq 1) = 1 - P(0) = 1 - e^{-\lambda}. \tag{3.2}$$

With $P(n \geq 1) = \gamma$, the mean of the Poisson distribution can be expressed in terms of the hit rate:

$$\lambda = -\ln(1-\gamma) \underbrace{\approx}_{\gamma \ll 1} \gamma \tag{3.3}$$

Using this relationship, the conditional probability for exactly one particle being ionized given a large channeltron signal $P(n = 1|n \geq 1)$ can be derived. It is defined as:

$$P(n = 1|n \geq 1) = \frac{P(n = 1 \cap n \geq 1)}{P(n \geq 1)} = \frac{P(n = 1)}{P(n \geq 1)}. \tag{3.4}$$

Inserting the Poisson distribution, one obtains:

$$P(n = 1|n \geq 1) = \frac{P(n = 1)}{P(n \geq 1)} = \frac{\lambda e^{-\lambda}}{1 - e^{-\lambda}} \approx 1 - \frac{\lambda}{2} \approx 1 - \frac{\gamma}{2}. \tag{3.5}$$

Here, the first approximation was obtained from a Taylor expansion up to the first order for small λ and the second approximation uses Eq. (3.3). In the case of a channeltron rate of $\gamma = 0.01$, the probability of *exactly* one nanoparticle being ionized, given that a large channeltron signal was detected, is approximately $P(n = 1|n \geq 1) = 99.5\%$.

The probability of multiple particles being ionized at once is consequently given by:

$$P_{\text{multi}} \equiv P(n > 1|n \geq 1) = 1 - P(n = 1|n \geq 1) = 1 - \frac{\lambda e^{-\lambda}}{1 - e^{-\lambda}} \approx \frac{\gamma}{2} \tag{3.6}$$

This multihit probability is shown in Fig. 3.7 for the full range of channeltron hit rates: $0 \leq \gamma < 1$.

3.3.2 Typical nanoparticle density in the laser focus

From the average channeltron rate and the focal geometry, the nanoparticle density in the aerosol stream can be estimated. On the time scale of the duration of a laser pulse (25 fs in our case), the nanoparticles in the focus do not move significantly. Assuming a particle velocity of 200 m/s (below the speed of sound [86]), the distance traveled is only 5 pm (less than the size of an atom) within a single laser pulse. Therefore, the particle motion during ionization can safely be neglected[1]. In the interaction region of the nanoscope, the full width at half of the intensity maximum of the laser focus in the plane perpendicular to the propagation direction was approximately FWHM = 50 μm (measured with a camera). This corresponds to a beam waist $w_0 = \text{FWHM}/\sqrt{2\ln 2} = 42\,\mu\text{m}$ and a Rayleigh-length of

[1] At a repetition rate of 100 kHz, the time between two laser pulses is 10 μs, which corresponds to a distance of 2 mm. This is larger than the size of the laser focus, meaning that the same particle cannot be exposed to two consecutive laser pulses.

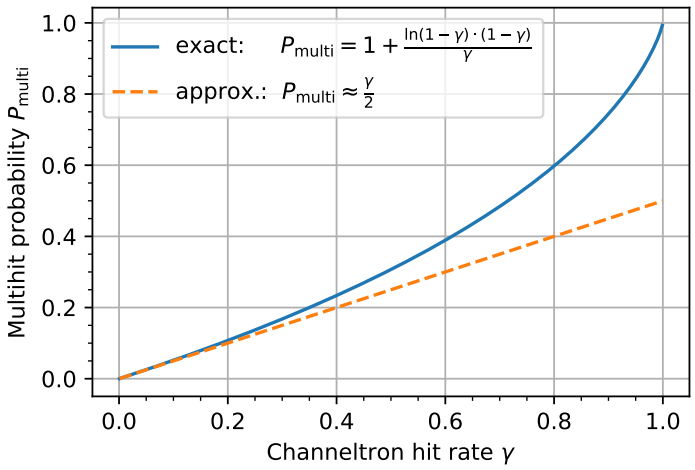

Figure 3.7: Probability of ionizing more than a single nanoparticle given a channeltron hit P_{multi}, defined in Eq. (3.6), as a function of the channeltron hit rate γ. The solid curve shows the exact expression $P_{\text{multi}} = 1 - \frac{\lambda e^{-\lambda}}{1-e^{-\lambda}}$ with $\lambda = -\ln(1-\gamma)$. The dashed line shows the approximation for $\gamma \ll 1$: $P_{\text{multi}} \approx \gamma/2$.

$z_R = \pi w_0^2/\lambda = 2.8\,\text{mm}$. Since the Rayleigh range is longer than the width of the collimated aerosol stream of approximately 1 mm, we will assume that nanoparticles are ionized in a volume of $V = 42\,\mu\text{m} \times 42\,\mu\text{m} \times 1\,\text{mm}$. As mentioned in the section above, the channeltron hit rate γ for large electron signals and thus the average number of particles $\langle N \rangle /$ within this volume is about $\gamma = 10^{-2}$. Hence, the density ρ of the nanoparticles in the focus is estimated as

$$\rho = \langle N \rangle / V \approx 10^4 / \text{cm}^3. \tag{3.7}$$

We expect about a factor of two uncertainty per linear dimension in the determination of the ionization volume, which makes the density estimate accurate within about one order of magnitude. The estimated value of $\rho = 10^4/\,\text{cm}^3$ is two orders of magnitude below what is reported for the aerosol density that the atomizer produces [87]. Considering the estimated error, the density in the interaction volume is still at least one order magnitude lower than what is expected at the atomizer exit.

For the propanediol droplet experiments, this is not surprising since a significant quantity of propanediol accumulated at the impactor and inside the damping bottle over the course of a measurement. This means that a certain fraction of droplets was stopped at the impactor and removed from the aerosol, lowering the density.

For the case of the silica nanoparticles, the explanation for the low target density in the laser focus is the following. When the nanoparticles are aerosolized from a solution, solvent droplets with ideally one nanoparticle per droplet are produced. However, since the distribution of the nanoparticles in solution is probabilistic, the number of nanoparticles per droplet at the atomizer output is as well. The sample concentration needs to be sufficiently low to minimize the number of droplets with more than one nanoparticle (to avoid cluster formation, see Chapter 4). Typical concentrations in nanoparticle experiments were on

the order of 10^{10} particles per cubic centimeter of solution (for particles with a diameter of 300 nm, this corresponds to a mass concentration of about 0.37 g/l). With a typical droplet diameter at the aerosol outlet of 1 μm [88] or a corresponding droplet volume of approximately $5 \times 10^{-13}\,\mathrm{cm}^3$, it is thus expected that a single droplet contains 5×10^{-3} particles. The aerosol density of the atomizer on the order of $10^6/\,\mathrm{cm}^3$ [87] needs to be multiplied with this probability for a droplet containing a particle. Doing so results in an expected particle density in the interaction region which is consistent with the estimate of Eq. (3.7): $\rho \approx 10^4/\,\mathrm{cm}^3$.

3.3.3 Ion momentum measurement

The ion detector of both reaction nanoscopes consisted of a chevron stack of microchannel plates (MCP) and a delay-line anode (DLD 80, Roentdek Handels GmbH). It allowed the measurement of the ion time-of-flight (TOF) and the arrival position on the detector. For individual ions, the time-of-flight was determined from the arrival time of a decoupled (high frequency) voltage spike from either the front side or the back side of the MCP[2]. This voltage spike was amplified using an Ortec FTA820A amplifier and then sent into a constant-fraction discriminator (CFD, Ortec 935) to increase the time resolution. The timing of the resulting voltage pulse was finally detected using a time-to-digital converter (TDC8HP, Roentdek Handels GmbH). The position detection relied on four additional voltage pulses per ion, two per direction (x and y) of the delay-line anode. Every direction of the DLD consisted of a pair of wound-up wires. At either end of the wire pair, the (high-frequency part of the) voltage across the pair was decoupled, leading to two signals per direction. The DLD voltage pulses were pre-processed by the same combination of amplifiers and CFDs before their timing was recorded in the TDC8HP. The position along a coordinate, x or y, is proportional to the timing difference of the voltage pulses decoupled from either end of the corresponding pair of delay line wires. The conversion from timing difference to position, as well as the rest of the data acquisition, was achieved using the CoboldPC software (Roentdek Handels GmbH).

From the TOF and position of an ion, its momentum vector at the time of birth can be reconstructed. The reconstruction relies on the constant electric field E inside the nanoscope and is based on classical trajectories. The direction of the electric field is along the time-of-direction z, and the other directions are field free, leading to the following trajectory equations

$$x(t) = \frac{p_x}{m}t, \tag{3.8}$$

$$y(t) = \frac{p_y}{m}t, \tag{3.9}$$

$$z(t) = \frac{1}{2}at^2 + \frac{p_z}{m}t = L, \tag{3.10}$$

[2]The unused output port should always be terminated with a 50 Ω resistor to avoid signal artifacts. If the connector for the MCP front is used for the time-of-flight, the MCP back should be terminated and vice-versa.

where t is the TOF, m is the ion mass, L is the distance between the interaction region and the ion detector, and $a = Eq/m$ is the acceleration due to the electric field E for an ion with charge q. The initial momenta p_i can be reconstructed from the TOF t and an ion's arrival position at the detector $(x(t), y(t))$:

$$p_x = m\frac{x}{t}, \tag{3.11}$$

$$p_y = m\frac{y}{t}, \tag{3.12}$$

$$p_z = m\frac{L}{t} - \frac{1}{2}m \cdot a \cdot t. \tag{3.13}$$

The ratio m/q can be obtained from the TOF after a calibration of the spectrometer. This is achieved with ions of very low energy, i.e., sharp peaks in the time-of-flight histogram. Such ions are generated, for example, after the single ionization of single molecules. In that case, the only momentum imparted on the ion is the recoil momentum from the released electron (and negligible contribution due to the momenta of the absorbed photons) [89, 90]. Thus, setting $p_z = 0$ in Eq. (3.13), it follows that the TOF is proportional to the square root of the ratio m/q.

$$t \propto \sqrt{\frac{m}{q}}. \tag{3.14}$$

In practice, the TOF t is only measured up to an initially unknown offset with respect to the actual instance of ionization. This offset and the proportionality constant of the above equation can be fixed by fitting a linear function using the time of flight for $p_z = 0$ for multiple ions with known m/q. The TOF calibration can be used to eliminate the electric field from the momentum calculations such that only the length L of spectrometer's ion side needs to be known. If $p_z = 0$, it follows that:

$$a = \frac{Eq}{m} = \frac{2L}{\tau_{m/q}^2}, \tag{3.15}$$

where $\tau_{m/q}$ was used as a notation the fragment- or m/q-specific TOF for $p_z = 0$. Inserting this expression back into Eq. (3.13), we obtain:

$$p_z = \frac{mL}{t}\left(1 - \frac{t^2}{\tau_{m/q}^2}\right). \tag{3.16}$$

This approach is advantageous over the direct calculation of p_z since the value of the electric field is removed as a potential source of error and the length of the spectrometer can be measured with high accuracy. For this reason, Eq. (3.16) was used throughout this thesis for calculating the momentum component parallel to the TOF axis.

Limitations of the ion detector

A delay-line detector, as used in the reaction nanoscope, is optimized for detecting only a few ions (< 10) per laser shot. However, we found that staying within this limit in reaction nanoscopy experiments is not always possible. The reason is the high number of molecular adsorbates on the surface of a nanoparticle, which can contribute one or more ions to the emitted ion spectrum upon ionization of the nanoparticle surface. The number of adsorbates can be estimated using the density of silanol (Si-OH) groups on the silica surface. In Chapter 5, it is shown that silanol groups are the primary source of protons in reaction nanoscopy experiments with silica particles and that protons dominate the overall ion spectra. With a surface density of approximately $2.2\,\mathrm{OH/nm^2}$ [91], a $d = 300\,\mathrm{nm}$ silica particle with a surface area of approximately $3\times10^5\,\mathrm{nm^2}$ contains about 600k silanol groups, which could release a proton. To stay within the ideal operating range of the ion detector (< 10 ions), the average proton generation probability from silanol groups thus has to be on the order of 10^{-5}. This probability alone would not be a problem since the laser power can be arbitrarily lowered. The challenge in current reaction nanoscopy experiments is the strongly nonlinear dependence of the ion generation probability on the laser intensity (I^N, with $N > 10$, see Chapter 2). This means that a small increase in laser intensity already causes the proton generation probability to exceed the threshold of 10^{-5}, and a small decrease significantly lowers the rate at which protons are generated and thus substantially increases the measurement time. A second problem at low intensities arises from the increased contribution of ions emitted from nanoparticle clusters, an effect demonstrated in Chapter 4. These considerations show that, in practice, it is often unavoidable to generate more protons from a nanoparticle or droplet surface than the detector is optimized for, leading to detector saturation. The following section discusses the effects of detector saturation. The term "laser intensity" will refer to a constant intensity at a certain point in the laser focus (without taking into account focal volume averaging).

For laser intensities, which produce proton counts slightly above the detector limit, the effect of the detector dead-time can be observed in the proton histograms. The delay-line detector used in the reaction nanoscope has a multihit dead-time of 10 ns-20 ns (see Ref. [92]). For ion detection in single-molecule experiments, this dead time is usually sufficient for detecting multiple ion fragments per laser shot. If the fragments differ in m/q, their times-of-flight are typically significantly different, easily avoiding dead time limitations. For ion fragments of identical m/q, their mutual Coulomb repulsion causes different emission directions from the interaction region and, for the most part, sufficiently different times-of-flight above the dead-time limit. In the experiments on nanoparticles or droplets presented here, most emitted ions are protons, and the Coulomb repulsion determines their emission direction from the charged nanoparticle surface instead of each other. As a result, the times-of-flight of multiple protons can be dead-time-limited, which leads to asymmetric time-of-flight and momentum histograms since protons with longer time-of-flight values are less likely to be detected. This effect is shown in Fig. 3.8 for an exemplary data set obtained from an experiment with silica nanoparticles. This dead-time effect is most severely observed for protons. Other fragments like H_2^+ or CH_3^+ are produced

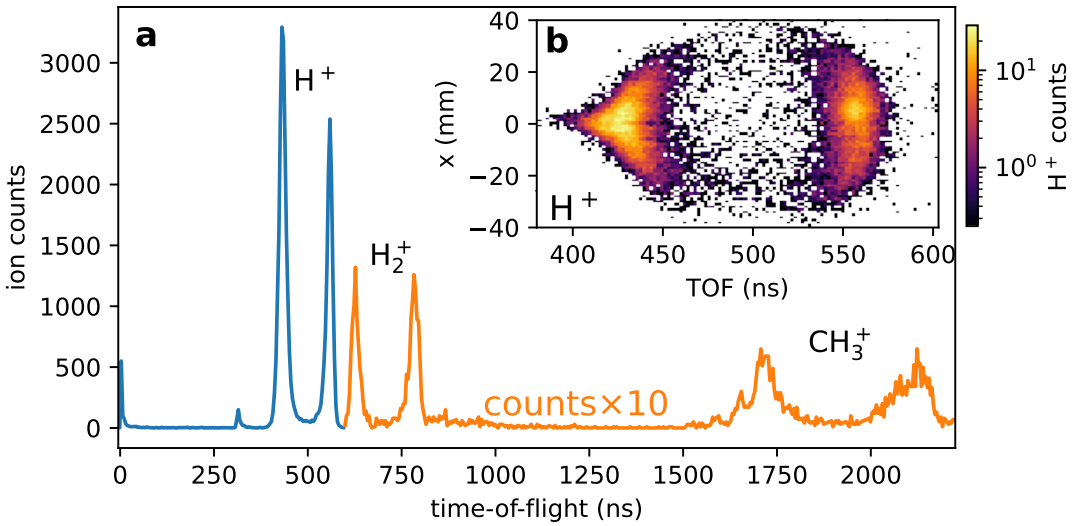

Figure 3.8: Asymmetric proton spectra. **a:** Ion time-of-flight spectrum for a measurement with silica nanoparticles filtered on large electron signals, i.e. nanoparticle hits. An asymmetry along the time-of-flight direction can be observed mostly for the protons, while the H_2^+ and CH_3^+ spectra are approximately symmetric. **b:** Proton (H^+) time-of-flight spectrum, position-resolved along the laser propagation direction. For this measurement, the laser polarization was chosen along the time-of-flight axis.

at much lower rates, which makes the detection of two ions of the same species in a single laser shot less likely.

A more detrimental saturation effect can be observed at higher intensities. In this regime, the decoupled signal from the MCP can reach 10s of volts (see Fig. 3.9a). For comparison, typical amplitudes for single ion MCP signals are on the order of 10s of millivolts. The enormous voltage difference suggests that such intense shots correspond to a *very* high number of generated ions (on the order of 1000 ions if a linear scaling is assumed). From the arrival time of the peak in Fig. 3.9a, it can be deduced that the ion species causing the extremely strong signal are protons. This is qualitatively consistent with the above considerations about the proton generation. That the signal is related to a high intensity can be deduced from an estimate of the proton energy from the voltage trace. As shown in Fig. 3.9a, protons with energies of approx. 75 eV are generated with such signals, which is 2-3 times more energy than in the regime below detector saturation. According to our understanding, the increased ion energy requires more surface charge on the nanoparticle, which makes a higher laser intensity necessary [42]. The strong voltage signals from the MCP cause a saturation of the signal amplifier used before the CFD. As shown in Fig. 3.9b, the saturation results in a ringing at the amplifier output, which lasts more than 1 μs. This ringing can be observed as unphysical spikes in the "raw" time-of-flight spectra of the CoboldPC software. "Raw" time-of-flight spectra consider all TDC counts on the channel connected to the MCP, even those without a valid position reconstruction. Apart from the ringing at the amplifier output, strong proton signals as in Fig. 3.9a appear to increase the dead-time of the MCP itself since no other peaks in the

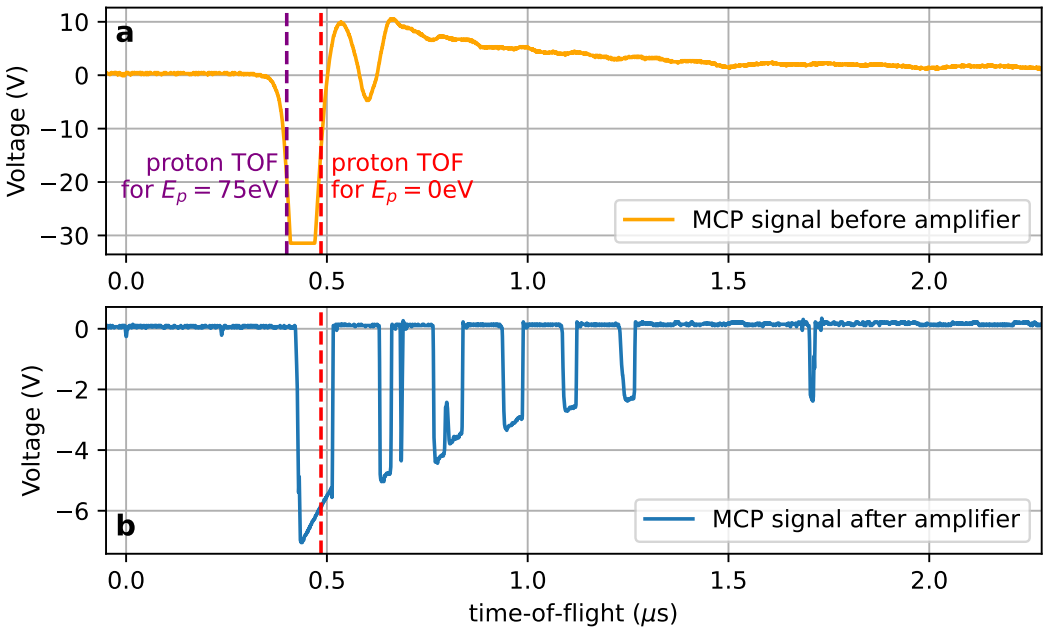

Figure 3.9: Extreme example for the single-shot detector response for a nanoparticle measurement at high laser intensity (recorded with an oscilloscope). **a:** Decoupled signal from the MCP *without* further amplification. The arrival time of the main peak corresponds to the proton time-of-flight (TOF), as indicated by the dashed lines. A voltage pulse produced from a single ion causes signal amplitudes on the order of 10 mV, while here, 10s of volts are observed. The actual amplitude for the signal shown here is unknown due to the saturation of the oscilloscope channel at ≈ -30 V. **b:** Exemplary amplifier output for a similar input as shown in panel a. A nonlinear amplifier response and strong ringing with a decay time of more than 1 μs are observed.

voltage curve can be observed, even after many microseconds (not shown in the figure). Therefore, we assume that the acquisition software can detect not a single ion with a valid position for such a laser shot.

The effect of these two types of detector saturation on the nanoparticle data is expected to be equivalent to a filter on low local intensity in the focal volume. Low-intensity regions are unaffected by detector saturation, while areas of high intensity might be. Hence, some care must be taken when interpreting reaction nanoscopy data. Since a single measurement might not represent the entire focal volume, it is advisable to perform experiments for a range of pulse energies and test whether parameters such as the ion energy change upon a change of pulse energy. Additionally, we recommend monitoring the rate of exceedingly strong MCP signals on an oscilloscope (as shown in Fig. 3.9). This rate can be compared to the rate of large channeltron signals, i.e., the rate of nanoparticles hits. The ratio of both rates indicates which fraction of nanoparticle hits generate entirely undetectable signals, like in Fig. 3.9. This fraction should obviously be kept as low as possible by decreasing the laser intensity to the lowest possible value while maintaining a workable data acquisition rate. Suppose the fraction of undetectable MCP signals is negligible. In that case, the only other saturation effect is due to the detector dead time, which is insignificant for ions

heavier than the proton (as shown in Fig. 3.8). We, therefore, expect that this effect does not significantly affect the interpretation of reaction nanoscopy data

Due to the nonlinear scaling of the ion generation rate, detector saturation is not always avoidable in strong-field reaction nanoscopy experiments. However, since the nonlinearity of the signal causes the problem, future reaction nanoscopy could benefit from using higher energy photons, say close to the ultra-violet region. This would greatly reduce the nonlinearity of the ionization and ion generation process and would thus enable investigations over a wider range of laser intensities.

Chapter 4

Reaction nanoscopy with nanoparticle clusters

In this chapter, the signatures of nanoparticle clusters in the proton momentum spectra are investigated both theoretically, using the model introduced in Chapter 2, and experimentally, using the reaction nanoscopy technique. We demonstrate that cluster- and nanoparticle-emitted ions can be identified in a single-shot manner due to their negligible overlap in certain projections of the momentum histograms and the coincidence spectra. We furthermore discuss the intensity dependence of both signals and find a dominance of ions emitted from nanoparticle clusters at low laser intensities, which provides a possible explanation for previously observed discrepancies between theoretical predictions and experimental data in studies on strong-field electron emission from nanoparticles.

The majority of the results presented in this section were published in Ref. [52], the first study on reaction nanoscopy from isolated clusters of nanoparticles.

4.1 Introduction

When nanoparticles come close to each other and form a cluster, the plasmonic, excitonic, and magnetic responses of the individual nanoparticles start coupling, which gives rise to a cluster response that differs from the sum of the individual responses [93, 94]. These coupling effects, in combination with the very high surface-to-volume ratio of nanoparticle clusters, have led to a multitude of applications. Nanoparticle clusters are used, for instance, in surface-enhanced Raman scattering [95], for optical labeling [96], in photocatalysis [97–103], for chemical separation, and enrichment [104, 105], and in biomedical applications [106–108].

Nanoparticle clusters can be produced in a bottom-up fashion, starting from a stable, i.e., non-aggregated, dispersion of single nanoparticles in a suitable solvent. Particle stability is achieved through various approaches depending crucially on the nanoparticle surface. A common stabilization approach is modifying the nanoparticles' surface charge such that their mutual Coulombic repulsion overcomes all attractive forces. The effective charge of a

particle in solution is usually measured via the zeta potential ζ, the electrostatic potential at the slipping interface between the liquid and the nanoparticle [109]. The higher the magnitude of the zeta potential, the higher the charge on the particle surface, the more repulsion between the particles, and thus the more stable the solution. Due to the finite temperature of the particle solution and the kinetic energy of the particles, the absolute value of the zeta potential must be sufficiently large to maintain stability. At room temperature, zeta potentials of $|\zeta| > 30\,\mathrm{mV}$ are considered stable [110]. The silanol groups on the surface of silica particles, for example, get deprotonated when the particles are dispersed in pure water [111, 112], which gives rise to a negatively charged particle surface and thus negative zeta potential stabilizing the particles.

Cluster formation from a stable dispersion can be initiated by destabilizing the nanoparticles in a controlled way. There are two main approaches to destabilization: Internal destabilization by the modification of the nanoparticle-nanoparticle interaction and the application of external forces [94]. One way of internally destabilizing an aqueous solution of silica nanoparticles is by changing the pH to counteract the deprotonation [113], thus lowering the surface charge and the inter-particle repulsion. The second way of internal destabilization is the addition of salts. Salt ions attach to the charged nanoparticle surfaces and form an electric double layer, which (partially) shields the electrostatic inter-particle repulsion [114]. The salt concentration above which a nanoparticle dispersion becomes unstable is called the critical salt concentration [115]. Finally, cluster formation can be internally controlled by surface functionalization. As before, this can effectively imply the control of the surface charge when, for instance, parts of the ligands are prone to (de-) protonation in solution. Apart from charge interactions between the ligands of different particles, steric and osmotic, as well as solvophilic or solvophobic interactions, can be used to form nanoparticle clusters [94].

For the results presented in this chapter, we started from a stable dispersion of silica nanoparticles ($d = 300\,\mathrm{nm}$) in a mixture of ethanol and water, and achieved the formation of nanoparticle clusters by an external force. The aerosol generator introduced in Section 3.1 first produced an aerosol of small droplets of nanoparticle dispersion. In the second step, the solvent was dried off such that only the nanoparticles remained. If a droplet contained more than one nanoparticle, the surface tension of the drying, i.e., shrinking, droplet forced the enclosed particles closer and closer together, resulting in the formation of a nanoparticle cluster.

The strong-field emitted ions emitted from the mixed stream of single particles and clusters were analyzed using the reaction nanoscopy technique. The technique's sensitivity to the optical near-field around the nanostructures allowed an in-situ identification of the origin of the emitted ions (single particle or cluster) on a single-shot basis. Using the model introduced in Chapter 2, we found that the optical near-field governs the ion emission (see Fig. 4.1) and that the nonlinearity of the strong-field ion generation causes a pseudo-alignment of small nanoparticle clusters like dimers. Further results on the intensity dependence of the cluster contribution suggested a high relevance of our findings on related work on strong-field electron emission.

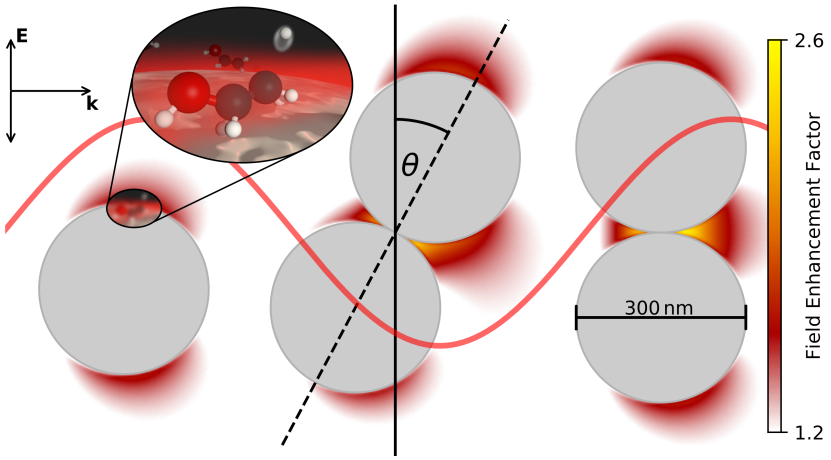

Figure 4.1: Near-field enhancement around a 300 nm silica nanosphere and its dimers for a linearly polarized laser pulse (red line) with a central wavelength of 1030 nm. The laser polarization (**E**) and propagation (**k**) directions are shown in the top left. The local field enhancement factor was calculated by FDTD simulations and is encoded by the color scale. The angle θ is defined as the angle between the dimer axis and the laser polarization axis. The laser-induced deprotonation of molecules from the nanoparticle surface is shown in the inset. Figure taken from Ref. [52].

4.2 Experimental Techniques

For a detailed description of the experimental techniques, see Chapter 3. In brief, we used a commercial fiber laser system with a central wavelength of 1030 nm, a repetition rate of 150 kHz, and a pulse duration of 40 fs. The laser pulses were attenuated and then back-focused by a spherical silver mirror (f = 100mm). In the laser focus, i.e., the interaction region of the reaction nanoscope, intensities of up to 5×10^{13} W/cm^2 were reached. A mixed aerosol of single nanoparticles and clusters was generated from dispersions of d =300 nm silica nanoparticles using argon as the carrier gas. The particles were prepared in ethanol at a concentration of 25 g/l and diluted with deionized water. The cluster content in the aerosol was controlled by varying the concentration of the nanoparticle dispersion between 0.2 g/l and 1.5 g/l. The aerosol was injected into the reaction nanoscope with an aerodynamic lens to form a collimated stream of nanoparticles intersecting the laser beam in the focus. Due to the transmission characteristics of the aerodynamic lens [78] and the aerosol source as a whole (see discussion in Section 3.1), it is assumed that the ion signal from nanoparticle clusters is mostly generated by the ionization of nanoparticle dimers with a negligible contribution of larger clusters.

4.3 Proton Emission from single nanoparticles and nanoparticle clusters

We studied the influence of nanoparticle clusters on the measured proton momentum distribution by carrying out measurements for different concentrations of nanoparticles in the

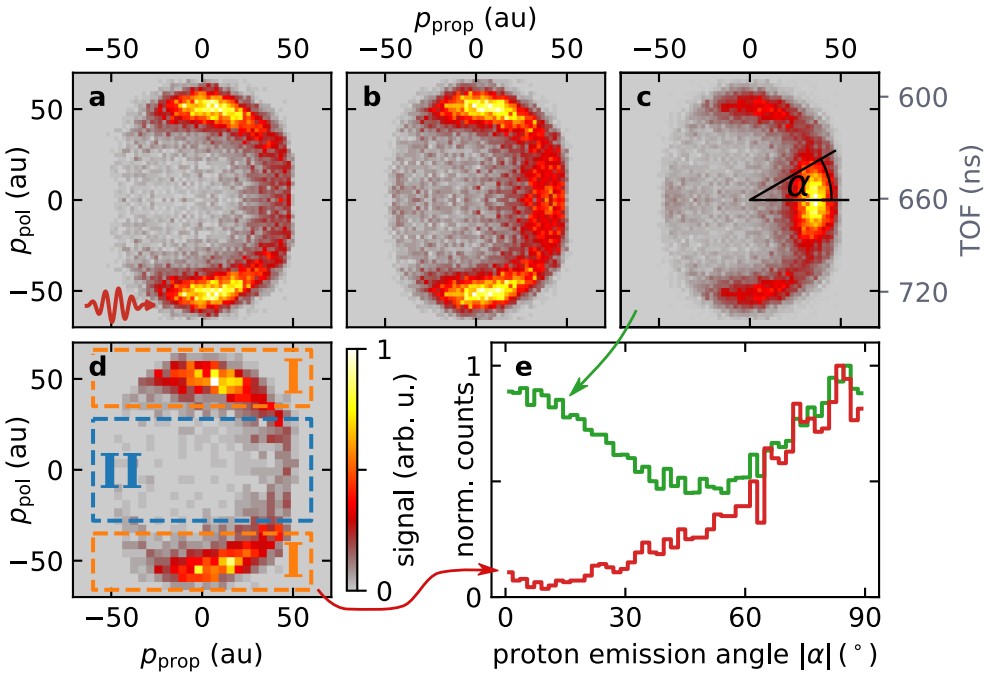

Figure 4.2: Measured proton momentum distributions for different sample concentrations. **a:** 0.2 g/l. **b:** 0.4 g/l. **c:** 1.5 g/l. Momenta are shown in atomic units (au). The data was taken at a peak intensity of 5×10^{13} W/cm^2. **d:** Events with two coincident protons from the data in panel c. **e:** Angular distributions of counts for the data from panel c (green line) and panel d (red line). The definition of proton emission angle $\alpha = \arctan(p_{pol}/p_{prop})$ is indicated in panel c. Figure taken from Ref. [52].

dispersion at a fixed peak laser intensity of 5×10^{13} W/cm^2 and linear laser polarization along the time-of-flight axis of the nanoscope. The results of the concentration scan are shown in Fig. 4.2a-c. It contains the data for protons emitted from a nanosystem (single particle or cluster), i.e., protons where a large channeltron signal was detected in coincidence with the ions. The histograms are projections of the three-dimensional momentum distribution of these protons onto the plane of polarization and propagation.

At the lowest concentration of 0.2 g/l (Fig. 4.2a), a close-to-dipolar emission pattern along the polarization direction is observed. We find a small asymmetry along the propagation direction, with more ions being emitted forward in the laser propagation direction. The asymmetry of the ion emission is a consequence of the asymmetric enhancement of the electric field on the surface of a single nanoparticle, as shown in the left-most image of Fig. 4.1. The field enhancement is shifted forwards in the laser propagation direction due to the non-negligible size of the nanoparticle compared to the laser wavelength. Quantitatively, this effect is described by the Mie solution of Maxwell's equations [40] where the quantity $\rho = kR = n\pi d/\lambda$ is the so-called size parameter [116]. If the size parameter ρ is much smaller than one, the propagation of the light field inside the spherical particle can be neglected, meaning that the phase of the light field oscillation as a function of space is approximately constant throughout the particle. In this limit, the physics can be described

by Rayleigh scattering. For practical purposes, Rayleigh scattering holds when the object's size is smaller than 1/10 of the vacuum wavelength of the incident radiation [117]. If the size parameter ρ is on the order of or larger than unity, the propagation of the electric field within the spherical object is no longer negligible, and the Mie solution needs to be applied. For the case studied here, where $d = 300\,\text{nm}$ silica spheres and an incident laser wavelength of $\lambda = 1030\,\text{nm}$ were used, the value of the size parameter is $\rho = 1.33$. This indicates the onset of Mie scattering and is reflected by the slightly forward-tilted field enhancement pattern (see Fig. 4.1) and the corresponding asymmetry in the ion emission (see Fig. 4.2). This propagation-induced asymmetry in the ion emission pattern from single nanoparticles was first reported by Rupp et al. [47].

The ion momentum distribution at higher nanoparticle concentrations, however, had not been observed previously. We found that, starting at a concentration of 0.4 g/l (see Fig. 4.2b), a forward-emitted component at large values of p_{prop} appears in the proton momentum distribution. Since this contribution dominates the momentum histogram in Fig. 4.2c at the highest studied concentration of 1.5 g/l, we concluded that it is caused by clusters in the aerosol. It should be noted that the concentration from which a cluster contribution can be observed in the proton momentum spectra depends sensitively on the steps of nanoparticle preparation, storage, cleaning, dilution, and the laser intensity. The concentration values found here should thus not be overinterpreted.

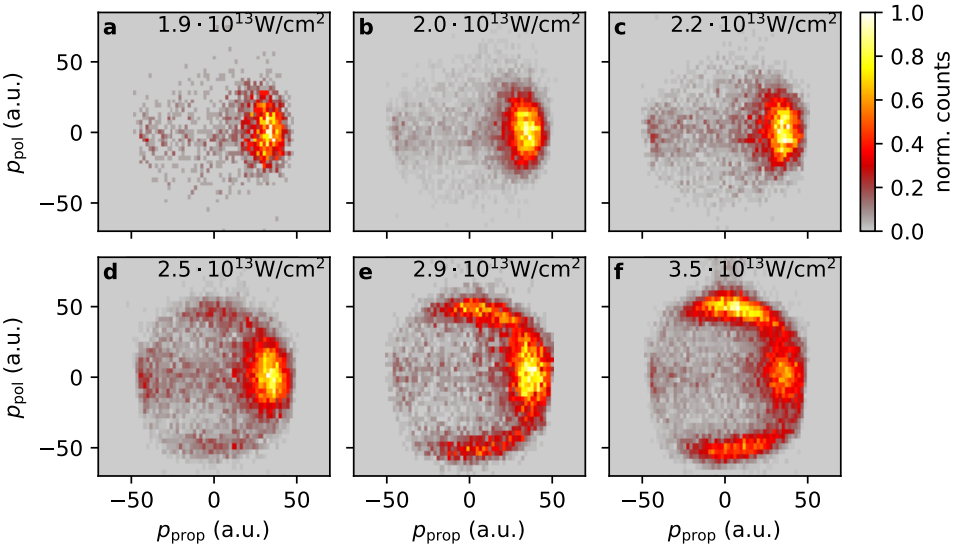

Figure 4.3: Intensity scan with 1030 nm, 40 fs laser pulses and a sample of silica nanoparticles with a diameter of 300 nm dispersed in ethanol and deionized water at a concentration of 1.5 g/l. The low-intensity data (panels a-c) only show features of nanoparticle clusters. At higher intensities, the single particle signal along the polarization direction appears (panels d-f).

4.4 Dependence on intensity and wavelength

The conclusion that the forward-emitted proton signal is related to nanoparticle clusters is further supported by the intensity dependence of the observed signal. As shown in Fig. 4.1, for $d = 300\,\mathrm{nm}$ silica particles exposed to $\lambda = 1030\,\mathrm{nm}$ light, the maximum enhancement factor for a single nanoparticle is about 1.5, while for dimers, it reaches values of up to 2.6, depending on the alignment. Combined with the nonlinear nature of the ion generation in our experiments, it is expected that at low laser intensities, only clusters of nanoparticles can be ionized and emit ions. At higher intensities, contributions of both, single nanoparticles and clusters, are anticipated. To investigate this hypothesis, an intensity scan at a high sample concentration of 1.5 g/l was carried out. The results are shown in Fig. 4.3. At peak intensities of $2.2\times10^{13}\,\mathrm{W/cm^2}$ and below (Fig. 4.3a-c) only the momentum component along the propagation direction was observed, which confirms the above hypothesis. After a mere 10% intensity increase to $2.5\times10^{13}\,\mathrm{W/cm^2}$, the dipolar single-particle signature started appearing in the momentum histogram.

Since the field enhancement of a single nanoparticle is not high enough at low intensity for substantial ionization of the surface and ion generation, low-intensity data is ideally suited for studying the pure ion signal from dimers without the contribution of protons from single nanoparticles. For this purpose, a different projection of ion momentum distribution is shown in Fig. 4.5g, where the laser propagation direction is still from left to right, but the laser polarization is perpendicular to the image plane. One can see that the forward component is, in fact, a ring-like emission pattern with a strong concentration of counts in the forward direction.

This asymmetry is once more a consequence of the propagation of the light in the nanostructure, which causes an asymmetric field enhancement, shifted forwards along the propagation direction. The field enhancement plot in Fig. 4.1 for the aligned dimer ($\theta = 0$) shows this propagation effect. Experimental evidence for this claim can be obtained from a measurement at a different wavelength, which alters the propagation effects. The OPCPA system introduced in the experimental chapter (Chapter 3) was used for this purpose. Silica nanoparticles with the same diameter of 300 nm were ionized with strong, linearly polarized laser pulses at a central wavelength of $2\,\mu\mathrm{m}$. In this case, the initial nanoparticle solvent (ethanol) was completely replaced with ultra-pure water, in contrast to the dilution of an ethanol dispersion with water that was used for the rest of the results in this chapter. Consequently, a concentration of 0.5 g/l was sufficient for observing a cluster signature. Due to the higher surface tension of water compared to ethanol, or a water-ethanol mixture, we assume that the atomizer produced larger droplets when operated with water. This increases the average number of nanoparticles enclosed in a droplet and, thereby, the cluster content in the aerosol. Fig. 4.4a shows the proton momenta in the propagation-polarization plane for the measurement at $\lambda = 2\,\mu\mathrm{m}$. The white-shaded polygon marks the single nanoparticle emission, which was confirmed by a measurement without clusters. The cluster part of the signal, outside of the polygon, is much more symmetric along the propagation direction compared to the case of the 1030 nm pulses. The symmetry corresponds to an approximately equal amount of forward and backward-emitted protons

along the laser propagation. Fig. 4.4d shows the cluster contribution to the proton signal (counts outside the blue region) in the plane perpendicular to the laser polarization. This projection makes it obvious that the proton emission from 300 nm nanoparticle dimers ionized by 2 μm laser pulses is, in fact, donut-shaped with only a slight concentration of counts in the forward direction. This is in contrast to the high propagation-induced asymmetry, which was observed at a wavelength 1030 nm (see Fig. 4.5g).

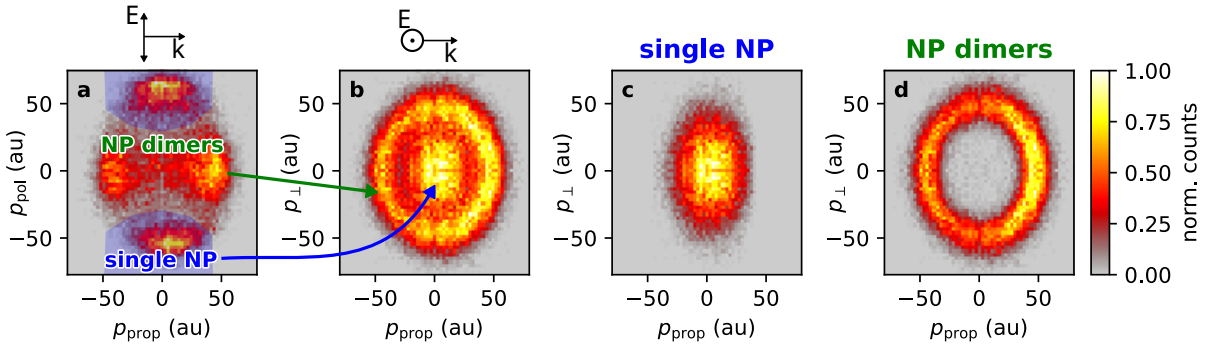

Figure 4.4: Proton Momentum histograms from a measurement of 300 nm silica particles with a central laser wavelength of 2 μm and linear polarization. **a:** Momentum histogram projected onto the plane of propagation and polarization. The blue regions define the filter used in panels c and d. Counts within the region are associated with ion emission from single nanoparticles (NP), and counts outside the region with nanoparticle dimers. **b-d:** Momentum histograms projected onto the p_{prop}-$p_\perp$ plane. Panel b shows the unfiltered proton data. Panel c only shows counts within the blue region of panel a, and panel d the counts outside the filter region. The data was symmetrized along the time-of-flight direction $p_\perp$ to remove an asymmetry due to detector saturation.

4.5 Theoretical Results

Another confirmation for the assignment of the forward-emitted component along the propagation direction to ion emission from nanoparticle dimers is provided by the results of the semi-classical model introduced in Chapter 2. A brief summary of the model will be given here. All further details can be found in the theory chapter. The model's basic assumption is that the final proton momenta are dominated by the Coulomb repulsion from the charge on the nanoparticle or nanocluster surface. The charging of the surface, as well as the generation of the protons, were modeled based on the near-field, which was obtained from the commercial Lumerical FDTD software. The generated (positive) surface charges account for the ionization of the nanosurface, i.e., the removal of electrons. While in reality, not all electrons are energetic enough to leave the nanosystem [43], we neglected this effect and introduced the total (positive) charge of the surface as an effective quantity. The spatial distribution of the positive charge on the surface was calculated from the ADK ionization rate [53] based on the local electric field on the surface. The Coulomb repulsion from these static charges was used to propagate individual (non-interacting) protons along their classical trajectories. The protons' initial positions were sampled from a distribution given

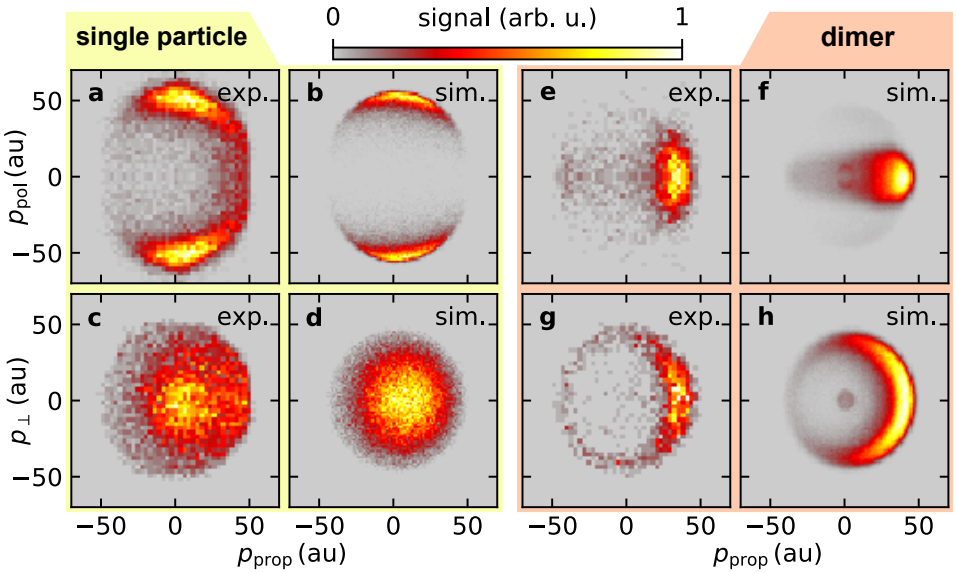

Figure 4.5: Comparison of experiment and simulation for single nanoparticles and their dimers. **a,c:** The measured proton momentum distributions from isolated nanoparticles at a peak intensity of $5 \times 10^{13}\,\mathrm{W/cm^2}$, linear laser polarization and a sample concentration of 0.2 g/l. Here, p_{pol} is the momentum component along the polarization, p_{prop} the component along the propagation direction of the laser, and $p_{\perp}$ is the momentum component perpendicular to the other two. **b,d:** The corresponding model simulations for single nanospheres. **e,g:** Experimental data for nanoparticle dimers below the ionization threshold for single nanoparticles at a peak intensity of $1.9 \times 10^{13}\,\mathrm{W/cm^2}$ and a high sample concentration (1.5 g/l). **f,h:** The model simulations for nanosphere dimers at an intensity of $1.9 \times 10^{13}\,\mathrm{W/cm^2}$. Figure taken from Ref. [52].

by the product of the local intensity enhancement to a fixed power and a radial Gaussian centered around the surface of the nanoparticle[1]. The $I^N(\mathbf{x})$ power law was implemented to model the intensity-dependent proton generation probability. For fixing the power N, the approach of Ref. [47] was followed, and $N = 13$ was used. The Gaussian distribution was used for modeling the distribution of proton-containing molecules before the arrival of the laser. A standard deviation of $\sigma = 10\,\mathrm{nm}$ was used. However, due to the large value of N and the fast decay of the near-field amplitude with distance to the nanoparticle surface, the results were robust w.r.t. to changes of the standard deviation σ.

As mentioned above, the total surface charge in the model is an effective charge. Here, it is obtained by fitting the mean energy of the simulated protons emitted from single nanoparticles to the experimental data. A second fit for nanoparticle dimers is *not* required (explanation follows below). For the single nanoparticle simulation results, which are compared to the experiment in Fig. 4.5a-d, the total charge was set to be $\approx 1600e$, where e is the elementary charge. Note that this approach of determining the total surface charge differs slightly from the method described in Chapter 2, which was developed later and only applied to the results presented in Chapter 5.

The predictions of the model and the corresponding experimental data on single nanoparticles and clusters are shown in Fig. 4.5 and Fig. 4.6. The overall good and almost quantitative agreement between the model and the experiment shows that a treatment of the electron-ion interaction via an effective surface charge is feasible. For single nanoparticles, this holds for both projections displayed in Fig. 4.5a,b and c,d and for the one-dimensional distribution in Fig. 4.6a-c.

A good predictive power of the model for a single nanoparticle is a requirement for its application to clusters of nanoparticles, in this case, dimers. The theoretical results for dimers shown in Fig. 4.5 and Fig. 4.6 were calculated by averaging over approximately 600 random dimer orientations. The random orientations were generated by projecting a vector of three Gaussian ($\mu = 0$, $\sigma = 1$) random numbers onto the unit sphere. This method is the same as that described in Chapter 2 for uniformly sampling random points on the surface of a sphere. It ensures averaging over *uniformly* random distributed dimer orientations [62, 63]. To increase the computational efficiency, however, a higher number of samples for small alignment angles $\theta < 30°$ was used. As Fig. 4.7 shows, 95% of all protons are emitted under such small angles for a power law of I^{13}. The altered sampling density was accounted for in the averaging procedure by applying appropriate weighting factors. Apart from these sampling weights, the ion yields for different dimer orientations were weighted based on the relative number of expected protons generated from a dimer in a certain orientation. The proton number is proportional to the integral of the initial proton distribution (power law × Gaussian), which was evaluated using Monte-Carlo integration (see also Chapter 2).

As mentioned above, the total surface charge on a nanoparticle dimer was determined by rescaling the result of the fit carried out for the single-particle case. The fit effectively fixes the number of neutral atoms per volume. It can thus be used to calculate the total charge

[1] For a nanoparticle cluster, one Gaussian per nanoparticle was used.

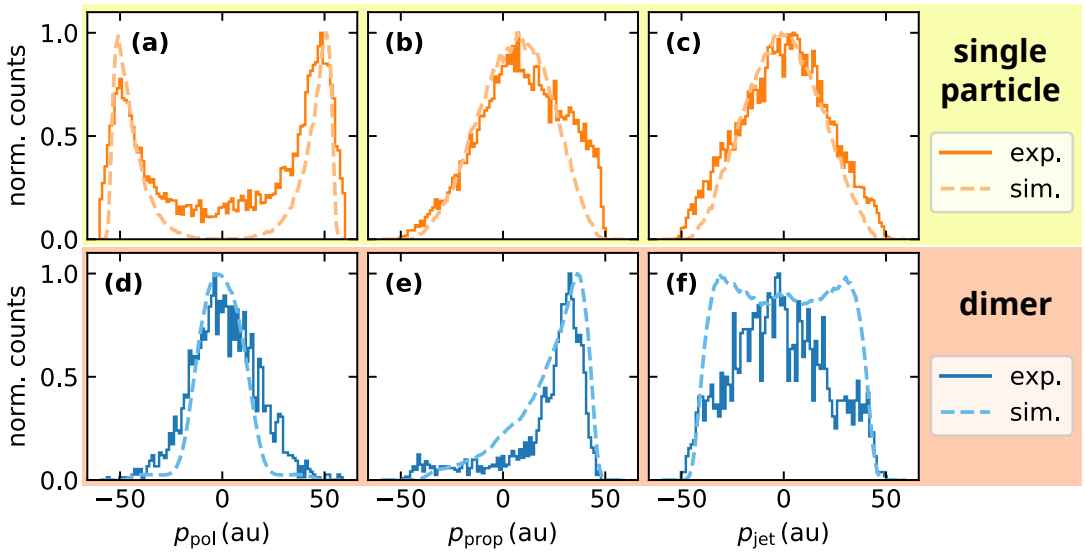

Figure 4.6: Projected proton momentum distributions for single nanoparticles and dimers. One-dimensional momentum distributions for single silica nanoparticles and nanoparticle dimers. The projections are obtained from the data in Figure 4.5. Simulated data are shown as dashed lines, and measured data are shown as solid lines. The top row contains the single particle results (panels a-c). The results for dimers are shown in the bottom row (panels d-f). Panels a,d show the momentum component along the laser polarization, panels b,e the component along the laser propagation axis, and panels c,f show the component perpendicular to the other two. Figure taken from Ref. [52].

consistently for a different system (i.e., more nanoparticles) or at a different intensity. In practice, the ratios of ionization probabilities between the single particle and dimer were again determined by Monte Carlo integration and used for a consistent scaling of the total surface charge. For example, for the dimer aligned along the laser polarization, at an intensity of $1.85 \times 10^{13}\,\mathrm{W/cm^2}$, this procedure yielded a total charge of approximately $400e$. The corresponding results averaged over all dimer orientations are shown in Fig. 4.5e-h.

Overall a high degree of agreement between the simulation and the experimental data was found. Both simulated projections of the three-dimensional momentum histogram share the characteristic features seen in the experiment. The heavily forward-concentrated proton emission in the propagation-polarization (see Fig. 4.5e,f) plane, as well as the ring-like structure in the plane perpendicular to the polarization (see Fig. 4.5g,h) are reproduced by the model. Only the angular region within which the counts are concentrated is predicted to be larger than experimentally observed. This effect is most visible in Fig. 4.6f, the one-dimensional momentum projection onto the $p_\perp$ axis. Since the angular distribution of the ions is heavily determined by their initial position, the narrower experimental distribution hints at a more confined ion emission than assumed by the model. Therefore, the agreement between theory and experiment could be improved by a stronger confinement of the protons' initial distribution. This would require a more nonlinear ion generation law, for example, by using a larger exponent in the power law. However, for the sake of consistency with the previous work by Rupp et al. [47], and for testing the

extensibility and applicability of the corresponding results, the photon-energy corrected value of $N = 13$ was chosen here. The exponent of the power law was only based on a different ionization potential for the results presented in the next chapter, where the main proton origin was identified as the silanol groups on the silica surface instead of physisorbed molecules of water or ethanol.

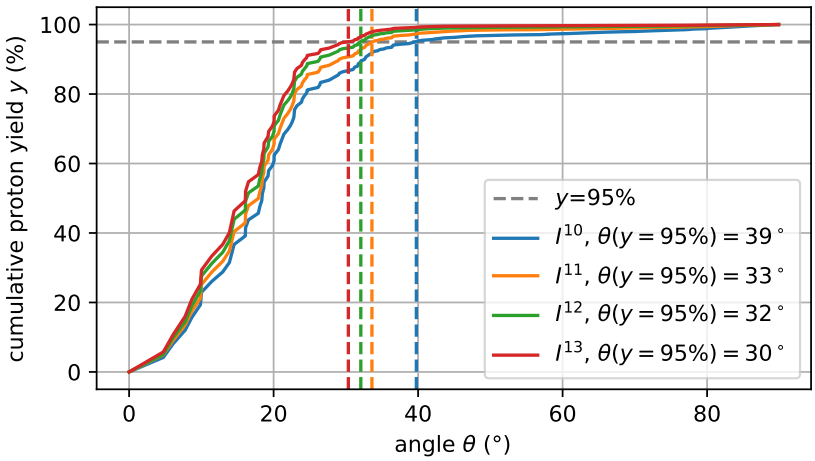

Figure 4.7: The cumulative proton yield y from dimers for all angles smaller than θ, the angle between the laser polarization and the dimer axis. A selection of power laws is shown, I^{13} was used in Ref. [52] and the other results presented in this chapter. The vertical dashed lines indicate the angle, which corresponds to a cumulative yield of 95%.

4.6 Coincident ion emission

While the above paragraphs have provided sufficient evidence that ions emitted in the plane perpendicular to the laser polarization indicate nanoparticle clusters, the inverse statement, i.e., the possibility of clusters producing a dipolar ion signal along the polarization direction, has not been discussed yet. This question requires some attention since the field enhancement at the poles of a single nanoparticle is approximately equal to the magnitude of the field enhancement on the outer poles of an aligned dimer (see Fig. 4.1). This means that both, single nanoparticles and clusters, can, in principle, produce ions emitted along the polarization direction. To which extent clusters contribute to the dipolar part of the ion momentum spectra depends on the ratio between single nanoparticles and clusters in the aerosol stream. This fact will be utilized in the discussion section.

To investigate the contribution of clusters to the dipolar ion emission, we employed events where two protons were detected in a single shot in coincidence with a high channeltron signal (indicating a nanoparticle hit). The momentum histogram for coincidentally detected protons from 300 nm silica particles is shown in Fig. 4.2d. The data is a subset of the measurement at the highest concentration in Fig. 4.2c. The absence of the cluster

signature after a simple selection of coincident proton events is striking. In Fig. 4.2d, two kinds of regions are defined. Region I contains the dipolar emission, and region II contains the inner part where the cluster signal might be expected. In fact, coincidences, where both protons are detected in region II, are not detectable with our reaction nanoscope due to the 30 ns dead time of the ion detector[2]. This can be seen on the time-of-flight scale on the vertical axis of Fig. 4.2c. However, the detection of one ion in region I and the other ion in region II is not dead-time limited. Still, the counts in region II are very scarce. This means that the predominant case is the emission of both ions in region I, where one ion arrives early (TOF $\approx$ 600 ns) and the other one arrives late (TOF $\approx$ 720 ns). From this observation, we conclude that the forward-emitted momentum component and the dipolar, single-particle signature were generated quasi-independently of each other in our experiments. At high enough sample concentrations and laser intensities, this might not be the case anymore.

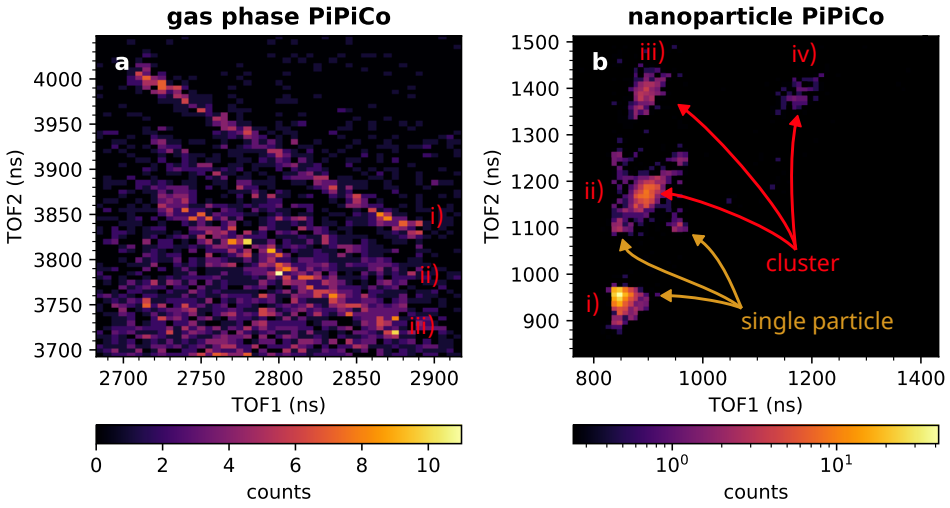

Figure 4.8: Typical **P**hoto**i**on-**P**hoto**i**on **Co**incidence (PiPiCo) spectra for gas-phase data and nanoparticle data. **a:** PiPiCo histogram for the C-C bond breaking in ethanol. i) methyl ion + methoxy ion, ii) methyl ion + CH_2O^+, iii) methyl ion + CHO^+. **b:** PiPiCo histogram for nanoparticle data ($d = 300$ nm silica particles in ethanol and water). i) proton + proton, ii) proton + H_2^+, iii) proton + H_3^+, iv) H_2^+ + H_3^+. As indicated by the colored arrows, coincident ions from clusters lie on diagonals with a positive slope, and coincidences from single nanoparticles lie on the corners of a rectangle. For the proton-proton coincidences, due to the detector's dead time, only the "top-left" corner is observed. Note that this pattern is only valid for linear laser polarization along the time-of-flight axis of the nanoscope and minor propagation effects in the single particles.

The previous paragraph demonstrates that an analysis of coincident events in reaction nanoscopy can be beneficial for understanding the underlying physical processes. Com-

[2]The dead time of a delay-line anode can be as short as $\approx$ 10 ns. In the case of this measurement, the settings of the constant fraction discriminator of the MCP were not chosen ideally, which led to a longer dead time.

pared to coincidences from the Coulomb explosion of single molecules, however, coincidences from ions originating from a nanosurface are not quite as powerful since reaction nanoscopy experiments are not kinematically complete [118]. The incompleteness in reaction nanoscopy causes unique structures in the photoion-photoion coincidence (PiPiCo) histograms which are distinctively different from the typical signatures of Coulomb explosions. Fig. 4.8a shows the PiPiCo histogram for the process of C-C bond breaking in doubly ionized ethanol. The top-most line (label i)) corresponds to the detection of a methyl ion ($m = 15\,\mathrm{u}$) and a methoxy ion ($m = 31\,\mathrm{u}$) in coincidence. In this case, all ions involved in the Coulomb explosion are detected, resulting in a sharp line with a negative slope due to momentum conservation. For lines ii) and iii) of Fig. 4.8a, one or two protons, respectively, are missing from the methoxy ion, which leads to an incomplete momentum and a slight broadening of the PiPiCo lines. Due to the low statistics and the warm jet of the reaction nanoscopy, this broadening effect is not easily visible here. For a clearer example, see, for instance, Ref. [119]. In contrast to the gas-phase PiPiCo structures, there are no sharp lines visible in the case of ion coincidences from the emission from the surface of a nanoparticle or cluster. This is obvious since the heaviest interaction partner, the nanosystem, is not detected in the experiment, which leads to an incomplete momentum sum. A nanoparticle PiPiCo histogram is displayed in Fig. 4.8b. The time-of-flight ranges on both axes correspond to the ions H^+, H_2^+, and H_3^+. The shape of the coincidences between H^+ and H_2^+ is the most general shown here. It consists of four blobs forming a rectangle whose positive diagonal contains additional counts. The coincidences involving the H_3^+ ion (labels iii) and iv)) only show the diagonal part. The proton-proton coincidence (label i)), as explained above, are dead-time limited, which only leaves the counts in the top-left corner of the full rectangle. Based on the ion time-of-flight, it can be concluded that the counts on the diagonal correspond to ions emitted from nanoparticle clusters. The corner counts are coincidences from single particles, as indicated by the labels in Fig. 4.8b. The four corners of the rectangle correspond to the different combinations of the ions being emitted toward or away from the detector, respectively. Due to the presence of the nanoparticle, the emission directions directly correspond to the emission from one side of the nanoparticle or the other. This is illustrated in Fig. 4.9.

4.7 Discussion

Ratio between single particles and dimers

The good reproduction of the experimental results by the dimer model, the concentration scan data, as well as the size-selective elements of the nanoparticle source (impactor and aerodynamic lens, see Section 3.1) allow for the conclusion that the protons emitted along the propagation direction of the laser are indeed predominantly generated on the surface of nanoparticle *dimers* with a negligible contribution of larger clusters. Hence, the separation between the cluster-related part of the momentum histogram and the single-nanoparticle component in the concentration scan results (Fig. 4.2) can be used for carrying out an

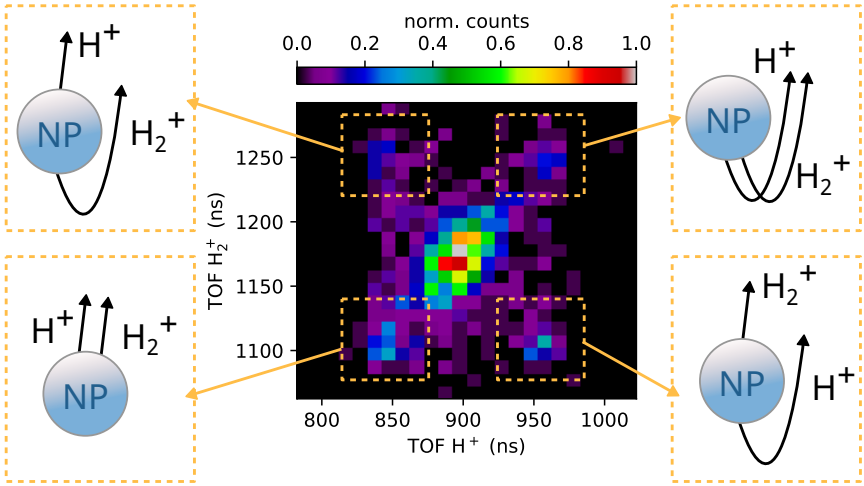

Figure 4.9: PiPiCo histogram of H^+ and H_2^+ ions generated on nanoparticle surfaces (data filtered on high channeltron signal). The boxes in the four corners correspond to different combinations of ion birth positions on the surface of a single nanoparticle (NP). This is indicated in the sketches in the dashed boxes. The detector is assumed to be on the top end of the sketches. Small TOF values correspond to the emission of an ion toward the detector, and large TOF values to the emission away from the detector. Due to the presence of a nanoparticle, the emission direction and the birth position are linked. The histogram data outside of the dashed regions correspond to the emission from nanoparticle clusters.

estimate of the monomer-dimer ratio in the focal volume. For this purpose, the definition of region I and II Fig. 4.2d is used. While it would be straightforward to define counts in region I as "single nanoparticle signal" and, correspondingly, counts in region II as "cluster signal," there is a small contribution of either one of these categories to the other region. To quantify this, we denote the total number of proton counts in region I or II as N_I or N_II, respectively. Both of these contain protons originating from both, single nanoparticles (s) and dimers (d):

$$N_\mathrm{I} = N_\mathrm{I}^{(s)} + N_\mathrm{I}^{(d)}, \qquad N_\mathrm{II} = N_\mathrm{II}^{(s)} + N_\mathrm{II}^{(d)}, \tag{4.1}$$

To disentangle the individual contributions, we use the coincident proton data of Fig. 4.2d and the low-intensity measurement of Fig. 4.5e. The former is taken as pure single nanoparticle emission, which enables the extraction of the ratio $\gamma_s = N_\mathrm{I}^{(s)}/N_\mathrm{II}^{(s)} = 5.5$, i.e., the ratio between the counts in region I and II for a single nanoparticle measurement. The low intensity data is used analogously for the ratio $\gamma_d = N_\mathrm{I}^{(d)}/N_\mathrm{II}^{(d)} = 0.035$, which describes a typical cluster measurement. Under the assumption that these ratios also hold for the concentration scan data of Fig. 4.2, one can rewrite Eqs. (4.1) to obtain

$$\begin{pmatrix} N_\mathrm{I} \\ N_\mathrm{II} \end{pmatrix} = \begin{pmatrix} 1 & 1 \\ \frac{1}{\gamma_s} & \frac{1}{\gamma_d} \end{pmatrix} \begin{pmatrix} N_\mathrm{I}^{(s)} \\ N_\mathrm{I}^{(d)} \end{pmatrix} = \mathbf{R_I} \begin{pmatrix} N_\mathrm{I}^{(s)} \\ N_\mathrm{I}^{(d)} \end{pmatrix}, \tag{4.2}$$

$$\begin{pmatrix} N_\mathrm{I} \\ N_\mathrm{II} \end{pmatrix} = \begin{pmatrix} \gamma_s & \gamma_d \\ 1 & 1 \end{pmatrix} \begin{pmatrix} N_\mathrm{II}^{(s)} \\ N_\mathrm{II}^{(d)} \end{pmatrix} = \mathbf{R_{II}} \begin{pmatrix} N_\mathrm{II}^{(s)} \\ N_\mathrm{II}^{(d)} \end{pmatrix}. \tag{4.3}$$

Inverting the matrices $\mathbf{R_I}$ and $\mathbf{R_{II}}$ thus allows us to determine the individual contributions of single nanoparticles and clusters from the total number of proton counts in region I (N_I) and II (N_II). The results are summarized in Table 4.1. For the lowest concentration of 0.2 g/l in Fig. 4.2a, a dimer content of $(14 \pm 1)\%$ was found. The values at higher concentrations were $(33 \pm 1)\%$ dimers at 0.5 g/l (Fig. 4.2b) and $(60 \pm 1)\%$ at 1.5 g/l. The error was estimated by treating the experimental value $\gamma_d = 0.035$ as an upper limit: $\gamma_d \leq 0.035$.

	N_I	$N_\mathrm{I}^{(s)}$	$N_\mathrm{I}^{(d)}$	N_II	$N_\mathrm{II}^{(s)}$	$N_\mathrm{II}^{(d)}$	$N^{(s)}$	$N^{(d)}$	$\frac{N^{(d)}}{N^{(s)}}$	$\frac{N^{(d)}}{N^{(s)}+N^{(d)}}$
(a) 0.2 g/l	**5986**	5947	39	**2195**	1081	1114	7028	1153	0.16	**0.14**
(b) 0.5 g/l	**7180**	7044	136	**5178**	1281	3897	8325	4033	0.48	**0.33**
(c) 1.5 g/l	**6769**	6389	380	**12021**	1162	10859	7551	11239	1.49	**0.60**

Table 4.1: Determination of the ratio between protons emitted from single nanoparticles and protons emitted from dimers. The data is taken from the histograms a-c of Fig. 4.2 (panel indicated by the label in the first column). $N^{(s)}$ and $N^{(d)}$ denote the number of protons assigned to single particle events and dimer events, respectively. See the text for the definitions of the other quantities.

Alignment-selective proton emission

The high predictive power of the model allows an analysis of the contribution of different dimer alignments with respect to the laser polarization axis. As mentioned above, dimers aligned at angles $\theta \leq 30°$ produce 95% of the total proton signal. The full cumulative distribution is shown in Fig. 4.7. For such aligned dimers, the vast majority of protons (99,6%) are generated around the contact point between the two nanoparticles, where the field enhancement is highest (see Fig. 4.1). The alignment, in combination with the proton creation at the contact point, gives rise to the ring-like momentum distribution observed in the plane perpendicular to the polarization axis (see Fig. 4.4d and Fig. 4.5g,h). The remaining 0.4% of protons originate from the outer poles of the dimer and are emitted under a small angle along the polarization axis. This theoretical number is consistent with our experimental observation that the nanoparticle signal and the dimer signal have a very small overlap in the momentum histogram, which allows a separation of the corresponding signals.

Limits of the cluster detection

The limits of this kind of separation scheme are set by the Mie-Parameter. The larger the nanoparticles or the shorter the wavelength becomes, the more will the propagation of the electric field inside the nanosphere cause a forward shift of the regions of field enhancement along the propagation direction. Therefore, the overlap between the single particle proton momentum histogram and the dimer proton momentum histogram will grow with the Mie-Parameter. In order to investigate this effect and find the limit of the proton-momentum-based distinction between single nanoparticles and clusters, further

simulations were carried out. The results suggest that they are distinguishable for a Mie-Parameter of up to $\rho \approx 1.8$. At a wavelength of 1030 nm, this corresponds to a maximum particle diameter of 590 nm. For a fixed particle diameter of 300 nm, the shortest usable wavelength would be approximately 520 nm.

In addition, the model was tested on larger clusters using closely packed trimers of silica nanoparticles with a diameter of 300 nm irradiated by a 1030 nm laser pulse. Due to the same alignment effect as for the dimers, combined with a strong propagation effect, the protons generated from trimers will still be favorably emitted in the forward direction. The overlap with the signal from single nanoparticles, however, stays insignificant. Consequently, the separation of signals from differently sized clusters is challenging, while a distinction between ion signals from single nanoparticles and small clusters remains feasible.

Impact on related work

A major result of our work on the ion emission from nanoparticle clusters is the dominance of cluster-emitted ions at low laser intensities due to the higher field enhancement factor reached on the surface of clusters compared to single nanoparticles. This observation is a potential explanation for discrepancies between theory and experiment in earlier strong-field experiments with silica nanoparticles. For low laser intensities ($\leq 1.5 \times 10^{13}\,\mathrm{W/cm^2}$), Zherebtsov et al. [41] as well as Rupp et al. [120] have reported higher experimentally observed cutoffs in the photoelectron energy spectra than predicted by their theory. The authors used the $\mathrm{M^3C}$ model [46], which only describes the light-matter interaction and the electron emission for single nanoparticles. The missing contribution of electrons emitted from nanoparticle clusters is a possible explanation for the reported discrepancy since clusters give rise to a higher local intensity compared to a single nanoparticle, which increases the final electron energy (in strong-field electron emission in general [121] and also for electron emission from nanoparticles in strong fields [122]).

However, a systematic investigation of this hypothesis is still missing. The experimental challenge is the combined measurement of the electron energy with an (ion-based) cluster detection. A possible implementation could use a double-sided velocity map imaging spectrometer similar to the instrument presented in Ref. [123].

4.8 Conclusions

In this chapter, the capability of the reaction nanoscopy technique to distinguish between single nanoparticles and clusters of nanoparticles in an aerosolized mixture was demonstrated. We showed that ion emission in the plane perpendicular to the laser polarization is a clear indication of nanoparticle clusters as long as the individual nanoparticles are sufficiently small compared to the laser wavelength. For d =300 nm silica nanoparticles ionized and a laser wavelength of 2000 nm, an almost isotropic ion emission around this plane was observed, and only a minor propagation-induced asymmetry was seen in the momentum

histograms. For the same nanoparticles ionized and a wavelength of 1030 nm, it was shown here and in Ref. [52], that the propagation of the electric field in the nanoclusters leads to a strong forward concentration of proton counts within this plane.

The corresponding experimental data is well reproduced by a semi-classical Monte-Carlo model. The near-field driven charge generation using quasi-static ADK ionization and ion generation based on a multi-photon process combined with classical Coulomb interaction and propagation resulted in a close-to-quantitative agreement between theory and experiment. We have furthermore applied the model to a range of particle and cluster sizes and found that a momentum-based differentiation between ions emitted from clusters vs. single particles is applicable as long as the propagation effects in a single nanoparticle remain small, and the field enhancement pattern is close to a dipolar shape.

In addition, a comparison between the PiPiCo histograms for gas-phase and nanoparticle/cluster ion emission was carried out, and the physical meaning of the different features was explained. The cluster-related part of the PiPiCo histogram was shown to be isolated from the single nanoparticle contribution allowing for a coincidence-based separation of the ion signals. This proves that coincident ion data in reaction nanoscopy can be a valuable source of information despite the absence of complete momentum information in reaction nanoscopy compared to the reaction microscopy technique (where kinematically complete experiments are possible).

Lastly, we found that nanoparticle clusters are the dominating ion source at low laser intensities due to the typically higher field enhancement around clusters of nanoparticles compared to single nanoparticles. This observation is a possible explanation for previously reported discrepancies in studies on strong-field electron emission from silica nanoparticles [41, 120], where the experimentally observed electron energy cutoff was higher than predicted by theory. In general, the results presented here show that the contribution of clusters in experiments on aerosolized nanoparticles can be significant and even dominant for certain experimental parameters like low laser intensity or high sample concentration. Consequently, thorough sample handling and preparation, the choice of a suitable laser intensity, as well as careful data interpretation are of utmost importance for any related work on strong-field ion or electron emission from aerosolized nanoparticles.

Chapter 5

Elliptically polarized near-fields and the role of functional surface groups

In the following, the reaction nanoscopy results obtained from the ionization of single silica nanoparticles ionized with close to few-cycle laser pulses at a central wavelength of 2 μm will be presented. It will be demonstrated that the model introduced in Chapter 2 and used in the previous chapter is still capable of predicting the angular ion distribution at the longer wavelength and that it can be applied to arbitrarily elliptical laser polarizations. The limitations of the current model will be pointed out, and first experimental results necessitating future improvement of the theory will be presented. These results prove that covalently bound surface groups are the dominant source of ions in reaction nanoscopy and that the solvent of the initial nanoparticle dispersion can be neglected to a large part. This will help to advance the microscopic description of the ion generation from molecules adsorbed on nanoparticle surfaces.

Most of the results presented in this chapter were published in Ref. [50].

5.1 Introduction

The study of the interaction of nanoparticles with strong laser fields has been an active area of research for over a decade now [41, 124]. During that time, many research groups have been focusing their attention on the electron emission process, which has resulted in the discovery of many new phenomena and the development of suitable theoretical modeling [46]. For instance, it has been demonstrated that tailored light fields can be used to control the photoemission by steering electron trajectories [42] and modifying their backscattering dynamics. The elastic electron backscattering has been shown to be strongly influenced by the presence of the highly ionized nanoparticle [43] and the inelastic electron scattering inside the nanoparticle material was quantified using attosecond streaking [44]. With electron emission experiments, it was furthermore shown that the light-matter interaction can alter the properties of the nanoparticle material on sub-cycle time scales [45, 120, 125].

A crucial contribution to these insights was the mature theory for strong-field photoe-

mission from nanoparticles [46]. While numerous studies on the ion emission from strong-field ionized nanoparticles have been carried out by now[47–50, 52, 126], the theoretical description of the process is not very rigorous, especially in the intensity regime below the onset of plasma formation. Here, we present experimental data that extend the experimentally covered parameter space and provide new microscopic insights into the surface composition of silica nanoparticles in reaction nanoscopy. Both of these aspects are crucial for further developments of reaction nanoscopy and the theoretical description of the corresponding results.

Prior to when the results of this chapter were obtained, reaction nanoscopy had only been applied to silica nanoparticles with linearly polarized laser fields with wavelengths of 720 nm [47] and 1030 nm [52, 127]. In all cases, a close correspondence between the local near-field on the surface of the nanoparticle and the angular distribution of the emitted ions was reported, which has allowed the mapping of reaction yields on the nanoparticle surface with nanometer resolution. In this context, however, two questions are still not completely answered. The first question is how well the yield imaging concept for regions of enhanced field generalizes for different parameters, such as wavelength or polarization. The second question concerns the molecular origin of the observed reaction products. Rupp et al. [47] hypothesized that the measured proton yield mostly originated from physisorbed molecules. The assumption was based on the fact that the nanoparticles were dispersed in ethanol or water, and when the corresponding ionization potentials were used in the model, no obvious disagreement between theory and experiment was found. The first indication that this understanding cannot be entirely correct can be found in a study by Alghabra et. al [127]. In this case, dried nanoparticles were dispersed in pure deuterated water, and still, a strong signal of protons was observed in the time-of-flight histograms recorded with the nanoscope.

In this chapter, we present experimental reaction nanoscopy results where 300 nm silica nanoparticles were ionized by 2 μm laser pulses with different ellipticities, investigate the applicability of the previously introduced model (see Chapter 2) and discuss its limitations. We complement this with a systematic investigation of the surface composition of silica nanoparticles in the interaction region of the reaction nanoscope. Using experimental data obtained after the exchange of the nanoparticle solvent with the fully deuterated counterpart, we gain quantitative insight into the contribution of chemisorbed and physisorbed surface molecules to the ion yield in typical reaction nanoscopy experiments. These results pave the way for a more accurate description of the strong-field ion emission from nanoparticles with the potential inclusion of the microscopic details of the molecular structure on the nanosurface.

5.2 Experimental Methods

A brief summary of the experimental methods used for the results of this chapter will be given in the following. For more details, the reader is referred to Chapter 3.

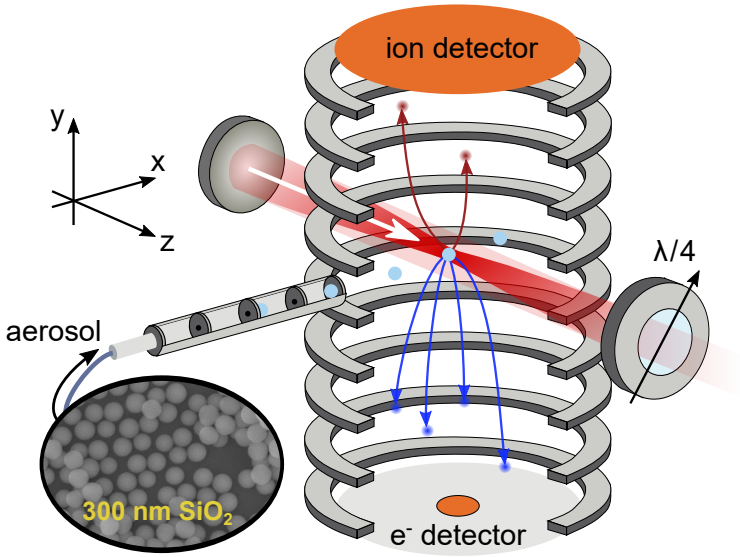

Figure 5.1: Experimental setup. A stream of silica nanoparticles (cyan) with a diameter of 300 nm is collimated by an aerodynamic lens and injected into the reaction nanoscope. A spherical mirror focuses the laser pulses onto the nanoparticles, and the generated electrons (blue) and ions (red) are detected by a channeltron and a delay-line detector, respectively. A quarter-wave plate ($\lambda/4$) is used to adjust the ellipticity of the laser pulses. The indicated coordinate system is used throughout Chapter 5. Figure taken from Ref. [50].

5.2.1 Laser system

For the strong-field ionization of the nanoparticles, we used a home-built laser system with a central wavelength of 2 μm, a pulse duration of 25 fs, a repetition rate of 100 kHz and a maximum average power of 10 W based on optical parametric chirped-pulse amplification [81]. The laser power was controlled by a broadband half-wave plate in combination with a wire-grid polarizer. The ellipticity of the laser pulses was adjusted with a broadband quarter-wave plate (wave plates: B. Halle Nachfl. GmbH, RAC 6L series).

5.2.2 Reaction nanoscope

Inside the reaction nanoscope, the laser pulses were back-focused with a spherical silver mirror ($f = 75$ mm). The laser focus and the nanoparticle stream were overlapping in the interaction region of the reaction nanoscope where laser intensities on the order of 10^{13} W/cm^2 were reached, leading to strong-field ionization of the nanoparticle surface. The generated electrons and ions were detected by a channeltron electron multiplier and a delay-line detector (DLD80, RoentDek Handels GmbH), respectively. A homogeneous electric field of approx. 100 V/cm was used to force the particles onto the corresponding detectors. The three-dimensional ion momentum was reconstructed from the ions' impact position on the detector and their time-of-flight, as described in Chapter 3. The detected electron signal was used to differentiate nanoparticle ionization events with a high number of generated electrons from the ionization of single background molecules with very small

or entirely absent electron signals. For this purpose, the decoupled voltage signal from the channeltron signal was sampled with a fast analog-to-digital converter (fADC4, RoentDek Handels GmbH) and time-integrated. The setup as well as the coordinate conventions are depicted in Fig. 5.1. The laser propagation direction is denoted by z, the ion detector plane is the x-z plane and the time-of-flight axis is y. The polarization plane is spanned by the time-of-flight axis y and the x-direction.

5.2.3 Nanoparticle Delivery

For this study, spherical silica nanoparticles with a diameter of 300 nm were used. The particles were dispersed in three different solvents: ethanol (Fisher Chemical, ≥99%), methanol (Thermo Scientific, 99%) or methanol-d4 (ACROS Organics, 99.6 at% D). The particles were aerosolized using an atomizer (TSI inc., model 3076) with argon as the carrier gas. The generated aerosol was dried with a counter-flow membrane dryer (PermaPure MD-700-48S) and the cluster content was minimized by an impactor (TSI inc., part no. 1035900). The pressure of the aerosol was reduced to 1 atm by a HEPA filter connected to ambient air. This pressure was required by the aerodynamic lens [78] used for the generation of a collimated stream of nanoparticles. The stream was differentially pumped in three stages before the interaction region of the nanoscope.

5.2.4 Nanoparticle synthesis

The spherical silica nanoparticles with a mean diameter of 300 nm were synthesized by Ana Sousa-Castillo in the group of Stefan A. Maier at LMU using a modified version of the Stöber method [72]. The required chemicals of tetraethoxysilane (TEOS, ≥98%), ethanol (EtOH, absolute), and ammonia solution (NH_4OH, 27 wt % in water) were purchased from Sigma-Aldrich. Water with a resistivity of 18.2 MΩcm and a total organic content of less than 3 ppb was obtained from a Millipore Milli-Q water purification system. For the particle synthesis, 1.7 ml of TEOS was added to a solution containing ethanol (18.12 ml), ammonium hydroxide (1.96 ml), and water (3.21 ml). This mixture was stirred at room temperature for 2 h and then purified by three subsequent cycles of centrifugation, solvent removal, and redispersion cycles with ethanol (6000 rpm, 10 min). The size and morphology of the silica nanoparticles were characterized using a transmission electron microscope (TEM, JEOL1020) operating at a voltage of 80 kV. A standard deviation of 6% for the size distribution of the nanoparticles was obtained from the electron microscope image. The procedure is described in the experimental chapter (Chapter 3). All samples were stored in anhydrous ethanol after cleaning. The solvent replacement was achieved by the same cycles of centrifugation, solvent removal, and redispersion in fresh solvent as for the purification step after the synthesis. Before using the samples in the experiment, they were diluted to a concentration of 1 g/l in order to minimize the number of clusters in the nanoparticle stream. A low contribution of nanoparticle clusters to the ion spectra was verified using the methodology introduced in the previous chapter and reported in Ref. [52].

5.3 Theoretical model

The ideas and principles of the model have been described in great detail in Chapter 2. It is, to a large extent, identical to the modeling of the results on nanoparticle clusters presented in the previous chapter. The only changes made were of evolutionary nature and were based on the results below. These adjustments mainly concern the description of the proton generation. As a reminder, the initial positions of the protons are sampled from a distribution, which is the product of an intensity-dependent power law and a Gaussian function centered around the nanoparticle surface. The latter is responsible for modeling the density of (proton-emitting) molecules at the surface. The standard deviation of this Gaussian function was reduced to $\sigma_r = 1\,\mathrm{nm}$ (from a value of $\sigma_r = 10\,\mathrm{nm}$ in the previous chapter). This modification was made to account for the high degree of evaporation of solvent molecules, which we will prove further below. While the reduction by a factor of 10 might sound significant, the second factor, the dependence of the proton generation probability on the local intensity, still dominates the overall probability distribution. The large exponent in the corresponding power law leads to an extremely fast decay of the proton generation probability with distance from the nanoparticle surface, which causes a narrower radial distribution than what is set by the Gaussian with $\sigma_r = 1\,\mathrm{nm}$. This shows the great sensitivity of the reaction nanoscopy technique to the very surface of the nanosystem (at least theoretically). Like the standard deviation of the Gaussian, the exponent of the I^N power law was adjusted compared to what was used for the description of the results on nanoparticle clusters. The exponent N is determined by and equal to the number of photons needed to energetically overcome the ionization potential of the molecule or surface group, which is assumed to be the source of protons. As our results below will show, the main proton sources in our experiment were silanol groups (Si-O-H) on the nanoparticle surface. We, therefore, used the ionization potential I_p =13.0 eV of the OH radical [128] for calculating the exponent. With a photon energy of $E_\gamma = 0.62\,\mathrm{eV}$ at the central wavelength of $2\,\mu\mathrm{m}$, an exponent of $N = 21$ was obtained.

5.4 Results

The first reaction nanoscopy data produced with a laser wavelength of $2\,\mu\mathrm{m}$ is displayed in Fig. 5.2B. It shows the proton momentum distribution projected onto the polarization plane for linearly polarized light. As observed previously for shorter wavelengths [47, 50], the proton momentum histogram appears to be closely related to the field enhancement on the nanoparticle surface (Fig. 5.2A).

In order to further test the generality of this mapping between the near-field amplitude and the angular ion distribution, the polarization of the laser pulses was altered with a quarter-wave plate. Fig. 5.2 contains three different polarization states, linear, elliptical, and circular, which are indicated by the gray symbols. They correspond to wave plate settings of 0°, 35°, and 45°, respectively. The 35° position of the wave plate produced an elliptical polarization with a ratio of the main axes of $b/a = \tan(35°) \approx 0.7$

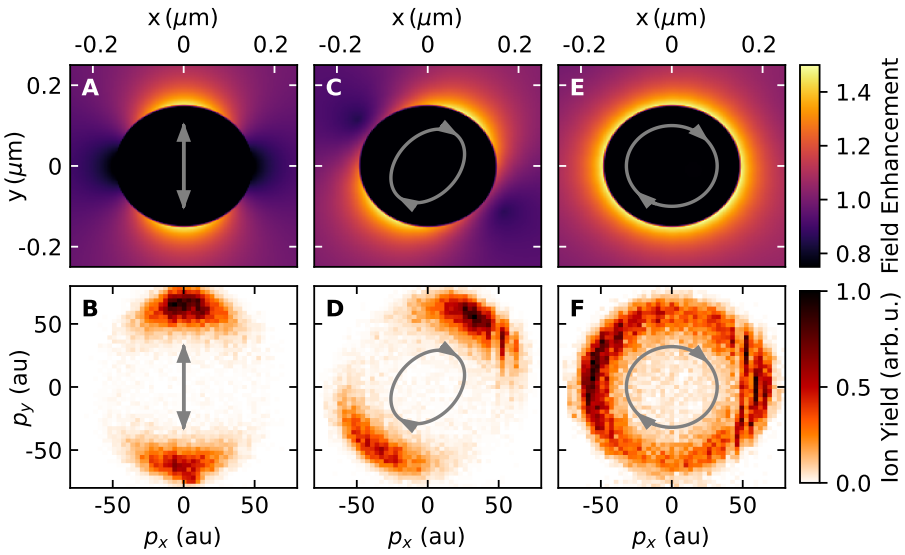

Figure 5.2: Field enhancement and proton momentum distributions for different ellipticities. **A,C,E:** Field enhancement in the polarization plane (x-y) through the center of a $d = 300\,\mathrm{nm}$ silica nanoparticle at the coordinate origin. **B,D,F**: Projection of the 3D momentum distribution for protons onto the polarization plane (x-y). **Left column:** Linear polarization (quarter-wave plate at 0°). **Middle column:** elliptical polarization (quarter-wave plate at 35°). **Right column:** circular polarization (quarter-wave plate at 45°). All proton data acquired with a pulse energy of $18\,\mu\mathrm{J}$, which corresponds to a peak intensity of $2 \times 10^{13}\,\mathrm{W/cm^2}$ for the case of linear polarization. Figure taken from Ref. [50]

(see Appendix A). For all three polarizations, a high correlation between the near field enhancement factor obtained from FDTD calculations (Fig. 5.2A,C,E) and the proton momentum in the polarization plane (Fig. 5.2B,D,F) is observed. Whether this remarkable resemblance between the distribution is also reproduced by the semi-classical model for the strong-field ion emission is investigated in Fig. 5.3. The Figure shows the angular proton distributions observed experimentally (Fig. 5.3A,B,C) and produced by the simulation code (Fig. 5.3D,E,F). While the theoretically predicted distributions are slightly wider than the experimental ones, the overall qualitative agreement between them is still acceptable. The width of the angular distribution in the simulation is mostly determined by the initial distribution of protons. Since the ionization of the surface (described by the ADK rate) is less nonlinear than the generation law for the protons, the proton trajectories point in good approximation along the radial direction of the nanoparticle. This effect was shown in Ref. [49], where the same model was used. This means that the protons' angular distribution does not significantly change as they leave the nanoparticle, and their initial distribution gets directly mapped onto the final angular distribution. Consequently, an imperfect theoretical description of the proton generation process will cause the experimental and the simulated angular distributions to deviate from each other.

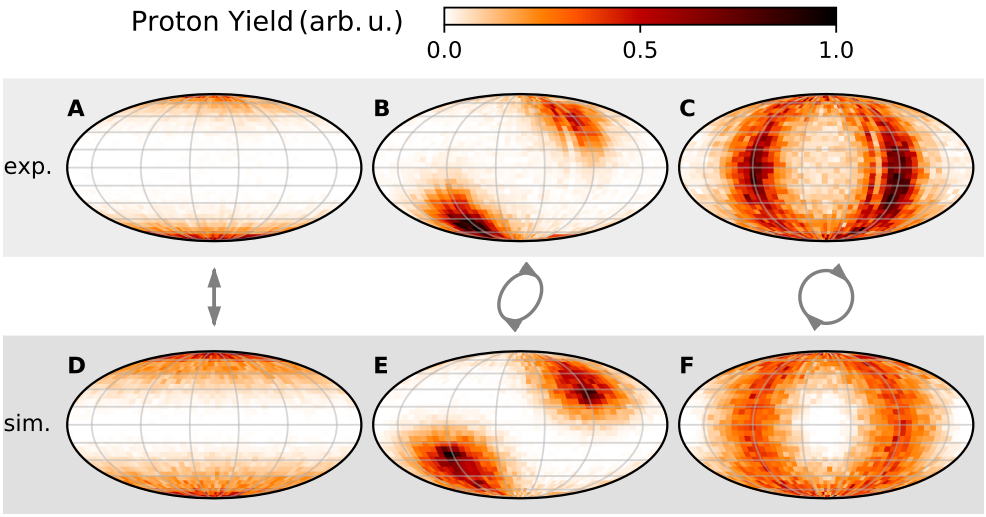

Figure 5.3: Comparison between experimental data (top row) and simulation results (bottom row). **A-C:** Angular distribution of the proton yield from 300 nm silica particles shown in the Mollweide projection [129]. The experimental data were obtained from the same measurements as the data in Fig. 5.2. **D-F:** Corresponding simulation results. Details can be found in the text. Figure taken from Ref. [50].

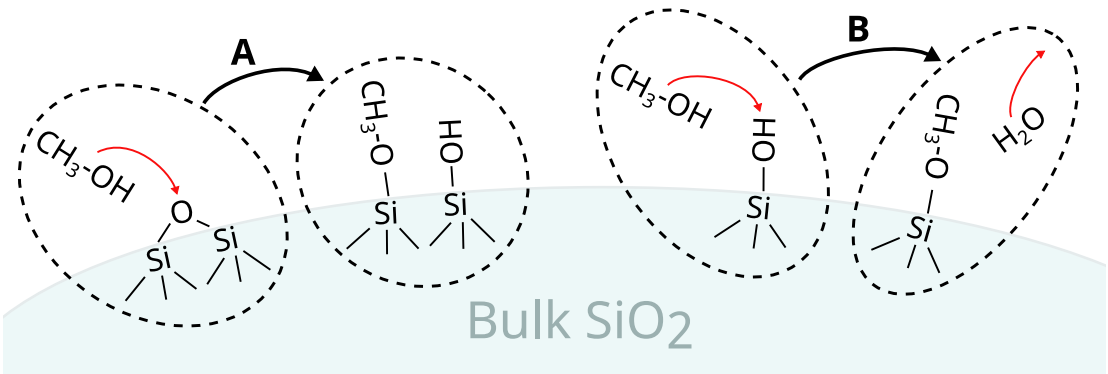

Figure 5.4: Reactions for the formation of alkoxy groups at the silica-methanol interface. The arrows A and B indicate reactions (5.1) and (5.2) of the main text, which describe the formation of a methoxy group from methanol and a siloxane (Si-O-Si) or a silanol group (Si-O-H), respectively.

The surface composition of silica particles

For a better understanding of the proton origin, the surface composition of the silica particles in our experiment is investigated in the following. This is achieved by comparing different solvents and analyzing their impact on the ion time-flight-histograms. Here we used $d = 300\,\mathrm{nm}$ silica nanoparticles, which were aerosolized from dispersions of pure ethanol, methanol, or fully deuterated methanol (methanol-d4). The microscopic details of the interface between silica (nanoparticles) and liquid-phase alcohols are well-understood [130–132]: Assuming a clean and dry silica surface that is only covered with silanol (Si-OH) and siloxane (Si-O-Si) initially, the addition of alcohols will cause the formation of covalent alkoxy bonds with the surface. Björklund and Kocherbitov [91] suggest the following reactions for this process:

$$\mathrm{ROH + Si\text{-}O\text{-}Si \rightarrow RO\text{-}Si + Si\text{-}OH} \tag{5.1}$$

$$\mathrm{ROH + Si\text{-}OH \rightarrow RO\text{-}Si + H_2O} \tag{5.2}$$

Here, the symbol "R" denotes the carbon chain part of the alcohol. The first case describes the reaction of an alcohol molecule with siloxane producing an alkoxy group together with a silanol group on the surface. In the second case, the alcohol reacts with a silanol group to form an alkoxy group, which leads to the production of free water molecules. To give an example, both reactions are depicted in Fig. 5.4 for methanol at the silica surface. The authors of Ref. [91] have furthermore measured the surface densities of alkoxy and silanol groups for silica (MCM-141) nanoparticles dispersed in different alcohols by thermal gravimetric analysis [133]. For ethanol, they found a value of 0.5 ethoxy groups and 2.2 OH groups per nm^2 on the silica surface. This relatively high density of OH groups makes the silica surface polar. For silica nanoparticles dispersed in an alcohol, the polarity gives rise to the formation of a physisorbed layer of alcohol molecules, which is bound to the silanol groups via hydrogen bonds [134, 135].

In the reaction nanoscopy experiments in this thesis, all aerosols were generated from a nanoparticle suspension in water or alcohol. The initially wet aerosol was sent through a drying stage and the vacuum of the nanoscope. The drying stage, however, is not capable of completely removing all solvent molecules from the aerosol, which is confirmed by the presence of ions from gas-phase (small channeltron signal) solvent molecules in the time-of-flight spectra. It is thus expected that the physisorbed layer is removed from the silica surface to a certain but unknown extent. Under ambient pressure, temperatures above 100°C are required for the complete removal of physisorbed alcohols [91]. The same can be achieved by prolonged exposure to vacuum at ambient temperature [130]. It is not clear, however, if, in the case of the reaction nanoscope, the brief period from a nanoparticle entering the aerodynamic lens to the interaction region of about 1 ms is long enough for significant evaporation.

To experimentally clarify the contribution of physisorbed alcohol molecules to typical reaction nanoscopy spectra, we replaced the original solvent of the 300 nm silica particles (ethanol) with methanol and fully deuterated methanol-d4, respectively. The solvent exchange without a calcination step is expected to largely leave the chemisorbed layer

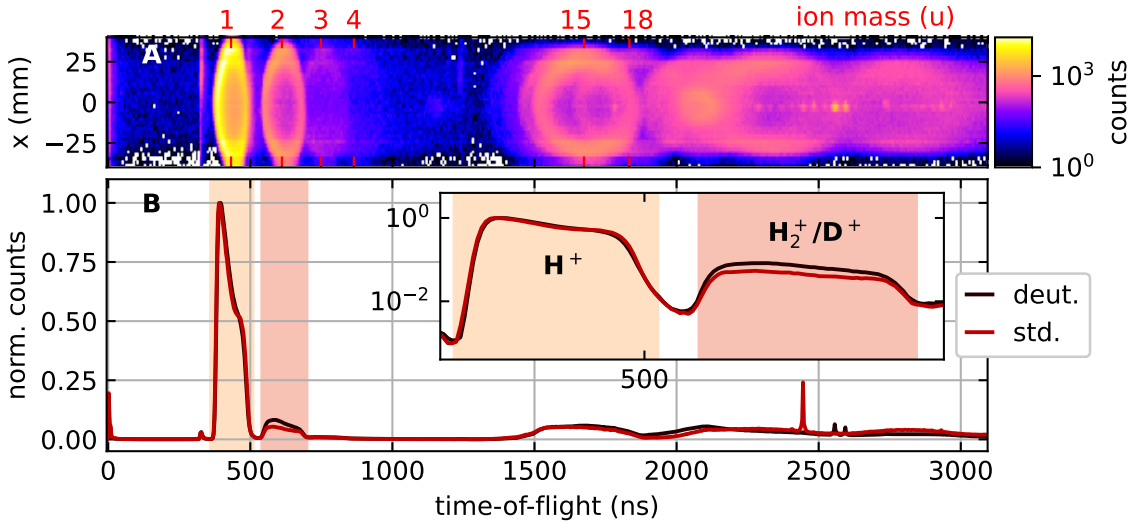

Figure 5.5: Solvent dependent results for 300 nm silica particles ionized by circularly polarized laser pulses. **A:** Time-of-flight vs. position spectrum for a reaction nanoscopy measurement with 300 nm silica nanoparticles dispersed in methanol-d4 (fully deuterated). **B:** Comparison of the time-of-flight histograms for particles dispersed in standard methanol (std.) and methanol-d4 (deut.). The inset shows a zoom-in to the mass peaks of $m = 1\,\mathrm{u}$ (H^+) and $m = 2\,\mathrm{u}$ (H_2^+ and D^+) on a logarithmic scale. Figure taken from Ref. [50].

unchanged [91]. A significant amount of deuterons emitted from the fully deuterated sample would thus indicate a large contribution of ions generated from physisorbed solvent molecules. A dominance of protons despite the methanol-d4 solvent would mean that the solvent largely evaporates before a particle reaches the interaction point, and that the ion origin is the chemisorbed layer on the particle surface. For the measurement with the fully deuterated solvent, the position-resolved time-of-flight histogram filtered on large channeltron signals is shown in Fig. 5.5A. By far the most abundant ion in the histogram is the proton at a mass of 1 u. The dominance of the proton peak over the $m = 2\,\mathrm{u}$ peak (deuterons and H_2^+) alone is already a strong indication that the solvent molecules play a minor role in the emission from the nanoparticle surface. For a more quantitative assessment, we compare the time-of-flight histograms of the nanoparticle sample with the fully deuterated solvent to the histogram for the same nanoparticles in standard methanol. The data is shown in Fig. 5.5B. For both samples, the only ion contributing to the mass-1 peak is the proton. For the mass-2 peak in the time-of-flight histogram, however, H_2^+, as well as D^+, are possible candidates. From the histograms, we extract the ratios between mass-2 counts n_2 and mass-1 n_1 counts. For the standard methanol sample, we obtain:

$$\frac{n_2}{n_1} = \frac{n_{H_2^+}}{n_p}. \tag{5.3}$$

For the deuterated sample, the counts are denoted by n_2^d and n_1^d, respectively, and are

given by:

$$\frac{n_2^d}{n_1^d} = \frac{n_{H_2^+}^d + n_{D^+}^d}{n_p^d} = \frac{n_{H_2^+}^d}{n_p^d} + \frac{n_{D^+}^d}{n_p^d}. \tag{5.4}$$

Assuming that the ratio between H_2^+ and protons is the same for both measurements

$$\frac{n_{H_2^+}^d}{n_p^d} = \frac{n_{H_2^+}}{n_p}, \tag{5.5}$$

we can solve for the ratio between deuterons and protons and find a value of $\frac{n_{D^+}^d}{n_p^d} = 0.04$. In other words, despite the use of a fully deuterated solvent (99.6 % purity), we only detect one deuteron for every 25 protons. These findings clearly show that the contribution of ions generated from physisorbed solvent molecules to reaction nanoscopy spectra is mostly negligible. A similar conclusion can be drawn from the results presented in Ref. [127], where water and D_2O were used as solvents, and a strong proton signal remained even for the D_2O case. While the authors do find a mass-2 signal comparable in strength to the mass-1 counts, this is likely due to the absence of a dryer in their setup resulting in a higher coverage with physisorbed molecules on the nanoparticle (or nanoparticle cluster) surface.

Expected, detected, and detectable ion fragments

Based on the understanding of the surface composition of nanoparticles aerosolized from an alcoholic solution, a certain contribution of hydrocarbon fragments from the chemisorbed alkoxy groups to the ion histograms is expected. Indeed, the methyl ion CH_3^+ (mass 15 u, Fig. 5.5A) is one of the most abundant ion species in the reaction nanoscopy histograms. In principle, a comparison to the CD_3^+ ion (mass 18 u) in analogy to the proton vs. deuteron comparison presented above could be carried out. Qualitatively, much less CD_3^+ compared to CH_3^+ is observed. A quantitative analysis, however, is not possible due to the overlap between the spectra of ions of similar masses. As shown in Fig. 5.5A, this overlap even prevents the identification of ion species at masses higher than 18 u. Fragments like the ethyl ion and the silicon ion Si^+, for instance, are expected to contribute in the corresponding time-of-flight range. Due to the high coverage of the silica surface with silanol groups, an ion that could be expected but was never observed in a reaction nanoscopy experiment with silica nanoparticles is the OH^+ ion ($m = 17$ u). This observation, or the lack thereof, is an indication that the Si-O bonds on the silica surface stay intact and that only the remaining part of the surface groups are emitted. While further investigations on this matter are required, the assumption is compatible with the reaction nanoscopy data, i.e., the emission of protons and alkyl groups.

Ion energies

Identifying ions of different masses and the ability to measure their kinetic energies allows for testing the limits of the model used above. Since, in the model, the charge on the nanoparticle surface is static, and the generated ions do not interact with each other, their final kinetic energy is simply given by the initial potential energy. Consequently, the measured ion energy should only depend on the charge of an ion but not on its mass. This, however, is not observed experimentally as illustrated by Fig. 5.6 where data for protons and methyl ions emitted from the nanoparticle surface are shown. While the momentum histograms for both ions (Fig. 5.6A,B) have a similar shape, their mean energies differ by up to 20% (see Fig. 5.6C). In all cases, the proton energy is found to be higher than the CH_3^+ energy, independent of the laser polarization and the laser intensity, and the difference in energy between H^+ and CH_3^+ is generally lowest at a low laser intensity. For both ions and all three polarization states displayed in Fig. 5.6C, the energy increases approximately linearly with intensity and levels off at the highest measured intensities.

Given that the model predicts mass-independent ion energies, the question arises whether the difference in energy is a measurement artifact or whether monovalent ions of different masses generated from single nanoparticles can indeed differ in their mean energies. A lower energy of the CH_3^+ ion could, for example, be explained by fragmentation at high intensities. This would reduce the CH_3^+ signal from the high-intensity regions of the laser focus and thereby shift the mean of the energy distribution toward a smaller value.

Such focal volume-related effects can be tested by analyzing coincident events of H^+ and CH_3^+. As derived in Section 3.3.1, typically more than 99% of all nanoparticle ionization events involve exactly one nanoparticle. This means that the vast majority of ions detected in coincidence with each other originate from the surface of the same nanoparticle. Therefore, coincident ions are well-suited for reasoning about effects related to the intensity distribution within the focal volume. In order to answer the question of whether the mass-dependence of the ion energy is focal volume related, we show the two-particle energy histogram in Fig. 5.7A for the data of Fig. 5.6, which was acquired with linearly polarized pulses. We find for 82% of all H^+ - CH_3^+ coincidences that the energy of the CH_3^+ ion is lower than the H^+ energy. Similar values were found for the other polarization states (see Ref. [50], supplementary information). This means that difference in ion energy is observable even for ions emitted from the same nanoparticle and is thus unrelated to focal volume averaging.

Furthermore, a covariance analysis on the coincident ion data was carried out. Such a statistical approach to multi-ion events has proven to be very effective when the probability of generating more than two ions within the regions of interest along the time-of-flight axis is non-negligible [136]. In Fig. 5.7B, the covariance map for the H^+ and CH_3^+ energy is displayed. For every pair of energy bins, it is defined in the same way as the ordinary covariance of two random variables:

$$\mathrm{Cov}(X_i, Y_j) = \langle X_i Y_j \rangle - \langle X_i \rangle \langle Y_j \rangle, \tag{5.6}$$

where in our case X and Y are the kinetic energy of H^+ and the CH_3^+ and i, j are the

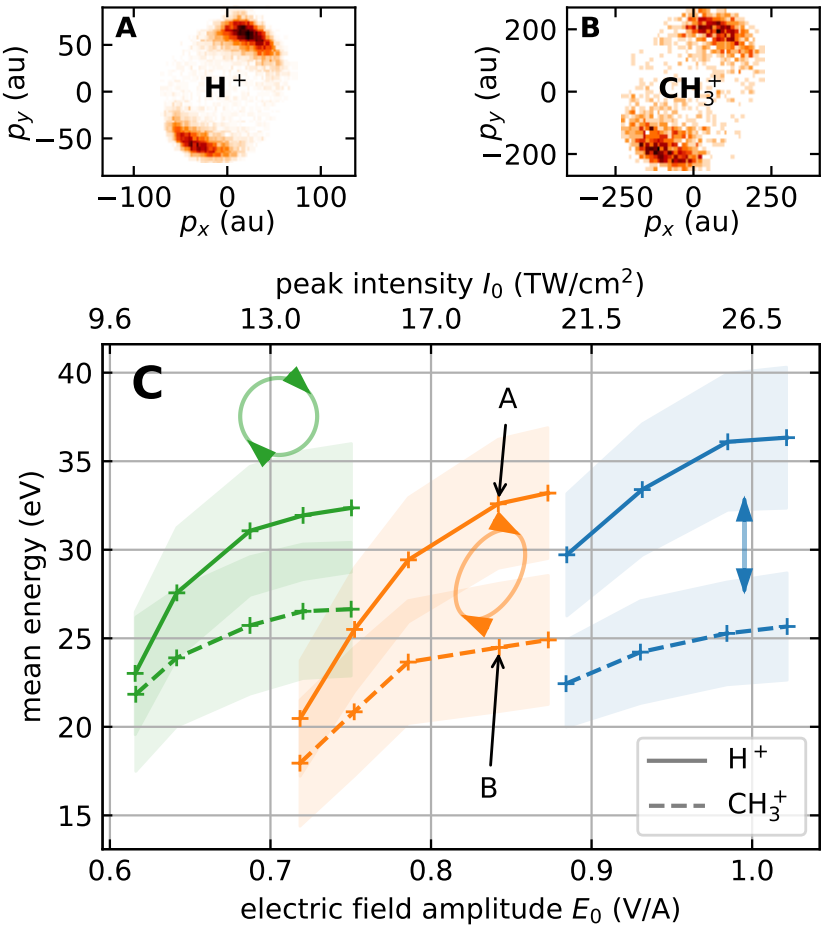

Figure 5.6: Ion energy scaling with electric field amplitude for different polarizations. **A,B:** Polarization-plane momentum spectra for H^+ (A) and CH_3^+ (B) ions generated on 300 nm silica nanoparticles taken at the field strength and polarization indicated by the arrows in panel C. **C:** Mean energies for H^+ (solid lines) and CH_3^+ (dashed lines) for a range of field strengths and different polarization states (corresponding to $\lambda/4$-plate angles 45°, 30°, 0°, from left to right). The shaded regions represent the width (standard deviation) of the ion energy distribution. The conversion to peak intensity I_0 (labels at upper x-axis) is carried out without cycle-averaging: $I_0 = c\varepsilon_0|E_0|^2$. Figure taken from Ref. [50].

indices of the corresponding energy bins. The angle brackets denote averaging over all samples, i.e., all detected coincidences. Positive or negative values in the covariance map indicate a positive or negative correlation between two ion energies, respectively. We find a positive correlation along a line underneath and parallel to the diagonal of the covariance map and a negative correlation everywhere else. The implications will be discussed in the following section.

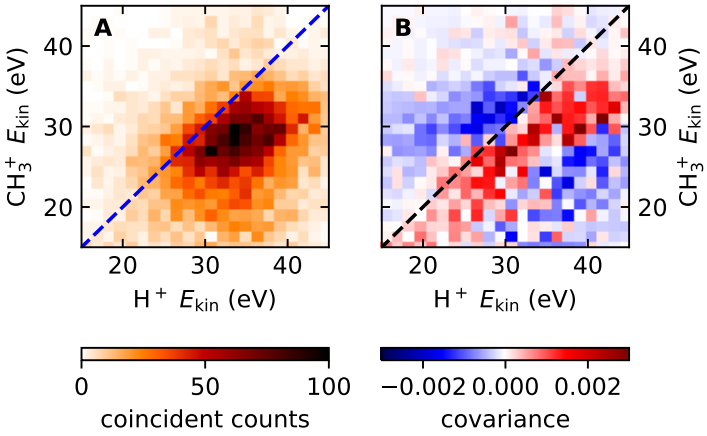

Figure 5.7: Coincidence and covariance histograms of H^+ and CH_3^+ ions generated by the same laser pulse. **A:** Histogram for the energies of H^+ and CH_3^+ ions detected in coincidence. **B:** Covariance map generated from the same data as defined in the text. The dashed line indicates $y = x$, i.e., equal energies for both ions. Figure taken from Ref. [50].

5.5 Discussion

The results presented in the previous section are a demonstration that in reaction nanoscopy experiments with silica nanoparticles, the close relationship between the angular distribution of the laser-generated ions and the local field enhancement on the nanoparticle surface is still observed at a wavelength of 2 μm and even for arbitrarily elliptical polarization. The work of Rupp et al. [47] has demonstrated that the mapping between local near-field and final ion distribution is not trivial for the case of a general surface charge density on the nanoparticle surface. From the simulations carried out here, we could identify the two main conditions such that the angular ion distribution shows a high correlation with the local near-field. The first condition is a monotonically increasing ion generation probability with near-field amplitude. While this may seem trivial regarding the nonlinear generation law introduced in the theory section, it can be violated due to the saturation of the ionization and the depletion of the neutral state (see Section 2.3 or Ref. [59], for example). The second condition is a radial repulsion of the generated ions from the surface of the nanoparticle. This condition is met if the local charge density around the birthplace of an ion is in good approximation symmetrical such that all tangential forces cancel out,

leading to a radial trajectory. In our model, this is fulfilled since the generation of surface charges in the model requires less field strength than the generation of free ions. The surface charge is thus distributed over larger areas than the birth positions of the free ions. As a consequence, most ions are emitted perpendicularly to the nanoparticle surface. Only the ions generated far away from the field enhancement maxima will be emitted under a small angle to the radial vector (see also Ref. [49]).

The physical background behind the effective surface charge used in our model is the ionization of the nanoparticle surface. The more electrons leave the surroundings of the nanoparticle, the more positively charged the nanoparticle will become, and the more energy the emitted ions will have. Thus, the electron yield is directly related to the effective surface charge of the nanoparticle, which, in turn, determines the final energy. Due to this connection, a comparison between the intensity-dependent ion energies in Fig. 5.6 and a previous study on strong-field *electron* emission from silica nanoparticles is carried out. Süßmann et al. [42] found a linear relationship between the laser intensity and the electron yield. In other words, they found a linear increase of the effective surface charge with laser intensity. This finding is compatible with the ion energy scaling we observed in the low-intensity range. The roll-off of the ion energies at higher intensities observed in Fig. 5.6, however, is to date not yet fully understood and will require further investigation in the future.

Since the ion energy is dominated by the Coulomb repulsion from the nanoparticle surface, it can in principle serve as a probe of the local charge density and the total charge of the nanoparticle. This could allow, for example, the observation of charge redistribution on the nanoparticle surface in pump-probe experiments and thereby provide valuable information about the material properties on the nanometer length scale and femtosecond time scale. For a complete understanding and correct interpretation of such data, however, the different contributions to the final ion energy need to be fully known. The observation of varying mean energies across different ion species proves that the static Coulomb description chosen here is still incomplete. An unaccounted contribution in the model is the initial energy from the dissociation of the molecular bond(s) upon ionization, which led to the production of a certain ion. Since typical dissociation energies of molecules upon dissociative ionization are in the few-eV range [137, 138], such a contribution would be compatible with our measurements. The first step toward modeling this effect was achieved by the results presented above, where the most important molecular adsorbates for ion emission were identified. It was shown that the ion spectra in reaction nanoscopy experiments are in very good approximation dominated by ions originating from covalent bonds with the surface and that the solvent in which the nanoparticles are dispersed plays only a minor role. A second possible contribution to the difference in ion energies is a dynamical effect. As positive ions are emitted from the nanoparticle surface, the total charge on the surface is reduced. This means that the surface charge is reduced for heavier particles with higher inertia, causing them to stay closer to the nanoparticle for a longer time than lighter ones. A consequence of this process may be visible in Fig. 5.5A, where a position-resolved time-of-flight histogram measured with circular polarization is shown. Interestingly, the radius of the circular emission pattern for every ion species decreases with ion mass. The

square of the ring radius is proportional to the energy of a particle: In the constant field of the spectrometer, a particle with zero initial velocity along the time-of-flight axis (i.e., the direction of the field), zero velocity along z and maximum velocity along the field-free x-axis satisfies:

$$\tau \propto \sqrt{\frac{m}{q}}, \tag{5.7}$$

$$p_x = m\frac{y}{\tau} \propto my\sqrt{\frac{q}{m}}, \tag{5.8}$$

$$p_z = 0, \tag{5.9}$$

where q is the charge of the ion, m its mass and τ its time-of-flight. Hence, the kinetic energy does not depend on mass but only the charge and the x-position:

$$E = \frac{p_y^2}{2m} \propto qx^2 \tag{5.10}$$

Given that we have never detected ions with a charge $q > 1e$ (like C^{2+} for instance), we may assume that all ions are monovalent ($q = 1e$), even those that are not uniquely identifiable due to overlapping spectra. In this case, the observation of smaller rings in the position-resolved time-of-flight histogram (Fig. 5.5A) indeed corresponds to a decreasing ion energy with ion mass. The data is therefore compatible with the hypothesis of a mass-dependent effective nanoparticle charge due to the faster emission of light ions like protons or H_2^+ molecular ions. Still, further (pump-probe) experiments are required to fully confirm the different contributions to the fragments' energy.

5.6 Conclusions

In this chapter, it was demonstrated that the model for strong-field ion emission introduced in Chapter 2 and first used for the description of the reaction nanoscopy results presented in Chapter 4, is able to also reproduce the angle-resolved momentum histograms at the longer wavelength of 2 μm and for an arbitrary ellipticity of the laser polarization. Furthermore, the current limitations of the model were discussed. The model is, at this point, not yet suitable for the description of ion energies over large parameter ranges like laser intensity or polarization state. More fundamentally, its underlying assumptions do not allow for a mass dependence of the mean ion energies, which was observed in the experiment and confirmed to be a single-particle effect by a covariance analysis of the coincident ion data. For these reasons, a more elaborate theoretical treatment will be required for a correct description of all ion energies.

As a first step toward this goal, the main origin of the observed ions in reaction nanoscopy was identified. Using silica nanoparticles dispersed in a fully deuterated solvent, it was found that after aerosolization and subsequent injection into the vacuum, their surface is, to a large extent, free of physisorbed solvent molecules. Ions originating

from such adsorbates were shown to only contribute at a level of a few percent to the overall ion yield. The dominant ion sources in reaction nanoscopy are therefore chemisorbed molecules, i.e., functional groups, which are covalently bound to the surface. The acquired reaction nanoscopy data for silica particles in an alcoholic dispersion were found to be compatible with studies where the influence of different alcohols on the silica surface was investigated by means of thermal gravimetric analysis [91]. The reported dominance of silanol groups on the surface with a significantly smaller amount of alkoxy groups is an explanation for the high abundance of H^+ and H_2^+ ions in reaction nanoscopy and also explains the presence of hydrocarbon fragments like CH_3^+.

In conclusion, the results of this chapter have answered the crucial question of the ion origin in reaction nanoscopy experiments. While the data itself is limited to silica nanoparticles, the principle that fragments of chemisorbed molecules dominate the ion spectra should apply to a wide range of nanosurfaces. This insight is a necessary step toward the development of more accurate models and, equally important, for the conception of future reaction nanoscopy experiments.

Chapter 6

Reaction nanoscopy with droplets

This chapter presents the first results of reaction nanoscopy with droplets. Polydisperse propanediol (PDO) droplets were ionized by a 2 μm laser, and the three-dimensional ion momenta were recorded. It was found that the ion emission is governed by the local near-field amplitude on the droplet surface, analogous to the results of reaction nanoscopy with solid nanoparticles. The correlation between the near-field enhancement and the angular distribution of the emitted ions was used to determine the most prominent droplet diameter, and the droplet charge was estimated from the energies of the emitted ions. To isolate droplet-related effects and effects of the molecular surface structure, we compared 1,2-PDO and 1,3-PDO reaction nanoscopy data. It was found that the ionized droplet surface increases the probability of fragment protonation. In addition, the isomer-specific molecular alignment on the surface of the PDO droplets was found to cause an enhanced emission of methyl ions from 1,2-PDO droplets, which was confirmed by density functional theory.

The results presented in this chapter were published here: arXiv:2212.05587 [physics.chem-ph].

6.1 Introduction

One of the ultimate goals of the reaction nanoscopy experiments is the direct observation of catalyzed chemical reactions by probing the reaction products via light-induced ion emission. While nanoparticles are heavily used in wet-chemistry catalysis applications [8], the transfer of these reactions to the ultra-high vacuum environment of the reaction nanoscope has remained challenging. To observe catalytic reactions, sufficient coverage of the surface of a nanoparticle with reactant molecules is required. As demonstrated in the previous chapter, the solvent's evaporation can strongly reduce the surface coverage and lower the signal from potential reaction products.

Despite reaction nanoscopy's sensitivity to single ions, a low rate of reaction product ions means a stronger relative signal of ions from surface ligands or the nanoparticle material itself and thus lowers the signal-to-noise ratio. This is especially problematic for cat-

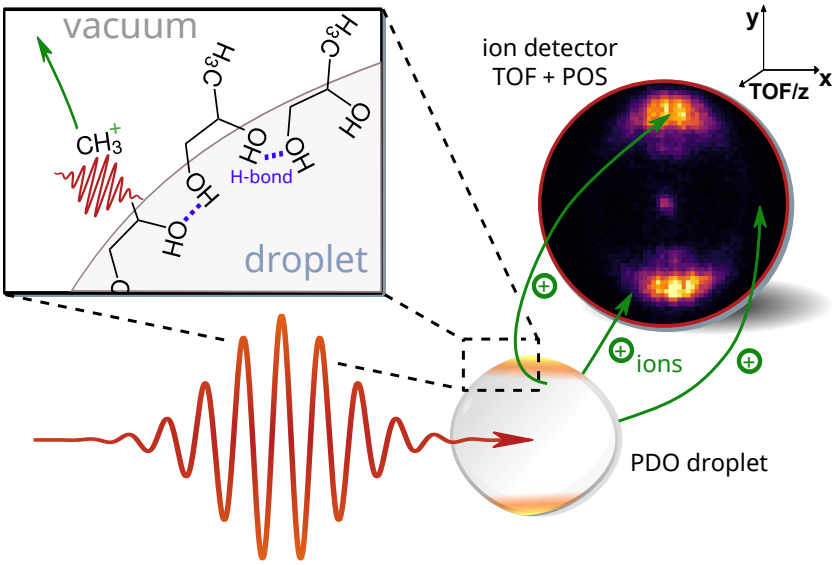

Figure 6.1: Schematic depiction of reaction nanoscopy with droplets of propanediol (PDO). A few-cycle laser pulse ionizes the droplet's surface, and the released ions are detected by a time-of-flight- (TOF) and position- (POS) sensitive detector. The green arrows indicate the ion trajectories. Laser pulses with a duration of 25 fs, a central wavelength of 2 μm, and an intensity of up to 5×10^{13} W/cm^2 were used. The mean droplet diameter was 590 nm (see results). The box on the top-left shows an example of the laser-induced emission of a CH_3^+ ion from a 1,2-PDO droplet.

alytic particle materials, which typically require stabilization by large hydrocarbons [139]. Upon laser ionization, such hydrocarbons fragment via multiple pathways resulting in a broad background in the time-of-flight spectra.

A technically simpler and potentially more feasible alternative to catalyzed reactions on nanoparticle surfaces could be reaction nanoscopy with droplets. Analogous to an enhancement of reaction rates by the presence of a catalyst, chemical reactions on droplets can be accelerated by charging the droplets [13–16, 140]. This has led to investigations into possible industrial applications [17, 18], and is why charged droplets are regarded as potential reactors for prebiotic polymers [19, 141, 142]. However, the primary mechanism behind the reaction rate enhancement on charged droplets is still not fully elucidated. While some researchers suggest that the acceleration of reaction rates is caused by solvent evaporation [143–145], other studies point out the role of the droplet surface itself [140, 146, 147]. The charge on the droplet leads to extreme conditions near the surface, with a strong electric field [148–150], a high degree of molecular concentration and alignment [19, 141, 142, 151, 152] and a high acidity [12, 153, 154]. However, the specific contributions of these effects have not been quantified so far and are still actively investigated [15, 150].

Since experimental methods for the study of charged droplets mostly rely on the complex and hardly controllable process of electrospray ionization [155–157], a distinction between surface effects and evaporation contributions to the mass spectra has so far not been possible. Furthermore, the uncontrolled charging of electrospray-generated droplets gives rise to droplet fission and the generation of progeny droplets when the total charge

approaches the Rayleigh limit[158]:

$$q_R = 8\pi\sqrt{\gamma\varepsilon_0 R^3}, \tag{6.1}$$

where γ is the surface tension, R is the droplet radius, and ε_0 is the vacuum permittivity. The consequence is unknown distributions of both the sizes and the charges of the droplets.

In this chapter, it is demonstrated that reaction nanoscopy can serve as a surface-sensitive method for investigating ion emission from charged droplets with the additional benefit of an in-situ evaluation of the droplet stability and characterization of the most abundant droplet diameter in a polydisperse stream of droplets. For this purpose, aerosolized droplets of PDO were ionized by a strong femtosecond laser pulse, and the three-dimensional momentum vectors of the generated ions were measured with the reaction nanoscope. For this proof-of-principle study, PDO was chosen as a target due to its low vapor pressure and relatively high surface tension, which make it ideal for droplet generation and injection into a vacuum. Apart from its favorable physical properties, it exists in the form 1,2-PDO and 1,3-PDO, which allows an investigation of isomer-related effects.

It will be shown that the comparison of reaction nanoscopy data for both isomers allows the separation into effects related to the droplet environment in general and furthermore reveals the isomer-related effect of enhanced production of CH_3^+ ion from 1,2-PDO droplets. Using density functional theory calculations, this effect is attributed to the isomer-specific molecular alignment on the droplet surface.

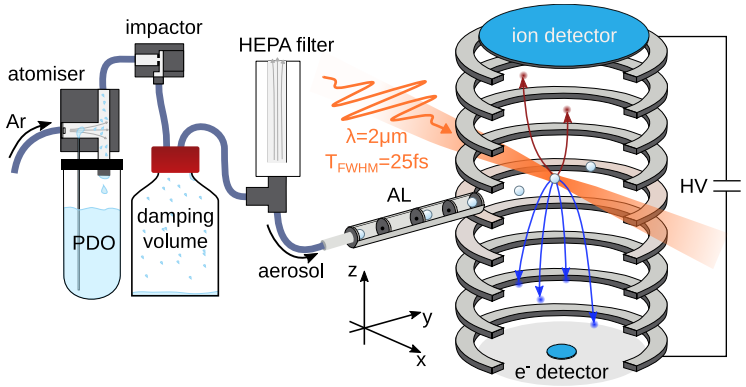

Figure 6.2: Droplet source and reaction nanoscope. The propanediol (PDO) droplet source consisted of an atomizer operated with argon (Ar), an impactor, a damping volume of 1 l, and a high-efficiency particulate air (HEPA) filter. An aerodynamic lens (AL) was used to inject a collimated aerosol stream into the reaction nanoscope, where the droplets were ionized in the laser's focus. The generated electrons and ions were directed to the corresponding detectors by a homogeneous electric field generated by a high voltage (HV).

6.2 Experimental

As in the previous chapters, the experimental setup will only be briefly described here. For more details, the reader is referred to the dedicated experimental chapter (Chapter 3).

6.2.1 Laser system

For the droplet experiments, the same OPCPA laser system as in Chapter 5 was used (see also Ref. [81]). It produced laser pulses with a central wavelength of 2 μm, a maximum pulse energy of 100 μJ, a pulse duration of 25 fs, and a repetition rate of 100 kHz. The pulse energy was controlled with a broadband half-wave plate in combination with a wire-grid polarizer. The temporal compression of the pulses was optimized by maximizing the ion count rate in the reaction nanoscope while tuning the pulse dispersion with a pair of fused silica wedges. The pulses were focused with a silver mirror (f = 75 mm), resulting in a peak of up to 5×10^{13} W/cm^2 in the laser focus, i.e., the interaction region of the nanoscope.

6.2.2 Reaction nanoscopy with droplets

The droplet source and the reaction nanoscope are shown in Fig. 6.2. The droplet setup is very similar to the configuration for solid nanoparticles. For droplet generation, the pure liquid of 1,2-PDO (Thermo Scientific, +99.5 %) or 1,3-PDO (Thermo Scientific, 99 %) was aerosolized by the same atomizer as before (TSI inc., model 3076). The aerosol was then sent through an impactor to remove large droplets from the stream, and the accumulating liquid at the impactor plate was collected by a subsequent reservoir, which also served as a dampener for flow instabilities (see the atomizer manual). The remaining components of the source were identical to the case of solid nanoparticles. The reaction nanoscope itself was operated at almost identical conditions as well (same voltages and similar laser intensities). From the reaction nanoscopy data, the most frequent droplet size (at the interaction point) in the aerosol stream was determined as (590±50) nm (see further details below).

6.3 Theoretical description of the droplet surface

For the interpretation of the isomer-specific reaction nanoscopy data from the PDO droplets, a microscopic description of the droplet surface on a molecular level was needed. Arijit Majumdar from the group of Prof. Dr. Matthias Ihme at Stanford University carried out density functional theory (DFT) calculations for this purpose. Since the computation of the entire droplet is not feasible at this level of theory, a model system of six layers of molecules was used. Periodic boundary conditions were chosen in the directions perpendicular to the surface normal. The curvature of the droplet surface is neglected due to the large droplet size compared to the size of the individual molecules. Such a system of layers has two boundaries with the vacuum, while a droplet has only one interface with the vacuum. To resolve this ambiguity and make the identification of the vacuum interface unique, the three bottom layers in the simulation are rotated by 180° with respect to the top three layers. The minimum energy configuration for this arrangement was calculated for both, 1,2-PDO and 1,3-PDO. The results are displayed in Fig. 6.3

The calculations were carried out with the Vienna ab initio simulation package (VASP) [159, 160], a code using the plane-wave DFT formulation [161]. The exchange correlation term

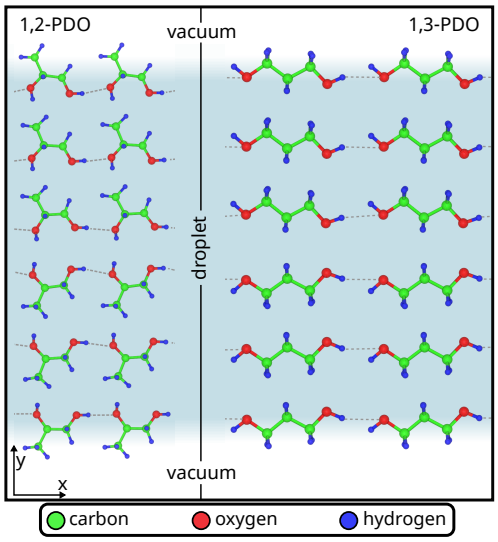

Figure 6.3: Simulation geometry for 1,2-PDO (left) and 1,3-PDO (right). The surface normal is along the y-axis. Periodic boundary conditions were applied along x and z. The dotted lines represent hydrogen bonds (manually inserted).

is described with the Perdew-Burke-Ernzerhof (PBE) functional [162], and the interaction between the atomic cores and the electrons is handled via the Projector Augmented Wave (PAW) method [163]. The size of the simulation is $\Delta x \times \Delta y \times \Delta z$ =8Å×90Å×12Å. The surface normal is along the y-coordinate. The boundaries in x and z are periodic. In order to avoid effects of periodicity in the direction of the surface normal, Δy was chosen sufficiently large. The Brillouin zone is sampled with a Γ-centered grid with a size of 7×1×7 grid points. The convergence criterion for the energy minimization was set to 10^{-6} eV. The final configurations are found with a formation enthalpy for the slab from isolated gaseous molecules of -0.70 eV for 1,2-PDO and -1.35 eV for 1,3-PDO to be energetically stable.

6.4 Results

6.4.1 Near-field driven ion emission

A spherical droplet interacts in the same way with (infrared) light as a solid sphere. For a spherical object in a vacuum, its diameter and the refractive index will define the properties of the near-field [40]. The refractive index for propanediol at a wavelength of 2 μm was obtained by an extrapolation from published refractive index data [164] using Cauchy's equation [165]. A value of $n(\lambda = 2\,\mu\text{m}) = 1.43$ was found. We expect the extrapolation to be accurate with $\Delta n = \pm 0.03$, which corresponds to a relative uncertainty of $\Delta n/n \approx 2\%$. The value of Δn was generously estimated from available data for the refractive index of ethylene glycol (EG) at $\lambda = 2\,\mu$m [166], $n_{\text{EG}} = 1.416 \pm 0.001$, which has very similar physical properties to PDO. The uncertainty in the refractive index is negligible compared to the uncertainty of the estimate of the droplet diameter of $d = (590 \pm 50)$ nm. A detailed

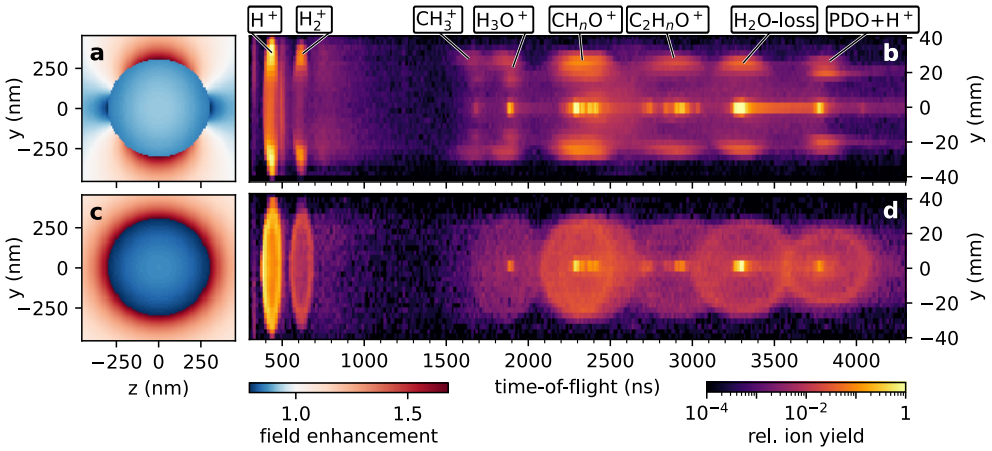

Figure 6.4: Near-field distributions and ion emission histograms for 1,3-propanediol droplets. **a:** Near-field enhancement around a propanediol droplet placed at the origin with a diameter of 590 nm for linearly polarized (along y) light with a wavelength of 2 μm in the plane of $x = 0$. The data was obtained from the Mie solution of Maxwell's equations.[40] **b:** Measured ion yield with linear laser polarization and an instantaneous peak intensity of approx. $5{\times}10^{13}\,\mathrm{W/cm^2}$ as a function of time-of-flight and y. Counts at large values of $|y|$ are ions emitted from droplets. Counts close to $y = 0$ correspond to ions generated from single propanediol molecules. **c,d:** The corresponding data for circularly polarized light at an instantaneous peak intensity of approx. $3{\times}10^{13}\,\mathrm{W/cm^2}$. For the coordinate system, cf. Fig. 6.1.

explanation of the size estimate will be given further below.

Using a refractive index of $n = 1.43$ and a droplet diameter of $d = 590\,\mathrm{nm}$, the field enhancement in the plane parallel to the laser polarization and through the center of the droplet was calculated from the Mie solution of Maxwell's equations [40] taking into account the first 15 orders of the expansion. The results for linear and circular polarization are shown in Fig. 6.4a and c. Since the refractive index of PDO is very similar to the refractive index of silica ($n(2\,\mu\mathrm{m}) = 1.438$ [167]), the resulting field enhancement distribution and amplitude for the PDO droplets are almost identical to silica nanoparticles of the same size. However, the question of whether the similarity in the near-field distributions translates into similar results for the ion emission is not a priori clear. To investigate this, the position-resolved time-of-flight histograms for reaction nanoscopy experiments with 1,3-PDO droplets are shown for the corresponding polarizations in Fig. 6.4. The plane, which is spanned by the y-direction and the time-of-flight axis, is parallel to the polarization plane of the laser. Therefore, for every ion species, it is expected that the pattern in the histogram is closely related to the corresponding field enhancement. This is indeed found for all ions with large momenta, i.e., for linear polarization, those ions with large values of $|y|$, and the ions forming the ring-like patterns for the case of circular polarization.

This near-field driven emission of the ions will be used below for the size determination of the droplets. Unlike typical data for silica nanoparticles, overall, the time-of-flight spectra are clean enough such that a relatively large number of fragments can be identified. As indicated by the labels above Fig. 6.4b, the only ambiguous groups of fragments are CH_nO^+ and $C_2H_nO^+$ where the spectra for the different proton numbers overlap. All other

fragments will be discussed further below.

6.5 Intensity dependence of the ion emission angle

Even though the polarization dependence of observed ion distributions already provides good evidence for a strong correlation between the near-field distribution and the angular ion distributions, this conclusion is further consolidated by the intensity dependence of the observed signal. The dependence is best visualized by the projection of the ion momenta onto the plane of polarization and propagation. The corresponding proton momentum histograms for different laser intensities are shown in the middle row of Fig. 6.5, and the angular distribution is shown in the bottom row. There, the angle α is defined as the angle between the ion emission direction and the laser propagation direction ($\alpha = \arctan2(|p_y|, p_x)$). At the lowest intensity of $2.2\times10^{13}\,\mathrm{W/cm^2}$, the angular distribution (panel h) peaks at $\alpha = 0$, and the majority of the ions are emitted forwards along the propagation direction.

This seems similar to the dominance of the ion signal from nanoparticle clusters at low intensity reported in Chapter 4 and Ref. [52]. However, it can easily be shown that clusters of droplets are not energetically favorable and can thus not be responsible for the observation. The surface energy [168] of a cluster E_C of two droplets is equal to twice the individual surface energies:

$$E_C = 2 \cdot 4\pi\gamma R_1^2, \tag{6.2}$$

where γ is the surface tension and R_1 the radius of the two droplets. If both droplets merge, their volumes add up, which leads to a new radius $R_2 = \sqrt[3]{2}R_1$. Therefore, the surface energy of the single droplet E_S with the new radius is given by:

$$E_S = 4\pi\gamma R_2^2 = 2^{\frac{2}{3}} \cdot 4\pi\gamma R_1^2 < E_C. \tag{6.3}$$

The inequality $E_S < E_C$ shows that merging two droplets into a larger one is energetically favorable over a cluster of two droplets. This result is simply a consequence of the sphere being the shape with the smallest surface area for a given volume [169] and thus minimizes surface tension.

With the exclusion of clusters, the only possible reason for the observation of ions emitted in the forward direction is large droplets where the propagation of the laser light causes nanofocusing [37]. Some contribution of ions emitted from large droplets is expected due to the polydispersity of the atomizer (see, for example, Ref. [170]). As shown in Fig. 6.5a-c, the nanofocusing effect leads to large field enhancement factors (>2.5) for droplets with a size on the order of the wavelength. Combined with nonlinear scaling of the ion yield with laser intensity, the low-intensity ion data is dominated by the emission from large droplets, even if their relative abundance in the droplet stream is low. In agreement with this hypothesis, the data obtained at the highest intensity of $4\times10^{13}\,\mathrm{W/cm^2}$ (Fig. 6.5g,k) shows hardly any contribution for small values of α, as indicated by the red ellipse in panel k. This means that the overall contribution to the ion yield of large droplets

with a propagation parameter $\rho = \pi d/\lambda \gg 1$ is negligible. More importantly, we observed that above a threshold intensity of approximately $3{\times}10^{13}\,\mathrm{W/cm^2}$, the angular distribution of ions does not significantly change anymore. We interpret this finding such that above the threshold intensity, all droplet sizes present in the aerosol stream are ionized by the laser. This stability of the angular distribution of the emitted ions for sufficiently high intensities will be used in the following for the size characterization of the most abundant droplets in the aerosol stream.

In short, the observation of intensity-dependent proton distributions is consistent with a droplet size selectivity from the dependence of the maximum field enhancement factor on the droplet size. The intensity-dependence of the proton momentum distributions from PDO droplets further confirms the close relationship between the angular distributions of the local near-field and the emitted ions.

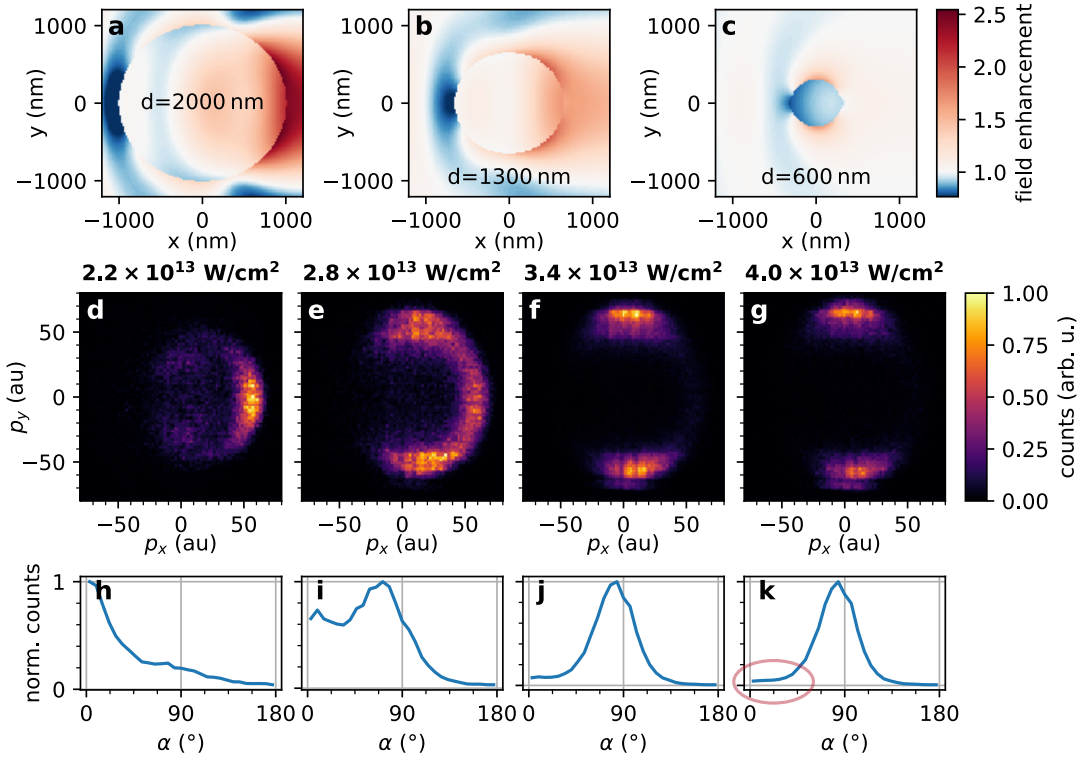

Figure 6.5: Intensity dependence of the proton emission. The laser propagation direction is from left to right along the x-coordinate. The polarization is linear along the y-coordinate. The top row shows the field enhancement in the plane $z = 0$ for propanediol droplets with diameters of 2000 nm (panel a), 1300 nm (panel b), and 600 nm (panel c), respectively, calculated from the Mie solution of Maxwell's equations. The middle row (panels d-g) shows projections of the three-dimensional proton momentum distribution onto the plane of propagation (p_x) and polarization (p_y) for different intensities. The angular distributions in the bottom row (panels h-k) are generated from the histograms in the middle row (same data per column). Here, the angle α is defined as $\alpha = \mathrm{arctan2}(|p_y|, p_x)$. The red ellipse in panel k highlights the small contribution of forward emitted protons ($\alpha = 0°$) at high intensities.

6.6 Droplet size characterization

The broad distribution of droplet sizes generated by the atomizer is altered as the aerosol is transported toward the interaction region: The impactor and the aerodynamic lens mechanically remove specific droplet sizes from the stream, and the vacuum of the nanoscope causes evaporation and shrinking of the injected droplets. Since the initial size distribution and the exact impact of all these mechanisms are unknown, an in-situ characterization of the droplet size is desirable. While a complete retrieval of the size distribution is out of reach with our current method, we can use the size-dependent angle of maximum near-field enhancement for determining the most frequent droplet diameter in the stream, i.e., the peak of the size distribution. As shown in the previous section, the angle between the laser polarization and the point of maximum field enhancement on the droplet surface depends on the droplet size. This angle shall be denoted by φ, as indicated in Fig. 6.6c. Assuming, based on the results above, that the angle-resolved ion yield is a monotonous map of the field enhancement, it follows that the peak of the angular ion distribution coincides with the angle for the maximum field enhancement: $\varphi \approx \alpha$. The angle-resolved ion momentum spectra can thus be used to estimate the most probable droplet size. In order to obtain the mapping between the angle of maximum near-field (or mean ion emission angle) and the droplet size, we calculated the Mie solution of Maxwell's equation for a range of droplet sizes and found the angle of maximum field enhancement $\varphi(d)$ ($\approx\alpha(d)$) by numerical optimization. The inverse function $d(\alpha)$ is shown in Fig. 6.6c. The shaded region along the α-axis shows the range of average ion emission angles obtained from ions of different masses. The corresponding range of droplet diameters is centered around a droplet diameter of 590 nm and about $\pm$50 nm wide. It is important to note that the spread of $\pm$50 nm is not the width of the size distribution but should be regarded as the error of the estimate of the most probable droplet size:

$$\arg\max_d p(d) = (590 \pm 50)\,\mathrm{nm}, \tag{6.4}$$

where $p(d)$ denotes the unknown size distribution and d the droplet diameter.

This approach to the characterization of droplet sizes relies on the propagation-induced tilt of the near-field enhancement along the propagation direction and does, therefore, not apply to arbitrarily small particles or propagation parameters $\rho = \pi d/\lambda \ll 1$, respectively. In this limit, the Rayleigh scattering limit [171], the response of the droplet is dipolar, and the emission angle is $\alpha = 90°$, independent of the size. A similar problem arises in the limit of large droplets, i.e., $\rho \gg 1$. As shown in Fig. 6.5a, for $d = \lambda$, nanofocusing is observed, which leads to an ion emission angle of $\alpha = 0$ for a large range of diameters, making an ion-based size estimate impossible. The ideal parameter space for the method presented here is thus $\rho \approx 1$, which corresponds to $d \approx \lambda/\pi \approx 600$ nm. This is consistent with the calculated mapping function in Fig. 6.6c.

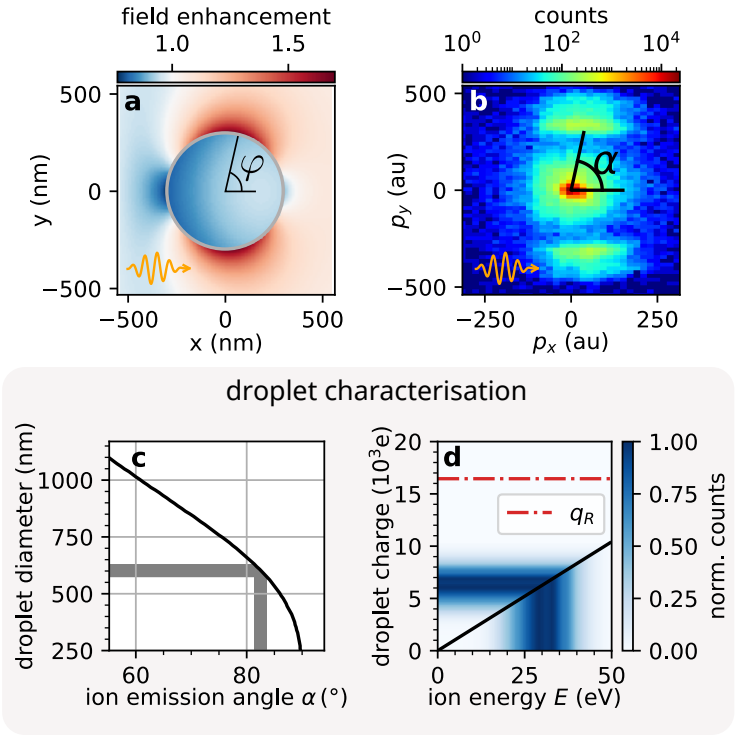

Figure 6.6: Determination of the droplet size and charge for a 1,2-propanediol measurement at a peak intensity of 4.7×10^{13} W/cm^2 and linear laser polarization. **a:** Sketch of a droplet with a diameter of 600 nm. The field enhancement is indicated by the color map. The angle φ is the angle of maximum field enhancement in the propagation-polarization plane (x-y plane). **b:** Projection of the measured ion momenta for protonated 1,2-propanediol (m =77 u) ions onto the plane of propagation (p_x) and polarization (p_y) of the laser. The units are atomic units (au). The angle α is the mean emission angle of the ions in the p_x-p_y plane. **c:** The relation between the droplet diameter d and the mean ion emission angle (solid line) using $\varphi \approx \alpha$ (see text for justification). The shaded area indicates the variation of the mean emission angle across ions of different masses. It corresponds to an uncertainty of the mean droplet diameter of $\pm$50 nm. **d:** The solid black line shows the relation between ion energy and droplet charge for a homogeneous charge distribution. The color map shows the measured distribution of proton energies (below the line) and the corresponding estimate for the droplet charges (above the line). The red dash-dotted line indicates the Rayleigh charge limit q_R for a 1,2-PDO droplet with a diameter of 590 nm.

6.7 Droplet charge and stability

In order to evaluate the relevance of the previously demonstrated size estimate, it is essential to understand whether the droplets remain intact after ionization. Droplets carrying charges close to or even above the Rayleigh limit [158], are likely to disintegrate into smaller droplets of different sizes, making the size estimate less meaningful. Charged droplets are stable if the surface tension can counteract the Coulomb repulsion of the charges. For this to be the case, the surface energy E_S has to be larger than half of the Coulomb energy E_C [172, 173]:

$$E_S > \frac{1}{2}E_C, \tag{6.5}$$

$$4\pi\gamma R^2 > \frac{1}{2}\frac{q^2}{8\pi\varepsilon_0 R}, \tag{6.6}$$

where γ is the surface tension, R is the droplet radius, q is the charge of the droplet and ε_0 is the vacuum permittivity. The Coulomb energy corresponds to the amount of work required for placing a total amount of charge q on the surface of a sphere with radius R. An intuitive derivation for this expression is shown in Appendix B. Condition (6.6) can be solved for q to obtain the Rayleigh condition for stable droplets:

$$q < \underbrace{8\pi\sqrt{\gamma\varepsilon_0 R^3}}_{\equiv q_R}, \tag{6.7}$$

which can be used to demonstrate that droplet fission stabilizes the system energetically. For example, consider a droplet holding a charge $q = q_R$, which disintegrates into two droplets holding equal amounts of charge $q_2 = q_R/2$, i.e., half of the original charge. The newly generated droplets will have half of the volume V of the original droplet, with $V \propto R^3$. The right-hand side of Eq. (6.7) scales with the square root of the volume, resulting in a new value of $q_R/\sqrt{2}$ after the fission event. Since $q_R/2 < q_R/\sqrt{2}$, the newly formed droplets will satisfy $E_S > \frac{1}{2}E_C$ and therefore be stable.

To evaluate the stability of the ionized droplets inside the reaction nanoscope, knowledge about their charge is necessary. In reaction nanoscopy, the Coulomb repulsion from the charged surface is the main contribution to the final ion energy [47, 52]. A measurement of the ion energy can thus be used for estimating the total charge of a droplet. Combined with the size determination from the section above, this allows a stability evaluation. In order to simplify the procedure, a homogeneous charge distribution on the droplet surface is assumed. To reach the same energy with a homogeneous charge distribution, a higher charge compared to a localized charge distribution is required. This means that the assumption of a homogeneous charge distribution leads to an overestimation of the surface charge. As long as such an estimate results in a charge below the Rayleigh limit, droplet stability is assured. Only if a charge close to or above the Rayleigh limit is obtained, the question of droplet stability cannot be answered definitively, as the actual charge might be much lower than the estimate.

With a homogeneous charge distribution, the relationship between the kinetic energy E_k of a monovalent ion with charge $+e$ and the charge of the droplet q follows from the electrostatic potential of a homogeneously charged sphere:

$$q = \frac{4\pi\varepsilon_0}{e} \cdot E_k R. \tag{6.8}$$

Similar to the ion energy scaling with mass we found for silica nanoparticles (see Chapter 5), we observe a decreasing fragment energy with ion mass. Assuming that this effect is due to the gradual discharging of the nanosphere with time, as described in the corresponding section, it is most representative to use the most energetic/lightest ions, the protons, as a probe for the surface charge. The energy distribution of the protons is shown in Fig. 6.6d, encoded by the color scale below the linear function (solid black line). The proton energy distribution is centered around an energy of 30 eV for this measurement taken at a peak laser intensity of about $5 \times 10^{13}\,\mathrm{W/cm^2}$, which corresponds to a droplet charge of approximately 6 ke (see color scale above the solid black line). Even the highest energy protons at about 50 eV still indicate emission from stable droplets with a corresponding droplet charge of 11 ke and a Rayleigh limit of $q_R \approx 16$ ke, using the estimated diameter of $d = 590$ nm. The Rayleigh limit q_R is indicated in Fig. 6.6d by the red dashed-dotted line.

It has been reported in the literature [174] that the Rayleigh limit cannot be used as an exact boundary as to when droplet fission sets in. However, since the retrieved charge values here are significantly below the Rayleigh limit and since they are overestimating the surface charge due to the assumed homogeneity, it can be safely concluded that the droplets studied here did not undergo droplet fission after the ionization by the laser pulse.

6.8 Ion emission: gas-phase vs. droplet

The reaction nanoscopy data presented in this chapter were acquired for both isomers of PDO. Before carrying out a comparison between 1,2-PDO and 1,3-PDO, however, we will attempt to isolate all features of the ion spectra that are isomer independent and thus only related to the fact that the molecules are contained in a droplet. For this purpose, the ion data were first grouped by the integrated electron signal. All ions detected with a small or absent electron signal originate from the ionization of single molecules in the gas phase. As discussed above, the ion data for large electron signals contain both gas-phase and droplet events. The background signal from gas-phase molecules is caused by the droplet evaporation inside the vacuum chamber, which increases the probability that a single gas-phase molecule is ionized in the laser focus at the same time as a droplet. To our advantage, however, the gas-phase signal is spatially separable from the droplet signal. As shown in Fig. 6.7, all gas-phase ions arrive close to $y = 0$ mm at the detector. The droplet ion data was thus selected by defining a pair of polygons in the TOF vs. y histogram for every ion species that was uniquely identifiable.

The normalized counts of these ionic fragments are shown in Fig. 6.9. The most striking droplet-specific feature is the high relative yield of protons (for both isomers) compared

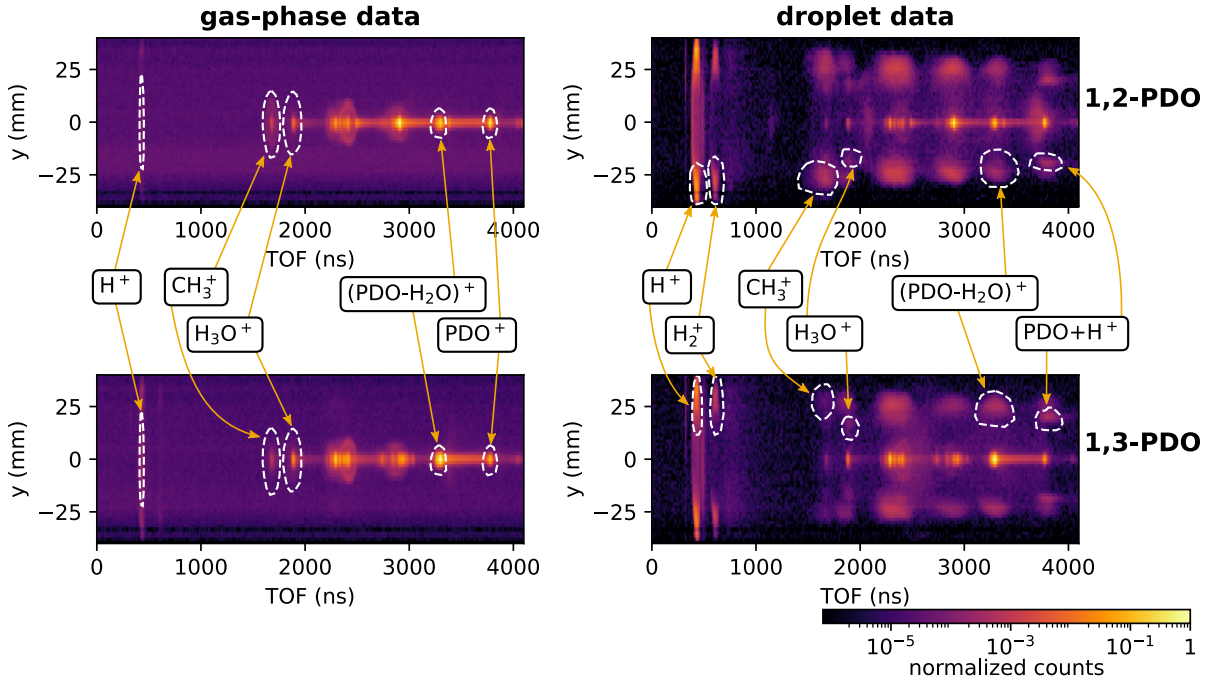

Figure 6.7: Filtering ion signals for gas-phase and droplet data. Two measurements are shown, one for 1,2-propanediol (1,2-PDO, panels a and b) and one for 1,3-propanediol (1,3-PDO, panels c and d). Both measurements were split into gas-phase data and droplet data based on the strength of the electron signal, which is recorded in coincidence with the ions. Gas-phase data (first column, panels **a** and **c**) are defined by a small or absent electron signal. Droplet data (second column, panels **b** and **d**) are defined as the complementary set. The ion species listed in the middle were identified after calibrating the time-of-flight. The polygons indicated by the white dashed lines were used for the yield comparison in Fig. 6.9.

to the proton yield from single gas-phase molecules. This observation is very similar to previous reaction nanoscopy studies, where protons were the most abundant ion species as well [47, 127]. The strong proton signal is likely caused by the combination of the high number of protons on the surface and their low electronegativity compared to the other constituents of PDO [175]. The low electronegativity suggests that all other atomic species are favored for the formation of new bonds after the ionization by the laser pulse.

Apart from the protons themselves, we observed several ions whose production is likely favored/enhanced due to the high abundance of protons shortly after the laser pulse. The simplest of these ions is the H_2^+ molecular ion. An indication that this fragment is a result of the proton-rich surface but not specific to the PDO molecules, in particular, is that H_2^+ has been observed before in reaction nanoscopy experiments with silica nanoparticles [127].

A second example that is compatible with the hypothesis that the presence of protons influences the ion spectra is the enhanced protonation of water molecules on the droplet. To be more precise, we observe that the ratios between the H_3O^+ channel ($m = 19\,\mathrm{u}$) and the H_2O-loss channel ($m = 58\,\mathrm{u}$) are significantly different for gas-phase and droplet data. For the gas-phase data, the ratio N_{19}/N_{58} is 0.50 and 0.38 for 1,2-PDO and 1,3-PDO respectively. For the ion emission from the droplets, these ratios increase to 1.95 and 1.23,

respectively. This corresponds to an increase by a factor of 3.9 in the case of 1,2-PDO and a factor of 3.3 for 1,3-PDO. We interpret this increase such that at least part of the generated neutral water molecules from the dissociation reaction

$$\mathrm{PDO}^+ \rightarrow \mathrm{H_2O} + \underbrace{\mathrm{C_3H_6O^+}}_{m=58} \tag{6.9}$$

get protonated on the surface of the droplet, which leads to an increased H_3O^+ yield relative to the H_2O-loss channel ($m = 58\,\mathrm{u}$).

In addition, we observe the protonation of the PDO molecule on the droplet surface. See Fig. 6.9b at the ion mass of $m = 77\,\mathrm{u}$. Due to the high mass of the protonated PDO molecule, its time-of-flight spectrum overlaps with the spectra of ions with similar masses, such as the PDO^+ ion ($m = 76\,\mathrm{u}$). However, as can be seen in the position-resolved TOF histograms of Fig. 6.7b,d, there is a clear shift between the background PDO^+ ions close to $y = 0$ and the protonation signal. The same is true for the histograms of Fig. 6.4, where the shift is evident for the circularly polarized case. A more rigid proof for the observation of protonated PDO is provided in Fig. 6.8 where we use the constraint that the momentum distribution is expected to peak at zero momentum along the time-of-flight axis. As shown in the figure, this is only the case if a mass of $m = 77\,\mathrm{u}$, i.e., protonated PDO, is assumed for the signal at large $|y|$-values. The protonation of molecules on the surface has two physical implications. The first one is that the surface ionization by the laser is not directly responsible for the generation of these ions. The laser is just producing an excess of positive charge on the surface, and the ionization of the PDO molecules only happens in a second step, namely protonation. The second implication of protonation is multi-molecular reactions. These have only been recently demonstrated with reaction nanoscopy [127] using silica nanoparticles.

In the field of electrospray mass spectroscopy, however, both of these findings are well established. For electrospray sources operated in positive mode, protonation is the predominant ion generation mechanism [176] and the study of chemical reactions on charged droplets is an ongoing and rapidly developing field [177]. These similarities to our results suggest that reaction nanoscopy might be suitable for studying more complex chemical reactions from droplets containing more than one molecular species. Especially the possibility of pump-probe measurements in reaction nanoscopy has a high potential for new insights into the time-evolution of chemical reactions on charged droplets, which is impossible with an electrospray ionization source.

6.9 Isomer comparison

In addition to the analysis of the droplet-specific features of the reaction nanoscopy spectra in the last section, we can infer information about molecular effects from a comparison of both PDO isomers, 1,2-PDO and 1,3-PDO. Their fragmentation behavior upon irradiation by the laser pulse is overall quite similar for both the gas-phase and the droplet-related data. For one specific fragment, however, we find an enhanced production on the 1,2-PDO

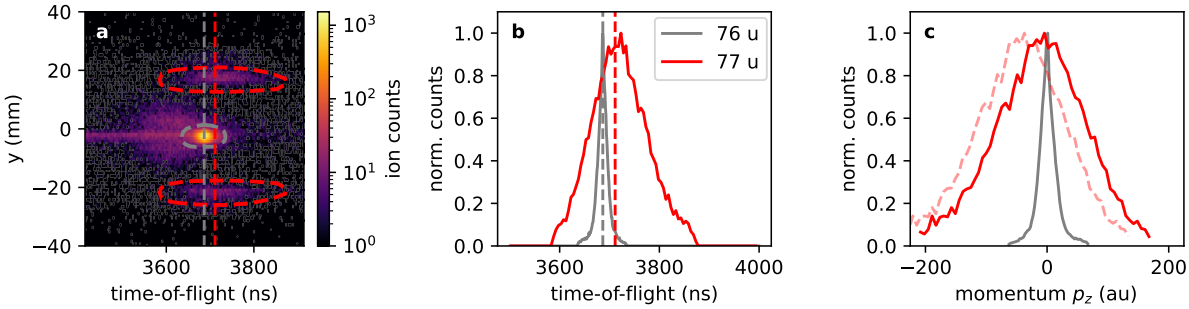

Figure 6.8: Proving PDO protonation by momentum symmetry. **a:** Time-of-flight vs. position histogram for masses of 76 u (gray) and 77 u (red), corresponding to the PDO^+ ion and protonated PDO. The vertical lines indicate the arrival time of ions with zero momentum along the time-of-flight axis ($p_z = 0$). The polygons indicate the selected data for panels b and c. **b:** Time-of-flight histograms for selected data. **c:** Solid lines: Momentum histograms for the selected data. Dashed line: Momentum histogram for the $m = 77$ u data under the assumption that the mass is 76 u, which causes an unphysical momentum distribution offset from $p_z = 0$. This proves that the ion counts within the red polygon indeed correspond to protonated PDO ($m = 77$ u).

droplet surface. Specifically, the data suggests that more CH_3^+ is produced for 1,2-PDO droplets than for gas-phase 1,2-PDO. To quantify this, we compare the CH_3^+ yield for both isomers. For gas-phase PDO, a ratio of about 2:1 between CH_3^+ from 1,2-PDO and 1,3-PDO is found (see Fig. 6.9a, blue rectangle). The larger yield of CH_3^+ from 1,2-PDO is unsurprising since it can be produced directly by dissociative ionization, while bond rearrangement is required for the case of 1,3-PDO. The surprising part is that the same ratio increases by a factor of three (to about 6:1) when the molecules are bound in the droplet (see Fig. 6.9b, blue rectangle).

Our collaborators carried out DFT simulations to evaluate how this enhancement might relate to the surface structure of the PDO droplets. As described above, a model system of six layers with rotational symmetry around the center was used to investigate the droplet surface. The minimum energy configurations were obtained for both isomers and are displayed in Fig. 6.9c for 1,2-PDO and Fig. 6.9d for 1,3-PDO. For both cases, the hydrogen bonds between neighboring molecules determine the molecular alignment. This leads to a linear arrangement of the (linear) 1,3-PDO molecules and results in outward pointing CH_3 groups on the surface of 1,2-PDO. The equilibrium configuration of the 1,2-PDO is the result of a steric effect between the methyl groups, which increase the energy of the system, and the hydrogen bonds between the OH groups, which stabilize the system upon a small configuration change. This change in energy is displayed in Fig. 6.10 for a rotation around the C2-C3 bond.

Based on the results of the DFT simulation, we assume that the enhancement of the CH_3^+ yield from 1,2-PDO droplets compared to the gas phase is due to the outward-facing methyl groups on the droplet surface caused by the hydrogen bonds between neighboring PDO molecules. On the charged surface, these methyl groups are almost radially aligned, i.e., parallel to the direction of the electric field on the surface, allowing for a more efficient

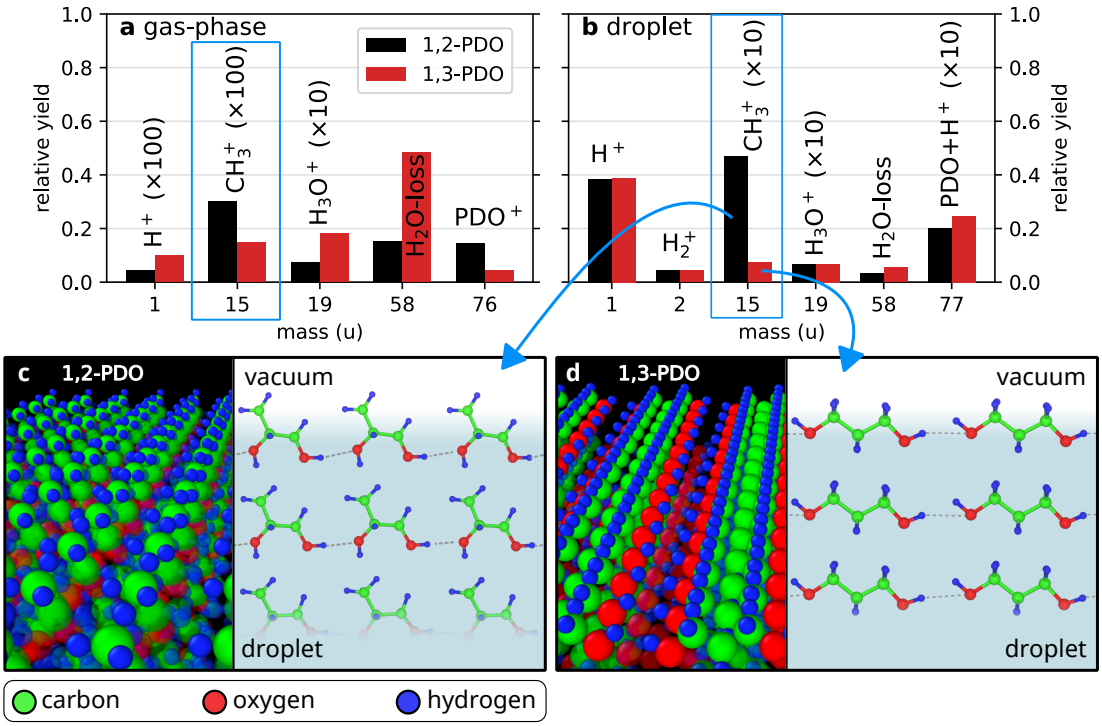

Figure 6.9: Isomer comparison of the fragmentation channels for gas-phase propanediol and propanediol droplets. **a:** Gas-phase data 1,2-propanediol and 1,3-propanediol for selected fragments. The data was obtained by filtering the droplet measurements on events with a low electron signal. The yield is normalized to the total number of counts after filtering. **b:** The same measurements as in panel a filtered on droplet events (high electron signal). The data is normalized to the total number of droplet ions, i.e., ions with a high electron signal. The fragment specific filters for every fragment are shown in Fig. 6.7. The blue rectangles mark the CH_3^+ ion for which we find a significant difference between the gas-phase and droplet data. We attribute this to the molecular alignment of the propanediol molecules on the droplet surface (see text for details). Panels c and d present density functional theory results for the molecular alignment of both isomers. Only the top three layers are shown. The gray dotted lines represent hydrogen bonds.

bond dissociation compared to the randomly aligned PDO molecules in the gas phase.

6.10 Conclusion

In summary, the results of this chapter demonstrate that the application of the reaction nanoscopy technique to droplets has enormous potential for the study of surface chemistry. It was shown that the angular distribution of the laser-generated ions can be used for an in-situ determination of the most prominent droplet size in the aerosol stream. Furthermore, the energy of the emitted ions was used to estimate a typical value for the total charge on the droplets. Both of these estimates were then combined to evaluate the stability of the droplets based on the Rayleigh criterion. It was found that the droplets did not undergo fission after the ionization, which ensured stable conditions during the process of ion emission.

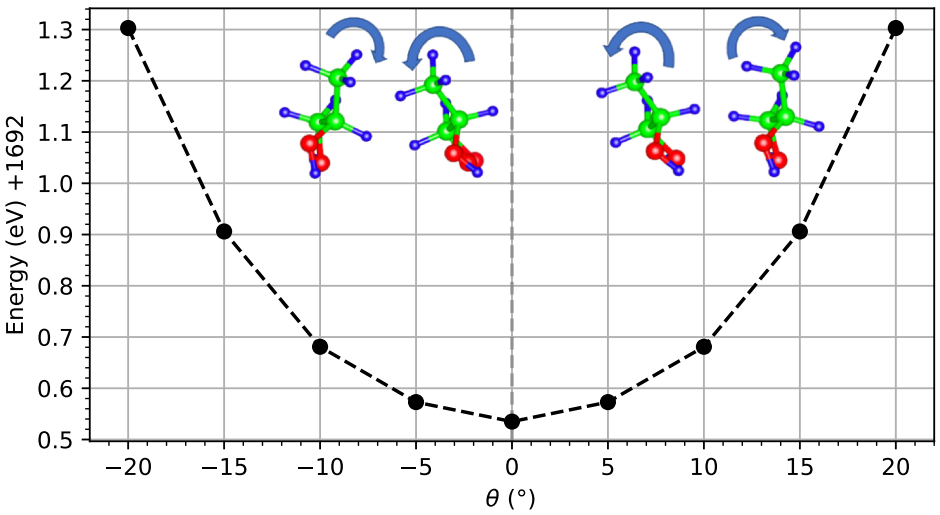

Figure 6.10: Energy of 1,2-propanediol with respect to angle of rotation θ. The rotation axis is along the C2-C3 bond, and $\theta = 0°$ corresponds to the equilibrium configuration obtained via energy minimization. The rotations are depicted by the blue arrows.

In this proof-of-principle study, propanediol was used as the droplet material, enabling comparative experiments with two isomers, 1,2-propanediol, and 1,3-propanediol. The coincident detection of the electron signal allowed a comparison of ion fragments from single, gas-phase molecules with ions originating from the droplet surface. An analysis of isomer-independent features in these ion spectra revealed that, generally, the ion emission from droplets is dominated by a high yield of protons and the protonation of fragments. When generated on the droplet surface, we could even identify protonation as the dominant ionization mechanism for the propanediol molecule. From the isomer-dependent parts of the ion spectra, increased production of CH_3^+ ions from droplets of 1,2-propanediol could be concluded. Density functional theory simulations for the droplet surface for both isomers showed that the alignment of the methyl groups on the surface of 1,2-propanediol droplets likely causes the increase.

These results demonstrate that reaction nanoscopy applied to droplets provides a sensitivity to the microscopic details of the surface on a molecular level. It furthermore allows a physical in-situ characterization of the droplets, which is unique to the technique. Consequently, we expect new insights into chemical reactions on the surface of charged droplets from reaction nanoscopy experiments with more complex droplet materials.

Appendix A

Expression for elliptical input fields for the FDTD simulations

A quarter-wave plate used under an angle α between the optical axis of the wave plate and the polarization direction of a linearly polarized input field will, in general, result in an elliptical output field with a rotated main axis with respect to the direction of the input polarization. Here, we will briefly derive an expression for the output field as a function of the wave plate position. The derivation was used for the electric field components along the axes of the lab frame in the FDTD simulations.

The electric field vector of the input field is described by $\mathbf{E} = (0, E_y, 0)$ assuming polarization along the y-axis. The field E_y shall be defined as a complex quantity:

$$E_y = \sqrt{I(t)} e^{-i\omega_0 t + i\varphi(t)}, \tag{A.1}$$

where $I(t)$ is the instantaneous intensity in arbitrary units, ω_0 is the central frequency and $\varphi(t)$ is the temporal phase. This electric field definition is equivalent to the definition in Chapter 2 after taking the real part and choosing $\varphi(t)$ adequately. The wave plate acts on the electric field by inducing a phase shift between the electric field components along and perpendicular to the wave plate's optical axis. The components can be obtained by a projection of the input field onto a unit vector parallel to the optical axis ($\mathbf{e}_\parallel$) and a unit vector perpendicular to it ($\mathbf{e}_\perp$). For an angle α between the optical axis and the input polarization (i.e. the y-direction), these vectors can be written as:

$$\mathbf{e}_\parallel = \begin{pmatrix} \sin(\alpha) \\ \cos(\alpha) \\ 0 \end{pmatrix}, \tag{A.2}$$

$$\mathbf{e}_\perp = \begin{pmatrix} \cos(\alpha) \\ -\sin(\alpha) \\ 0 \end{pmatrix}. \tag{A.3}$$

With the field expressed by these vectors, a phase shift δ can be applied to account for the action of the wave plate:

$$\mathbf{E} = E_y \left(\cos(\alpha) e^{i\delta} \mathbf{e}_\parallel - \sin(\alpha) \mathbf{e}_\perp \right). \tag{A.4}$$

Inserting the expression for E_y of Eq. (A.1), and taking the real part of the result, yields the parametric form of an ellipse in the plane of $\mathbf{e}_\parallel$ and $\mathbf{e}_\perp$:

$$\Re(\mathbf{E}) = \sqrt{I(t)}\left(\cos(\alpha)\cos(-\omega_0 t + \varphi(t) + \delta)\mathbf{e}_\parallel + \sin(\alpha)\cos(-\omega_0 t + \varphi(t))\mathbf{e}_\perp\right) \tag{A.5}$$

$$= \sqrt{I(t)}\left(\cos(\alpha)\sin(t')\mathbf{e}_\parallel + \sin(\alpha)\cos(t')\mathbf{e}_\perp\right) \tag{A.6}$$

$$= \sqrt{I(t)}\left(a\sin(t')\mathbf{e}_\parallel + b\cos(t')\mathbf{e}_\perp\right). \tag{A.7}$$

Here, a phase shift of $\delta = -\pi/2$ was inserted to account for the action of the quarter-wave plate. The quantities $a = \cos(\alpha)$ and $b = \sin(\alpha)$ are the two main axes of the ellipse determined by the wave plate angle and the parameter $t' = -\omega_0 t + \varphi(t)$ was introduced as a shorthand. The directions of the main axes are given by $\mathbf{e}_\parallel$ and $\mathbf{e}_\perp$ which are rotated by an angle α w.r.t. the lab frame. From Eq. (A.7) it is obvious that a wave plate setting of 45° corresponds to circular polarization since $\cos(45°) = \sin(45°) = a = b = 1/\sqrt{2}$. In general, the ratio between b and a is given by $b/a = \tan(\alpha)$.

In order to obtain the lab frame expressions for the electric field for the FDTD simulations, Eq. (A.2) and Eq. (A.3) were inserted into (A.7):

$$\mathbf{E}(\alpha) = \sqrt{I(t)}\begin{pmatrix} a\sin(t')\sin(\alpha) + b\cos(t')\cos(\alpha) \\ a\sin(t')\cos(\alpha) - b\cos(t')\sin(\alpha) \end{pmatrix} \tag{A.8}$$

$$= \sqrt{I(t)}\begin{pmatrix} \cos(\alpha) & -\sin(\alpha) \\ \sin(\alpha) & \cos(\alpha) \end{pmatrix}\begin{pmatrix} b\cos(t') \\ a\sin(t') \end{pmatrix}. \tag{A.9}$$

The final representation of a multiplication between a rotation matrix and and a vector for a parameterized ellipse summarizes the actions of the quarter-wave plate: rotation and ellipticity change.

Appendix B

Energy of a charged spherical surface

The problem of calculating the total energy W of a sphere with radius R and a total charge q on its surface is a standard electrostatic problem and is often solved under the assumption of infinitesimal charge increments. Here, we derive the formula under the assumption that q is a multiple of the elementary charge $q = Ne$ where N is an integer. Starting with a sphere that only holds a single elementary charge, the work W_1 required to bring a second one from $r = \infty$ to $r = R$ is given by:

$$W_1 = \int_{\infty}^{R} \mathrm{d}r F(r) = \int_{\infty}^{R} \mathrm{d}r \, \frac{e^2}{4\pi\varepsilon_0 r^2} = \frac{e^2}{4\pi\varepsilon_0 R}, \tag{B.1}$$

where $F(r)$ is the Coulomb force and ε_0 is the vacuum permittivity. Adding the next elementary charge e requires twice the amount of work since the sphere already holds a total charge of $2e$:

$$W_2 = \int_{\infty}^{R} \mathrm{d}r \, \frac{2e \cdot e}{4\pi\varepsilon_0 r^2} = 2 \cdot \frac{e^2}{4\pi\varepsilon_0 R} = 2W_1. \tag{B.2}$$

This generalizes such that the addition of the n-th elementary charge requires a work of $W_n = nW_1$. The total work is thus given by:

$$W = \sum_{n=1}^{N} W_n = W_1 \sum_{n=1}^{N} n = \frac{e^2}{4\pi\varepsilon_0 R} \cdot \frac{N(N+1)}{2} \approx \frac{(Ne)^2}{8\pi\varepsilon_0 R} = \frac{q^2}{8\pi\varepsilon_0 R}. \tag{B.3}$$

Here we used that $N \approx N + 1$ if N is large enough.

Bibliography

[1] F.-K. Liu. „Analysis and applications of nanoparticles in the separation sciences: A case of gold nanoparticles.“ *J. Chromatogr. A* 1216.52 (2009). Particle Analysis, 9034–9047. DOI: 10.1016/j.chroma.2009.07.026.

[2] N. Na, X. Cui, T. De Beer, et al. „The use of silica nanoparticles for gas chromatographic separation.“ *J. Chromatogr. A* 1218.28 (2011), 4552–4558. DOI: 10.1016/j.chroma.2011.05.043.

[3] E. Guihen. „Nanoparticles in modern separation science.“ *TrAC* 46 (2013), 1–14. DOI: 10.1016/j.trac.2013.01.011.

[4] C.-K. Chang, C.-C. Wu, Y.-S. Wang, and H.-C. Chang. „Selective Extraction and Enrichment of Multiphosphorylated Peptides Using Polyarginine-Coated Diamond Nanoparticles.“ *Anal. Chem.* 80.10 (2008), 3791–3797. DOI: 10.1021/ac702618h.

[5] J.-H. Lin and W.-L. Tseng. „Gold nanoparticles for specific extraction and enrichment of biomolecules and environmental pollutants.“ *Rev. Anal. Chem.* 31.3-4 (2012), 153–162. DOI: 10.1515/revac-2012-0029.

[6] L. Ling, X.-Y. Huang, and W.-X. Zhang. „Enrichment of Precious Metals from Wastewater with Core–Shell Nanoparticles of Iron.“ *Adv. Mater.* 30.17 (2018), 1705703. DOI: 10.1002/adma.201705703.

[7] R. Jin. „The impacts of nanotechnology on catalysis by precious metal nanoparticles.“ *Nanotechnol. Rev.* 1.1 (2012), 31–56. DOI: 10.1515/ntrev-2011-0003.

[8] D. Astruc. „Introduction: Nanoparticles in Catalysis.“ *Chem. Rev.* 120.2 (2020), 461–463. DOI: 10.1021/acs.chemrev.8b00696.

[9] C. Xie, Z. Niu, D. Kim, M. Li, and P. Yang. „Surface and Interface Control in Nanoparticle Catalysis.“ *Chem. Rev.* 120.2 (2020), 1184–1249. DOI: 10.1021/acs.chemrev.9b00220.

[10] I. Ganesh. „Electrochemical conversion of carbon dioxide into renewable fuel chemicals – The role of nanomaterials and the commercialization.“ *Renew. Sust. Energ. Rev.* 59 (2016), 1269–1297. DOI: 10.1016/j.rser.2016.01.026.

[11] J. Park, T. Kwon, J. Kim, et al. „Hollow nanoparticles as emerging electrocatalysts for renewable energy conversion reactions.“ *Chem. Soc. Rev.* 47 (22 2018), 8173–8202. DOI: 10.1039/C8CS00336J.

[12] S. Banerjee and R. N. Zare. „Syntheses of Isoquinoline and Substituted Quinolines in Charged Microdroplets.“ *Angew. Chem. Int. Ed.* 54.49 (2015), 14795–14799. DOI: 10.1002/anie.201507805.

[13] X. Yan, R. M. Bain, and R. G. Cooks. „Organic Reactions in Microdroplets: Reaction Acceleration Revealed by Mass Spectrometry.“ *Angew. Chem. Int. Ed.* 55.42 (2016), 12960–12972. DOI: 10.1002/anie.201602270.

[14] Y.-H. Lai, S. Sathyamoorthi, R. M. Bain, and R. N. Zare. „Microdroplets Accelerate Ring Opening of Epoxides.“ *JASMS* 29.5 (2018), 1036–1043. DOI: 10.1007/s13361-018-1908-z.

[15] M. F. Ruiz-Lopez, J. S. Francisco, M. T. C. Martins-Costa, and J. M. Anglada. „Molecular reactions at aqueous interfaces.“ *Nat. Rev. Chem.* 4.9 (2020), 459–475. DOI: 10.1038/s41570-020-0203-2.

[16] B. J. Burris and A. K. Badu-Tawiah. „Enzyme-Catalyzed Hydrolysis of Lipids in Immiscible Microdroplets Studied by Contained-Electrospray Ionization.“ *Anal. Chem.* 93.38 (2021), 13001–13007. DOI: 10.1021/acs.analchem.1c02785.

[17] H. Nie, Z. Wei, L. Qiu, X. Chen, D. T. Holden, and R. G. Cooks. „High-yield gram-scale organic synthesis using accelerated microdroplet/thin film reactions with solvent recycling.“ *Chem. Sci.* 11 (9 2020), 2356–2361. DOI: 10.1039/C9SC06265C.

[18] X. Zhong, H. Chen, and R. N. Zare. „Ultrafast enzymatic digestion of proteins by microdroplet mass spectrometry.“ *Nat. Commun.* 11.1 (2020), 1049. DOI: 10.1038/s41467-020-14877-x.

[19] C. M. Dobson, G. B. Ellison, A. F. Tuck, and V. Vaida. „Atmospheric aerosols as prebiotic chemical reactors.“ *PNAS* 97.22 (2000), 11864–11868. DOI: 10.1073/pnas.200366897.

[20] M. Ruiz-Bermejo, L. A. Rivas, A. Palacín, C. Menor-Salván, and S. Osuna-Esteban. „Prebiotic Synthesis of Protobiopolymers Under Alkaline Ocean Conditions.“ *Orig. Life Evol. Biosph.* 41.4 (2011), 331–345. DOI: 10.1007/s11084-010-9232-z.

[21] A. Fallah-Araghi, K. Meguellati, J.-C. Baret, et al. „Enhanced Chemical Synthesis at Soft Interfaces: A Universal Reaction-Adsorption Mechanism in Microcompartments.“ *Phys. Rev. Lett.* 112 (2 2014), 028301. DOI: 10.1103/PhysRevLett.112.028301.

[22] W. Guo, A. B. Kinghorn, Y. Zhang, et al. „Non-associative phase separation in an evaporating droplet as a model for prebiotic compartmentalization.“ *Nat. Commun.* 12.1 (2021), 3194. DOI: 10.1038/s41467-021-23410-7.

[23] S. Sonwani, S. Madaan, J. Arora, et al. „Inhalation Exposure to Atmospheric Nanoparticles and Its Associated Impacts on Human Health: A Review.“ *Front. Sustain. Cities.* 3 (2021). DOI: 10.3389/frsc.2021.690444.

[24] J. N. Smith, K. C. Barsanti, H. R. Friedli, et al. „Observations of aminium salts in atmospheric nanoparticles and possible climatic implications.“ *PNAS* 107.15 (2010), 6634–6639. DOI: 10.1073/pnas.0912127107.

[25] I. Riipinen, T. Yli-Juuti, J. R. Pierce, et al. „The contribution of organics to atmospheric nanoparticle growth.“ *Nat. Geosci.* 5.7 (2012), 453–458. DOI: 10.1038/ngeo1499.

[26] A. C. Martin, G. C. Cornwell, S. A. Atwood, et al. „Transport of pollution to a remote coastal site during gap flow from California's interior: impacts on aerosol composition, clouds, and radiative balance.“ *Atmospheric Chem. Phys.* 17.2 (2017), 1491–1509. DOI: 10.5194/acp-17-1491-2017.

[27] G. Doria, J. Conde, B. Veigas, et al. „Noble Metal Nanoparticles for Biosensing Applications.“ *Sensors* 12.2 (2012), 1657–1687. DOI: 10.3390/s120201657.

[28] M. J. Mitchell, M. M. Billingsley, R. M. Haley, M. E. Wechsler, N. A. Peppas, and R. Langer. „Engineering precision nanoparticles for drug delivery.“ *Nat. Rev. Drug. Discov.* 20.2 (2020), 101–124. DOI: 10.1038/s41573-020-0090-8.

[29] D. Gonzalez-Carter, X. Liu, T. A. Tockary, et al. „Targeting nanoparticles to the brain by exploiting the blood–brain barrier impermeability to selectively label the brain endothelium.“ *PNAS* 117.32 (2020), 19141–19150. DOI: 10.1073/pnas.2002016117.

[30] S. Ohta, E. Kikuchi, A. Ishijima, T. Azuma, I. Sakuma, and T. Ito. „Investigating the optimum size of nanoparticles for their delivery into the brain assisted by focused ultrasound-induced blood–brain barrier opening.“ *Sci. Rep.* 10.1 (2020), 18220. DOI: 10.1038/s41598-020-75253-9.

[31] Y. Zhou, Z. Peng, E. S. Seven, and R. M. Leblanc. „Crossing the blood-brain barrier with nanoparticles.“ *J. Control. Release* 270 (2018), 290–303. DOI: 10.1016/j.jconrel.2017.12.015.

[32] C. P. Profaci, R. N. Munji, R. S. Pulido, and R. Daneman. „The blood–brain barrier in health and disease: Important unanswered questions.“ *J. Exp. Med.* 217.4 (2020). DOI: 10.1084/jem.20190062.

[33] Y. Pan, X. Li, G. Yang, et al. „Serological immunochromatographic approach in diagnosis with SARS-CoV-2 infected COVID-19 patients.“ *J. Infect.* 81.1 (2020), e28–e32. DOI: 10.1016/j.jinf.2020.03.051.

[34] J. Sun, B. Bhushan, and J. Tong. „Structural coloration in nature.“ *RSC Adv.* 3 (35 2013), 14862–14889. DOI: 10.1039/C3RA41096J.

[35] X. Fan, W. Zheng, and D. J. Singh. „Light scattering and surface plasmons on small spherical particles.“ *Light Sci. Appl.* 3.6 (2014), e179–e179. DOI: 10.1038/lsa.2014.60.

[36] A. Devilez, X. Zambrana-Puyalto, B. Stout, and N. Bonod. „Mimicking localized surface plasmons with dielectric particles.“ *Phys. Rev. B* 92 (24 2015), 241412. DOI: 10.1103/PhysRevB.92.241412.

[37] V. A. Zenin and S. I. Bozhevolnyi. „Nanofocusing: reaching out.“ *Nanophotonics* 10.14 (2021), 3613–3618. DOI: doi:10.1515/nanoph-2021-0267.

[38] X. X. Han, R. S. Rodriguez, C. L. Haynes, Y. Ozaki, and B. Zhao. „Surface-enhanced Raman spectroscopy.“ *Nat. Rev. Methods Primers* 1.1 (Jan. 2022). DOI: 10.1038/s43586-021-00083-6.

[39] J. Obermeier, T. Schumacher, and M. Lippitz. „Nonlinear spectroscopy of plasmonic nanoparticles.“ *Adv. Phys.: X* 3.1 (2018), 1454341. DOI: 10.1080/23746149.2018.1454341.

[40] G. Mie. „Beiträge zur Optik trüber Medien, speziell kolloidaler Metallösungen.“ *Ann. Phys.* 330.3 (1908), 377–445. DOI: 10.1002/andp.19083300302.

[41] S. Zherebtsov, T. Fennel, J. Plenge, et al. „Controlled near-field enhanced electron acceleration from dielectric nanospheres with intense few-cycle laser fields.“ *Nat. Phys.* 7 (2011), 656. DOI: 10.1038/nphys1983.

[42] F. Süßmann, L. Seiffert, S. Zherebtsov, et al. „Field propagation-induced directionality of carrier-envelope phase-controlled photoemission from nanospheres.“ *Nat. Commun.* 6.1 (2015), 7944. DOI: 10.1038/ncomms8944.

[43] L. Seiffert, P. Henning, P. Rupp, et al. „Trapping field assisted backscattering in strong-field photoemission from dielectric nanospheres.“ *J. Mod. Opt.* 64.10-11 (2017), 1096–1103. DOI: 10.1080/09500340.2017.1288838.

[44] L. Seiffert, Q. Liu, S. Zherebtsov, et al. „Attosecond chronoscopy of electron scattering in dielectric nanoparticles.“ *Nat. Phys.* 13.8 (2017), 766–770. DOI: 10.1038/nphys4129.

[45] Q. Liu, L. Seiffert, F. Süßmann, et al. „Ionization-Induced Subcycle Metallization of Nanoparticles in Few-Cycle Pulses.“ *ACS Photonics* 7.11 (2020), 3207–3215. DOI: 10.1021/acsphotonics.0c01282.

[46] L. Seiffert, S. Zherebtsov, M. F. Kling, and T. Fennel. „Strong-field physics with nanospheres.“ *Adv. Phys.: X* 7.1 (2022), 2010595. DOI: 10.1080/23746149.2021.2010595.

[47] P. Rupp, C. Burger, N. G. Kling, et al. „Few-cycle laser driven reaction nanoscopy on aerosolized silica nanoparticles.“ *Nat. Commun.* 10.1 (2019), 4655. DOI: 10.1038/s41467-019-12580-0.

[48] D. D. Hickstein, F. Dollar, J. L. Ellis, et al. „Mapping Nanoscale Absorption of Femtosecond Laser Pulses Using Plasma Explosion Imaging.“ *ACS Nano* 8.9 (2014), 8810–8818. DOI: 10.1021/nn503199v.

[49] W. Zhang, R. Dagar, P. Rosenberger, et al. „All-optical nanoscopic spatial control of molecular reaction yields on nanoparticles.“ *Optica* 9.5 (2022), 551–560. DOI: 10.1364/OPTICA.453915.

[50] Rosenberger, Philipp, Dagar, Ritika, Zhang, Wenbin, et al. „Imaging elliptically polarized infrared near-fields on nanoparticles by strong-field dissociation of functional surface groups.“ *Eur. Phys. J. D* 76.6 (2022), 109. DOI: 10.1140/epjd/s10053-022-00430-6.

[51] L. Seiffert. „Semi-classical description of near-field driven attosecond photoemission from nanostructures.“ PhD thesis. Universität Rostock, 2018, pp. 11–36.

[52] P. Rosenberger, P. Rupp, R. Ali, et al. „Near-Field Induced Reaction Yields from Nanoparticle Clusters.“ *ACS Photonics* 7.7 (2020), 1885–1892. DOI: 10.1021/acsphotonics.0c00823.

[53] M. V. Ammosov, N. B. Delone, and V. P. Krainov. „Tunnel ionization of complex atoms and of atomic ions in an alternating electromagnetic field.“ *Sov. Phys. JETP* 64 (1986), 1191–1194.

[54] G Mainfray and G Manus. „Multiphoton ionization of atoms.“ *Rep. Prog. Phys.* 54.10 (1991), 1333–1372. DOI: 10.1088/0034-4885/54/10/002.

[55] H. R. Reiss. „Foundations of the Strong-Field Approximation.“ *Progress in Ultrafast Intense Laser Science III*. Berlin, Heidelberg: Springer Berlin Heidelberg, 2008, 1–31. DOI: 10.1007/978-3-540-73794-0_1.

[56] D. W. Mackowski. „Calculation of total cross sections of multiple-sphere clusters.“ *J. Opt. Soc. Am. A* 11.11 (1994), 2851–2861. DOI: 10.1364/JOSAA.11.002851.

[57] D. W. Mackowski and M. I. Mishchenko. „Calculation of the T matrix and the scattering matrix for ensembles of spheres.“ *J. Opt. Soc. Am. A* 13.11 (1996), 2266–2278. DOI: 10.1364/JOSAA.13.002266.

[58] P. Litvinov and K. Ziegler. „Rigorous derivation of superposition T-matrix approach from solution of inhomogeneous wave equation.“ *J. Quant. Spectrosc. Radiat. Transf.* 109.1 (2008), 74–88. DOI: 10.1016/j.jqsrt.2007.07.001.

[59] F. E. Haniel, H. Schröder, S. Kahaly, et al. „Saturating multiple ionization in intense mid-infrared laser fields.“ *New J. Phys.* 23.5 (2021), 053026. DOI: 10.1088/1367-2630/abf583.

[60] T. H. Distefano and D. E. Eastman. „The band edge of amorphous SiO_2 by photoinjection and photoconductivity measurements.“ *Solid State Commun.* 9.24 (1971), 2259–2261. DOI: 10.1016/0038-1098(71)90643-0.

[61] D. P. Kroese, T. Taimre, and Z. I. Botev. *Handbook of Monte Carlo Methods*. New Jersey: John Wiley & Sons, 2011, 59.

[62] M. E. Muller. „A note on a method for generating points uniformly on n-dimensional spheres.“ *Commun. ACM* 2.4 (1959), 19–20. DOI: 10.1145/377939.377946.

[63] G. Marsaglia. „Choosing a Point from the Surface of a Sphere.“ *Ann. Math. Statist.* 43.2 (1972), 645–646. DOI: 10.1214/aoms/1177692644.

[64] R. E. Caflisch. „Monte Carlo and quasi-Monte Carlo methods.“ *Acta Numer.* 7 (1998), 1–49. DOI: 10.1017/S0962492900002804.

[65] C. Neumann. *Hydrodynamische Untersuchungung: Nebst einem Anhange über die Probleme der Elecktrostatik und der magnetischen Induktion.* Leipzig: Teubner, 1883, 279–282.

[66] I. V. Lindell. „Electrostatic image theory for the dielectric sphere.“ *Radio Sci.* 27.1 (1992), 1–8. DOI: 10.1029/91RS02255.

[67] W. Cai, S. Deng, and D. Jacobs. „Extending the fast multipole method to charges inside or outside a dielectric sphere.“ *J. Comput. Phys.* 223.2 (2007), 846–864. DOI: 10.1016/j.jcp.2006.10.019.

[68] Z. Gan and Z. Xu. „Multiple-image treatment of induced charges in Monte Carlo simulations of electrolytes near a spherical dielectric interface.“ *Phys. Rev. E* 84 (1 2011), 016705. DOI: 10.1103/PhysRevE.84.016705.

[69] „Physical Constants.“ *Pulse-Width Modulated DC–DC Power Converters.* Ed. by M. K. Kazimierczuk. John Wiley & Sons, Ltd, 2013, 915–916. DOI: 10.1002/9781119009597.app3.

[70] P. Virtanen, R. Gommers, T. E. Oliphant, et al. „SciPy 1.0: Fundamental Algorithms for Scientific Computing in Python.“ *Nat. Methods* 17 (2020), 261–272. DOI: 10.1038/s41592-019-0686-2.

[71] P. Rupp. „Ultrafast dynamics on nanostructures in strong fields.“ PhD thesis. Ludwig-Maximilians-Universität München, 2019.

[72] W. Stöber, A. Fink, and E. Bohn. „Controlled growth of monodisperse silica spheres in the micron size range.“ *J. Colloid Interface Sci.* 26.1 (1968), 62–69. DOI: 10.1016/0021-9797(68)90272-5.

[73] Vikash and V. Kumar. „Ultrasonic-assisted de-agglomeration and power draw characterization of silica nanoparticles.“ *Ultrason. Sonochem.* 65 (2020), 105061. DOI: 10.1016/j.ultsonch.2020.105061.

[74] S. Pradhan, J. Hedberg, E. Blomberg, S. Wold, and I. O. Wallinder. „Effect of sonication on particle dispersion, administered dose and metal release of non-functionalized, non-inert metal nanoparticles.“ *J. Nanopart. Res.* 18.9 (2016). DOI: 10.1007/s11051-016-3597-5.

[75] J. Stetefeld, S. A. McKenna, and T. R. Patel. „Dynamic light scattering: a practical guide and applications in biomedical sciences.“ *Biophys. Rev.* 8.4 (2016), 409–427. DOI: 10.1007/s12551-016-0218-6.

[76] G. Bradski. „The OpenCV Library.“ *DDJ* 120 (2000), 122–125.

[77] B. Y. H. LIU and K. W. LEE. „An aerosol generator of high stability.“ *Am. Ind. Hyg.* 36.12 (1975), 861–865. DOI: 10.1080/0002889758507357.

[78] H. Bresch. „Photoionisation von freien Aerosolpartikeln mit Synchrotronstrahlung.“ PhD thesis. Freie Universität Berlin, 2007, pp. 74–76.

[79] M. Kübel, C. Burger, N. G. Kling, et al. „Complete characterization of single-cycle double ionization of argon from the nonsequential to the sequential ionization regime.“ *Phys. Rev. A* 93 (5 2016), 053422. DOI: 10.1103/PhysRevA.93.053422.

[80] N. C. Geib, M. Zilk, T. Pertsch, and F. Eilenberger. „Common pulse retrieval algorithm: a fast and universal method to retrieve ultrashort pulses.“ *Optica* 6.4 (2019), 495–505. DOI: 10.1364/OPTICA.6.000495.

[81] M. Neuhaus, H. Fuest, M. Seeger, et al. „10 W CEP-stable few-cycle source at 2 μm with 100 kHz repetition rate.“ *Opt. Express* 26.13 (2018), 16074–16085. DOI: 10.1364/OE.26.016074.

[82] R. Trebino, K. W. DeLong, D. N. Fittinghoff, et al. „Measuring ultrashort laser pulses in the time-frequency domain using frequency-resolved optical gating.“ *Rev. Sci. Instrum.* 68.9 (1997), 3277–3295. DOI: 10.1063/1.1148286.

[83] R. Trebino. *Frequency-resolved Optical Gating: The Measurement of Ultrashort Laser Pulses*. New York: Springer Science & Business Media, 2000.

[84] N. C. Geib. *Python for pulse retrieval*. https://github.com/ncgeib/pypret. 2019.

[85] J Ullrich, R Moshammer, A Dorn, R Dörner, L. P. H. Schmidt, and H Schmidt-Böcking. „Recoil-ion and electron momentum spectroscopy: reaction-microscopes.“ *Rep. Prog. Phys.* 66.9 (2003), 1463–1545. DOI: 10.1088/0034-4885/66/9/203.

[86] H. Bresch. „Photoionisation von freien Aerosolpartikeln mit Synchrotronstrahlung.“ PhD thesis. Freie Universität Berlin, 2007, p. 71.

[87] H. Bresch. „Photoionisation von freien Aerosolpartikeln mit Synchrotronstrahlung.“ PhD thesis. Freie Universität Berlin, 2007, pp. 55–58.

[88] J. Powell. „Strong-field driven dynamics of metal and dielectric nanoparticles.“ PhD thesis. Kansas State University, 2017, p. 32.

[89] V. C. Felicíssimo, F. F. Guimarães, and F. Gel'mukhanov. „Enhancement of the recoil effect in x-ray photoelectron spectra of molecules driven by a strong ir field.“ *Phys. Rev. A* 72 (2 2005), 023414. DOI: 10.1103/PhysRevA.72.023414.

[90] M. Kircher, J. Rist, F. Trinter, et al. „Photon-Momentum-Induced Molecular Dynamics in Photoionization of N_2 at $h\nu = 40$ keV.“ *Phys. Rev. Lett.* 123 (19 2019), 193001. DOI: 10.1103/PhysRevLett.123.193001.

[91] S. Björklund and V. Kocherbitov. „Alcohols react with MCM-41 at room temperature and chemically modify mesoporous silica.“ *Sci. Rep.* 7.1 (2017), 9960. DOI: 10.1038/s41598-017-10090-x.

[92] Roentdek Handels GmbH. *MCP Delay Line Detector Manual*. Version 11.0.2208.1, http://roentdek.com/manuals/MCP%20Delay%20Line%20manual.pdf, Accessed: 14.12.2022.

[93] Z. Nie, A. Petukhova, and E. Kumacheva. „Properties and emerging applications of self-assembled structures made from inorganic nanoparticles." *Nat. Nanotechnol.* 5.1 (2010), 15–25. DOI: 10.1038/nnano.2009.453.

[94] J. K. Stolarczyk, A. Deak, and D. F. Brougham. „Nanoparticle Clusters: Assembly and Control Over Internal Order, Current Capabilities, and Future Potential." *Adv. Mater.* 28.27 (2016), 5400–5424. DOI: 10.1002/adma.201505350.

[95] N. Pazos-Perez, C. S. Wagner, J. M. Romo-Herrera, et al. „Organized Plasmonic Clusters with High Coordination Number and Extraordinary Enhancement in Surface-Enhanced Raman Scattering (SERS)." *Angew. Chem. Int. Ed.* 51.51 (2012), 12688–12693. DOI: 10.1002/anie.201207019.

[96] O. Chen, L. Riedemann, F. Etoc, et al. „Magneto-fluorescent core-shell supernanoparticles." *Nat. Commun.* 5.1 (2014), 5093. DOI: 10.1038/ncomms6093.

[97] Z.-X. Li, L.-L. Li, Q. Yuan, et al. „Sustainable and Facile Route to Nearly Monodisperse Spherical Aggregates of CeO_2 Nanocrystals with Ionic Liquids and Their Catalytic Activities for CO Oxidation." *J. Phys. Chem. C* 112.47 (2008), 18405–18411. DOI: 10.1021/jp807348n.

[98] I. V. Chernyshova, S. Ponnurangam, and P. Somasundaran. „Tailoring (Bio)chemical Activity of Semiconducting Nanoparticles: Critical Role of Deposition and Aggregation." *J. Am. Chem. Soc.* 133.24 (2011), 9536–9544. DOI: 10.1021/ja202266g.

[99] Q. Zhang, J.-B. Joo, Z. Lu, et al. „Self-assembly and photocatalysis of mesoporous TiO_2 nanocrystal clusters." *Nano Res.* 4.1 (2011), 103–114. DOI: 10.1007/s12274-010-0058-9.

[100] Z. Bian, T. Tachikawa, and T. Majima. „Superstructure of TiO_2 Crystalline Nanoparticles Yields Effective Conduction Pathways for Photogenerated Charges." *J. Phys. Chem. Lett.* 3.11 (2012), 1422–1427. DOI: 10.1021/jz3005128.

[101] L. He, Y. Xiong, M. Zhao, et al. „Bioinspired Synthesis of ZnS Supraparticles toward Photoinduced Dechlorination of 2,2',4,4',5,5'-Hexachlorobiphenyl." *Chem. Asian J.* 8.8 (2013), 1765–1767. DOI: 10.1002/asia.201300277.

[102] F. Fan, Y. Feng, P. Tang, and D. Li. „Facile synthesis and photocatalytic performance of ZnO nanoparticles self-assembled spherical aggregates." *Mater. Lett.* 158 (2015), 290–294. DOI: 10.1016/j.matlet.2015.05.109.

[103] W. Yang, X. Liu, D. Li, L. Fan, and Y. Li. „Aggregation-induced preparation of ultrastable zinc sulfide colloidal nanospheres and their photocatalytic degradation of multiple organic dyes." *Phys. Chem. Chem. Phys.* 17 (22 2015), 14532–14541. DOI: 10.1039/C5CP01831E.

[104] Z. Lu, J. Duan, L. He, Y. Hu, and Y. Yin. „Mesoporous TiO_2 nanocrystal clusters for selective enrichment of phosphopeptides.“ *Anal. Chem.* 82.17 (2010), 7249—7258. DOI: 10.1021/ac1011206.

[105] J. Wei, Y. Ren, W. Luo, et al. „Ordered Mesoporous Alumina with Ultra-Large Pores as an Efficient Absorbent for Selective Bioenrichment.“ *Chem. Mater.* 29.5 (2017), 2211–2217. DOI: 10.1021/acs.chemmater.6b05032.

[106] Q. L. Vuong, P. Gillis, and Y. Gossuin. „Monte Carlo simulation and theory of proton NMR transverse relaxation induced by aggregation of magnetic particles used as MRI contrast agents.“ *J. Magn. Reson.* 212.1 (2011), 139–148. DOI: 10.1016/j.jmr.2011.06.024.

[107] E. Pöselt, H. Kloust, U. Tromsdorf, et al. „Relaxivity Optimization of a PEGylated Iron-Oxide-Based Negative Magnetic Resonance Contrast Agent for T_2-Weighted Spin–Echo Imaging.“ *ACS Nano* 6.2 (2012), 1619–1624. DOI: 10.1021/nn204591r.

[108] R. J. Hickey, X. Meng, P. Zhang, and S.-J. Park. „Low-Dimensional Nanoparticle Clustering in Polymer Micelles and Their Transverse Relaxivity Rates.“ *ACS Nano* 7.7 (2013), 5824–5833. DOI: 10.1021/nn400824b.

[109] S. Bhattacharjee. „DLS and zeta potential – What they are and what they are not?“ *J. Control. Release* 235 (2016), 337–351. DOI: 10.1016/j.jconrel.2016.06.017.

[110] S. Samimi, N. Maghsoudnia, R. B. Eftekhari, and F. Dorkoosh. „Chapter 3 - Lipid-Based Nanoparticles for Drug Delivery Systems.“ *Characterization and Biology of Nanomaterials for Drug Delivery*. Ed. by S. S. Mohapatra, S. Ranjan, N. Dasgupta, R. K. Mishra, and S. Thomas. Micro and Nano Technologies. Elsevier, 2019, 47–76. DOI: 10.1016/B978-0-12-814031-4.00003-9.

[111] L. Zhuravlev. „The surface chemistry of amorphous silica. Zhuravlev model.“ *Colloids Surf. A: Physicochem. Eng. Asp.* 173.1 (2000), 1–38. DOI: 10.1016/S0927-7757(00)00556-2.

[112] Y. Duval, J. A. Mielczarski, O. S. Pokrovsky, E. Mielczarski, and J. J. Ehrhardt. „Evidence of the Existence of Three Types of Species at the Quartz-Aqueous Solution Interface at pH 0-10: XPS Surface Group Quantification and Surface Complexation Modeling.“ *J. Phys. Chem. B* 106.11 (2002), 2937–2945. DOI: 10.1021/jp012818s.

[113] M. A. Brown, T. Huthwelker, A. Beloqui Redondo, et al. „Changes in the Silanol Protonation State Measured In Situ at the Silica–Aqueous Interface.“ *J. Phys. Chem. Lett.* 3.2 (2012), 231–235. DOI: 10.1021/jz201533w.

[114] L. S. de Lara, V. A. Rigo, M. F. Michelon, C. O. Metin, Q. P. Nguyen, and C. R. Miranda. „Molecular dynamics studies of aqueous silica nanoparticle dispersions: salt effects on the double layer formation.“ *J. Phys. Condens. Matter* 27.32 (2015), 325101. DOI: 10.1088/0953-8984/27/32/325101.

[115] C. O. Metin, L. W. Lake, C. R. Miranda, and Q. P. Nguyen. „Stability of aqueous silica nanoparticle dispersions.“ *J. Nanopart. Res.* 13.2 (2011), 839–850. DOI: 10.1007/s11051-010-0085-1.

[116] C. F. Bohren and D. R. Huffman. „Absorption and Scattering of Light by Small Particles.“ John Wiley & Sons, Ltd, 1998. Chap. 4, 82–129. DOI: 10.1002/9783527618156.ch4.

[117] D. J. Lockwood. „Rayleigh and Mie Scattering.“ *Encyclopedia of Color Science and Technology*. Ed. by M. R. Luo. New York, NY: Springer New York, 2016, 1097–1107. DOI: 10.1007/978-1-4419-8071-7_218.

[118] M. Schulz, R. Moshammer, D. Fischer, et al. „Three-dimensional imaging of atomic four-body processes.“ *Nature* 422.6927 (2003), 48–50. DOI: 10.1038/nature01415.

[119] N. Ekanayake, T. Severt, M. Nairat, et al. „H_2 roaming chemistry and the formation of H_3^+ from organic molecules in strong laser fields.“ *Nat. Commun.* 9.1 (2018), 5186. DOI: 10.1038/s41467-018-07577-0.

[120] P. Rupp, L. Seiffert, Q. Liu, et al. „Quenching of material dependence in few-cycle driven electron acceleration from nanoparticles under many-particle charge interaction.“ *J. Mod. Opt.* 64.10-11 (2017), 995–1003. DOI: 10.1080/09500340.2016.1267272.

[121] P. B. Corkum. „Plasma perspective on strong field multiphoton ionization.“ *Phys. Rev. Lett.* 71 (13 1993), 1994–1997. DOI: 10.1103/PhysRevLett.71.1994.

[122] J. A. Powell, A. M. Summers, Q. Liu, et al. „Interplay of pulse duration, peak intensity, and particle size in laser-driven electron emission from silica nanospheres.“ *Opt. Express* 27.19 (2019), 27124–27135. DOI: 10.1364/OE.27.027124.

[123] U. Ablikim, C. Bomme, T. Osipov, et al. „A coincidence velocity map imaging spectrometer for ions and high-energy electrons to study inner-shell photoionization of gas-phase molecules.“ *Rev. Sci. Instrum.* 90.5 (2019), 055103. DOI: 10.1063/1.5093420.

[124] F. Süßmann and M. F. Kling. „Attosecond nanoplasmonic streaking of localized fields near metal nanospheres.“ *Phys. Rev. B* 84.12 (2011). DOI: 10.1103/physrevb.84.121406.

[125] J. A. Powell, J. Li, A. Summers, et al. „Strong-Field Control of Plasmonic Properties in Core–Shell Nanoparticles.“ *ACS Photonics* 9.11 (2022), 3515–3521. DOI: 10.1021/acsphotonics.2c00663.

[126] F. Sun, H. Li, S. Song, et al. „Single-shot imaging of surface molecular ionization in nanosystems.“ *Nanophotonics* 10.10 (2021), 2651–2660. DOI: 10.1515/nanoph-2021-0172.

[127] M. S. Alghabra, R. Ali, V. Kim, et al. „Anomalous formation of trihydrogen cations from water on nanoparticles.“ *Nat. Commun.* 12.1 (2021), 3839. DOI: 10.1038/s41467-021-24175-9.

[128] R. T. Wiedmann, R. G. Tonkyn, M. G. White, K. Wang, and V. McKoy. „Rotationally resolved threshold photoelectron spectra of OH and OD.“ *J. Chem. Phys.* 97.2 (1992), 768–772. DOI: 10.1063/1.463179.

[129] J. P. Snyder. *Map projections: A working manual.* 1987. DOI: 10.3133/pp1395.

[130] R. G. Greenler. „Infrared Study of the Adsorption of Methanol and Ethanol on Aluminum Oxide.“ *J. Chem. Phys.* 37.9 (1962), 2094–2100. DOI: 10.1063/1.1733430.

[131] B. Vincent, Z. Király, S. Emmett, and A. Beaver. „The stability of silica dispersions in ethanol/cyclohexane mixtures.“ *Colloids Surf.* 49 (1990), 121–132. DOI: 10.1016/0166-6622(90)80097-N.

[132] D. Roy, S. Liu, B. L. Woods, et al. „Nonpolar Adsorption at the Silica/Methanol Interface: Surface Mediated Polarity and Solvent Density across a Strongly Associating Solid/Liquid Boundary.“ *J. Phys. Chem. C* 117.51 (2013), 27052–27061. DOI: 10.1021/jp410756g.

[133] A. W. Coats and J. P. Redfern. „Thermogravimetric analysis. A review.“ *Analyst* 88 (1053 1963), 906–924. DOI: 10.1039/AN9638800906.

[134] J. J. Karnes, E. A. Gobrogge, R. A. Walker, and I. Benjamin. „Unusual Structure and Dynamics at Silica/Methanol and Silica/Ethanol Interfaces—A Molecular Dynamics and Nonlinear Optical Study.“ *J. Phys. Chem. B* 120.8 (2016), 1569–1578. DOI: 10.1021/acs.jpcb.5b07777.

[135] K. Ren, Y.-P. Wang, and S. Liu. „The role of solute polarity on methanol–silica interfacial solvation: a molecular dynamics study.“ *Phys. Chem. Chem. Phys.* 23 (2 2021), 1092–1102. DOI: 10.1039/D0CP04422A.

[136] L. J. Frasinski. „Covariance mapping techniques.“ *J. Phys. B* 49.15 (2016), 152004. DOI: 10.1088/0953-4075/49/15/152004.

[137] M. F. Kling, C. Siedschlag, A. J. Verhoef, et al. „Control of Electron Localization in Molecular Dissociation.“ *Science* 312.5771 (2006), 246–248. DOI: 10.1126/science.1126259.

[138] H Li, X Gong, K Lin, et al. „Sub-cycle directional control of the dissociative ionization of H_2 in tailored femtosecond laser fields.“ *J. Phys. B* 50.17 (2017), 172001. DOI: 10.1088/1361-6455/aa8243.

[139] H. Kang, J. T. Buchman, R. S. Rodriguez, et al. „Stabilization of Silver and Gold Nanoparticles: Preservation and Improvement of Plasmonic Functionalities.“ *Chem. Rev.* 119.1 (2018), 664–699. DOI: 10.1021/acs.chemrev.8b00341.

[140] J. K. Lee, S. Banerjee, H. G. Nam, and R. N. Zare. „Acceleration of reaction in charged microdroplets.“ *Q. Rev. Biophys.* 48.4 (2015), 437–444. DOI: 10.1017/S0033583515000086.

[141] E. C. Griffith and V. Vaida. „In situ observation of peptide bond formation at the water-air interface.“ *PNAS* 109.39 (2012), 15697–15701. DOI: 10.1073/pnas.1210029109.

[142] A. G. Gale, T. T. Odbadrakh, B. T. Ball, and G. C. Shields. „Water-Mediated Peptide Bond Formation in the Gas Phase: A Model Prebiotic Reaction.“ *J. Phys. Chem. A* 124.20 (2020), 4150–4159. DOI: 10.1021/acs.jpca.0c02906.

[143] A. K. Badu-Tawiah, D. I. Campbell, and R. G. Cooks. „Accelerated C–N Bond Formation in Dropcast Thin Films on Ambient Surfaces.“ *JASMS* 23.9 (2012), 1461–1468. DOI: 10.1007/s13361-012-0394-y.

[144] R. M. Bain, C. J. Pulliam, and R. G. Cooks. „Accelerated Hantzsch electrospray synthesis with temporal control of reaction intermediates.“ *Chem. Sci.* 6 (1 2015), 397–401. DOI: 10.1039/C4SC02436B.

[145] M. Girod, E. Moyano, D. I. Campbell, and R. G. Cooks. „Accelerated bimolecular reactions in microdroplets studied by desorption electrospray ionization mass spectrometry.“ *Chem. Sci.* 2 (3 2011), 501–510. DOI: 10.1039/C0SC00416B.

[146] B. M. Marsh, K. Iyer, and R. G. Cooks. „Reaction Acceleration in Electrospray Droplets: Size, Distance, and Surfactant Effects.“ *JASMS* 30.10 (2019), 2022–2030. DOI: 10.1007/s13361-019-02264-w.

[147] Y. Li, X. Yan, and R. G. Cooks. „The Role of the Interface in Thin Film and Droplet Accelerated Reactions Studied by Competitive Substituent Effects.“ *Angew. Chem. Int. Ed.* 55.10 (2016), 3433–3437. DOI: 10.1002/anie.201511352.

[148] H. Xiong, J. K. Lee, R. N. Zare, and W. Min. „Strong Electric Field Observed at the Interface of Aqueous Microdroplets.“ *J. Phys. Chem. Lett.* 11.17 (2020), 7423–7428. DOI: 10.1021/acs.jpclett.0c02061.

[149] V. Kwan and S. Consta. „Bridging electrostatic properties between nanoscopic and microscopic highly charged droplets.“ *Chem. Phys. Lett.* 746 (2020), 137238. DOI: 10.1016/j.cplett.2020.137238.

[150] H. Hao, I. Leven, and T. Head-Gordon. „Can electric fields drive chemistry for an aqueous microdroplet?“ *Nat. Commun.* 13.1 (2022), 280. DOI: 10.1038/s41467-021-27941-x.

[151] H. Xiong, J. K. Lee, R. N. Zare, and W. Min. „Strong Concentration Enhancement of Molecules at the Interface of Aqueous Microdroplets.“ *J. Phys. Chem. B* 124.44 (2020), 9938–9944. DOI: 10.1021/acs.jpcb.0c07718.

[152] Y. Jung and R. A. Marcus. „On the Theory of Organic Catalysis “on Water”.“ *J. Am. Chem. Soc.* 129.17 (2007), 5492–5502. DOI: 10.1021/ja068120f.

[153] T. Sahraeian, D. S. Kulyk, and A. K. Badu-Tawiah. „Droplet Imbibition Enables Nonequilibrium Interfacial Reactions in Charged Microdroplets.“ *Langmuir* 35.45 (2019), 14451–14457. DOI: 10.1021/acs.langmuir.9b02439.

[154] K.-H. Huang, Z. Wei, and R. G. Cooks. „Accelerated reactions of amines with carbon dioxide driven by superacid at the microdroplet interface.“ *Chem. Sci.* 12 (6 2021), 2242–2250. DOI: 10.1039/D0SC05625A.

[155] C. C. Harper, D. D. Brauer, M. B. Francis, and E. R. Williams. „Direct observation of ion emission from charged aqueous nanodrops: effects on gaseous macromolecular charging.“ *Chem. Sci.* 12 (14 2021), 5185–5195. DOI: 10.1039/D0SC05707J.

[156] L. Konermann, E. Ahadi, A. D. Rodriguez, and S. Vahidi. „Unraveling the Mechanism of Electrospray Ionization.“ *Anal. Chem.* 85.1 (2013), 2–9. DOI: 10.1021/ac302789c.

[157] C. Lübbert and W. Peukert. „Characterization of Electrospray Drop Size Distributions by Mobility-Classified Mass Spectrometry: Implications for Ion Clustering in Solution and Ion Formation Pathways.“ *Anal. Chem.* 93.38 (2021), 12862–12871. DOI: 10.1021/acs.analchem.1c00727.

[158] Lord Rayleigh F.R.S. „XX. On the equilibrium of liquid conducting masses charged with electricity.“ *Lond. Edinb. Dublin philos. mag.* 14.87 (1882), 184–186. DOI: 10.1080/14786448208628425.

[159] G. Kresse and J. Hafner. „Ab initio molecular dynamics for liquid metals.“ *Phys. Rev. B* 47 (1 1993), 558–561. DOI: 10.1103/PhysRevB.47.558.

[160] J. Hafner. „Ab-initio simulations of materials using VASP: Density-functional theory and beyond.“ *J. Comput. Chem.* 29.13 (2008), 2044–2078. DOI: 10.1002/jcc.21057.

[161] F. Jensen. *Introduction to Computational Chemistry, 3rd Edition*. John Wiley & Sons, 2017.

[162] J. P. Perdew, K. Burke, and M. Ernzerhof. „Generalized Gradient Approximation Made Simple.“ *Phys. Rev. Lett.* 77 (18 1996), 3865–3868. DOI: 10.1103/PhysRevLett.77.3865.

[163] P. E. Blöchl. „Projector augmented-wave method.“ *Phys. Rev. B* 50 (24 1994), 17953–17979. DOI: 10.1103/PhysRevB.50.17953.

[164] T. P. Otanicar, P. E. Phelan, and J. S. Golden. „Optical properties of liquids for direct absorption solar thermal energy systems.“ *Solar Energy* 83.7 (2009), 969–977. DOI: 10.1016/j.solener.2008.12.009.

[165] F. A. Jenkins and H. E. White. „Fundamentals of Optics.“ Ed. by S. Grall. Fourth. McGraw-Hill Higher Education, 2001, 479.

[166] E. Sani and A. Dell'Oro. „Optical constants of ethylene glycol over an extremely wide spectral range.“ *Opt. Mater.* 37 (2014), 36–41. DOI: 10.1016/j.optmat.2014.04.035.

[167] I. H. Malitson. „Interspecimen Comparison of the Refractive Index of Fused Silica.“ *J. Opt. Soc. Am.* 55.10 (1965), 1205–1209. DOI: 10.1364/JOSA.55.001205.

[168] J. V. Iribarne and B. A. Thomson. „On the evaporation of small ions from charged droplets.“ *J. Chem. Phys.* 64.6 (1976), 2287–2294. DOI: 10.1063/1.432536.

[169] R. Osserman. „The isoperimetric inequality.“ *Bull. Am. Math.* 84.6 (1978), 1182–1238. DOI: 10.1090/s0002-9904-1978-14553-4.

[170] E. A. Parmentier, G. David, P. C. Arroyo, S. Bibawi, K. Esat, and R. Signorell. „Photochemistry of single optically trapped oleic acid droplets.“ *J. Aerosol Sci.* 151 (2021), 105660. DOI: 10.1016/j.jaerosci.2020.105660.

[171] M. Kerker, P. Scheiner, and D. D. Cooke. „The range of validity of the Rayleigh and Thomson limits for Lorenz-Mie scattering.“ *J. Opt. Soc. Am.* 68.1 (1978), 135–137. DOI: 10.1364/JOSA.68.000135.

[172] L. Konermann. „A Simple Model for the Disintegration of Highly Charged Solvent Droplets during Electrospray Ionization.“ *JASMS* 20.3 (2009), 496–506. DOI: 10.1016/j.jasms.2008.11.007.

[173] U. Näher, S. Bjørnholm, S. Frauendorf, F. Garcias, and C. Guet. „Fission of metal clusters.“ *Phys. Rep.* 285.6 (1997), 245–320. DOI: 10.1016/S0370-1573(96)00040-3.

[174] D. Duft, T. Achtzehn, R. Müller, B. A. Huber, and T. Leisner. „Rayleigh jets from levitated microdroplets.“ *Nature* 421.6919 (2003), 128–128. DOI: 10.1038/421128a.

[175] L. C. Allen. „Electronegativity is the average one-electron energy of the valence-shell electrons in ground-state free atoms.“ *J. Am. Chem. Soc.* 111.25 (1989), 9003–9014. DOI: 10.1021/ja00207a003.

[176] S. Banerjee and S. Mazumdar. „Electrospray ionization mass spectrometry: a technique to access the information beyond the molecular weight of the analyte.“ *Int. J. Anal. Chem.* 2012 (2012), 282574–282574. DOI: 10.1155/2012/282574.

[177] Z. Wei, Y. Li, R. G. Cooks, and X. Yan. „Accelerated Reaction Kinetics in Microdroplets: Overview and Recent Developments.“ *Annu. Rev. Phys. Chem.* 71.1 (2020), 31–51. DOI: 10.1146/annurev-physchem-121319-110654.

Acknowledgments

I would like to thank Prof. Dr. Matthias Kling for giving me the opportunity of doing a PhD in his group and for his supervision and guidance throughout the years. I am thankful for his trust in my work and for involving me in numerous international collaborations, which allowed me to work on a wide range of exciting topics. It enabled me to meet scientists from all over the globe, and make many new friends. In particular, I had the great pleasure of working with and learning from Dr. James Cryan, Prof. Dr. Ali Alnaser, Prof. Dr. Rami Ali, Prof. Dr. Nora Berrah, PD Dr. Robert Moshammer, and Prof. Dr. Cesar Costa Vera.

I am very grateful to Dr. Boris Bergues for his supervision of my PhD projects and for leading the whole reaction nanoscopy team. He taught me a great deal about how to approach scientific questions and how to use simple models to gain an intuitive understanding of complex physical processes. I admire his science ethics and found our many discussions immensely inspiring.

I thank Christian Burger and Philipp Rupp for their introduction to the experimental techniques of ion momentum spectroscopy and reaction nanoscopy. I very much enjoyed their companionship in the office and appreciated their help.

I am grateful to the newer members of the reaction nanoscopy team, Ritika Dagar and Wenbin Zhang, for their help in the lab and with the laser operation in particular. At this point, I want to give special thanks to Marcel Neuhaus, who we could always rely on when the laser required extra special care. I very much appreciate our nano-collaboration with Prof. Dr. Stefan Maier and Prof. Dr. Emiliano Cortés. I am especially grateful to Dr. Ana Sousa-Castillo for producing all the nanoparticles we needed at an impressively fast speed.

I would also like to thank the other members of the Kling group for their continuous input and motivation, the lively discussions, and the fun we had in the lab, the office, the Mensa, on the volleyball field, and elsewhere. Thank you, Džiugas Kimbaras, Max Seeger, Johannes Blöchl, Johannes Schötz, Najd Altwaijry, Shubhadeep Biswas, Sambit Mitra, Weiwei Li, Thomas Nubbemayer, Mario Aulich, Zilong Wang and Martin Graßl!

I very much appreciated the amazing social life within our group. I had a lot of fun on our skiing trips, our visits to Mühlenpark and Oktoberfest, and I will not forget our adventurous Christmas parties (laser tag battles, go-kart racing, escape room challenges, and so on). It was great!

From our group members on the side of the great pond, I would like to thank Dr.

Adam Summers, Dr. Alexandra Feinberg, Dr. Ilana Porter, and Martin Graßl for their hospitality, their help with paper writing, and with the completion of this thesis.

I am grateful to Florian Saran, Romy Knab, Klaus Franke, and Dr. Nils Haag for helping me overcome all technical and administrative hurdles during purchasing, shipping, or moving of equipment.

I also want to thank all of my friends and family outside of academia. They helped me maintain a good balance between research work and normal life and offered the perfect distraction from work-related issues whenever necessary. Special thanks go to my parents for their ongoing trust, support, and guidance during my studies and beyond.

Lastly, I would like to thank Jessica Zauner for enduring me in the stressful phases of the PhD work during the last five years, for having an open ear for all my complaints, and for continuously motivating me.